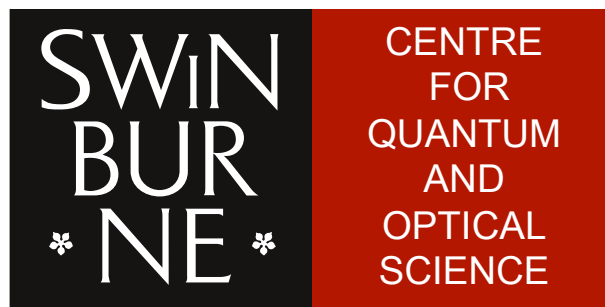


Sub-Micron-Period Magnetic Lattices for Ultracold Atoms



Centre for Quantum and Optical Science
Faculty of Science, Engineering and Technology
Swinburne University of Technology
Melbourne, Australia

June 2017

Abstract

Magnetic lattices comprising periodic arrays of magnetic microtraps are a promising complementary tool to the widely used optical lattices for trapping periodic arrays of ultracold atoms. Magnetic lattices based on patterned magnetic films allow nearly arbitrary lattice geometries and lattice periods without limitations imposed by optical wavelengths. In this thesis, a hybrid atom chip structure containing a patterned magnetic lattice film is designed and fabricated. The successful trapping of ultracold ^{87}Rb atoms in a $0.7\ \mu\text{m}$ -period triangular magnetic lattice is reported.

Four magnetic lattice structures including $0.7\ \mu\text{m}$ -period 2D square and triangular lattices and 1D $0.7\ \mu\text{m}$ -period and $5\ \mu\text{m}$ -period lattices are patterned by electron beam lithography and reactive ion etching in a magnetic Co/Pd multi-atomic layer film. The submicron period magnetic lattices are chosen with the potential to enable quantum tunnelling experiments and to simulate condensed matter phenomena. For initial preparation of the ultracold ^{87}Rb atoms and loading the magnetic lattice, a chip structure comprising Z-shaped and U-shaped current-carrying wires is produced from direct bonded copper (DBC).

Before loading the magnetic lattice traps, the effects of atom-surface interaction are studied by bringing atoms trapped in the Z-wire magnetic trap within a few micrometres of the magnetic film surface. The observed atom loss in the Z-wire trap originates mainly from surface-induced evaporation and the attractive Casimir-Polder interaction, rather than from spin-flips due to Johnson magnetic noise from the reflecting gold surface layer. Then the interaction of the ultracold atoms with the $0.7\ \mu\text{m}$ -period magnetic potential located very close to the chip surface is studied by the reflection dynamics of the atoms. The observed half-moon-shaped clouds of the reflected atoms are consistent with a sinusoidal corrugated magnetic lattice potential. Finally, the results of loading atoms into the $0.7\ \mu\text{m}$ -period triangular magnetic lattice at estimated distances of only 90 - 260 nm from the chip surface are presented. The measured trap lifetimes are 0.4 - 1.7 ms, depending on distance from the chip surface, which are consistent with surface-induced thermal evaporation and

three-body recombination losses as a result of the very tight lattice traps.

The trapping of atoms in a $0.7\ \mu\text{m}$ -period magnetic lattice is an important step towards studying quantum tunnelling in a magnetic lattice. To the best of my knowledge, this represents the first realisation of trapping ultracold atoms in a submicron period magnetic lattice. In addition, the trapping of atoms at estimated distances down to about 100 nm from the chip surface and at trapping frequencies as high as 800 kHz represents new territory for trapping ultracold atoms.

Acknowledgements

It is a great opportunity for me to spend my PhD time in the Centre for Quantum and Optical Science at Swinburne University of Technology. This project couldn't be successfully completed without the continuous help and support from a number of people during the last four years. In the beginning of my thesis, I would like to express my sincere gratitude to all of them.

First of all, I would like to thank my supervisor Prof. Peter Hannaford for his valuable supervision, encouragement and support throughout the project. I appreciate his insight in physics, optimism on experiments and his generosity with conference opportunities.

Secondly, I want to thank my co-supervisor Prof. Russell McLean and Prof. Andrei Sidorov. Their advice at the group meetings and expertise in daily experiment work was helpful and stimulated new ideas. Many thanks to Dr. Alexander Akoulchine for the knowledge of lasers and spectroscopy.

It is important for me to acknowledge the people who were involved in fabricating the sub-micron period magnetic lattices: Prof. Manfred Albrecht at the Universität Augsburg, Germany for kindly providing the state-of-art Co/Pd multi-atomic layer film; Prof. Saulius Juodkazis, Armandas Balcytis and Pierrette Michaux from the Centre for Micro-Photonics at Swinburne for their great job with producing the magnetic lattice structures; and Dr. James Wang for providing facilities including the AFM/MFM and sharing his experience in characterising the patterned magnetic film.

I want to thank other members in our group and in the Centre who provided excellent company, advice and help. I am grateful for the knowledge and skills I learned from Dr. Ivan Herrera, who worked for two years as a postdoc on the project, from aligning the optics to analysing the data. I always benefited from discussions with Dr. Yun Li from the theory side and enjoyed the talks in coffee time. To our former PhD student, Prince Surendran, I always remember in the early days we were struggling together in the lab. Many thanks to Alessandro Brolis for

the stimulating discussions. Now the experiments are in the hands of Tien Tran who joined the lab two years ago. He gave me a lot of assistance in the experiment. It was great experience to work with our visiting scientist Dr. Shannon Whitlock. He certainly contributed a lot to this project.

I would like to thank other people in the Centre, especially Research Support Coordinator Tatiana Tchernova for assistance with all administrative paperwork, travelling tickets, and of course, the wonderful annual Christmas BBQ in the nearby Central Park.

Next, I want to thank my good friends, especially the brothers back in the undergraduate period, Xiaodong Zhou, Pan Zheng and Yandong Liu. I appreciate our long-lasting friendship. It is hard to forget every QQ conversation across continents. I wish us all a bright future.

Last but not least, I want to thank my parents for their love and support. This thesis is for them.

Declaration

The work presented in this thesis entitled “Sub-Micron-Period Magnetic Lattices for Ultracold Atoms” has been carried out in the Centre for Quantum and Optical Science (CQOS) at Swinburne University of Technology in Melbourne between December 2012 and December 2016. The thesis contains no material that has been accepted for the award of any other degree or diploma. To the best of my knowledge, the thesis contains no material previously published or written by another author, except where due reference is made in the text of the thesis.

yibo wang

Yibo Wang

Melbourne, Victoria, Australia

18 June 2017

Contents

Abstract	i
Acknowledgements	iii
Declaration	v
List of Figures	x
List of Tables	xiii
1 Introduction	1
1.1 The quantum world and ultracold quantum gases	1
1.2 The atom chip: cold matter lab on a chip	4
1.3 Hybrid atom chip with a magnetic lattice	7
1.4 Overview of thesis	9
2 Theoretical background	11
2.1 Magnetic trapping of neutral atoms	11
2.2 Magnetic traps on atom chips	13
2.2.1 Principle of wire magnetic traps	13
2.2.2 U-wire and Z-wire configurations	15
2.3 Mirror magneto-optical trap (MMOT)	16
2.4 The thermodynamics of cold atoms	17

2.5	Forced evaporative cooling	18
2.6	Theory of Bose-Einstein Condensation	20
2.6.1	Thomas-Fermi approximation	22
2.6.2	BECs in a lattice potential: quantum tunnelling	24
2.7	Atom-chip surface interactions	26
2.7.1	Johnson noise	26
2.7.2	Casimir-Polder interaction	28
2.8	Sub-micron period magnetic lattices	30
2.9	Summary	32
3	Magnetic lattice atom chip design and fabrication	33
3.1	Co/Pd multilayer mono-atomic magnetic films	34
3.2	Co/Pd film characterisation	35
3.3	Sub-micron-period magnetic lattice structure fabrication	37
3.3.1	Correction for proximity effects	39
3.4	Film characterisation	42
3.5	Hybrid atom chip	45
3.5.1	Direct bonded copper	46
3.5.2	Atom chip design: four U-wire and four Z-wire configuration	47
3.5.3	Assembly and pre-baking of hybrid magnetic lattice chip	49
3.6	Summary	50
4	Experimental setup and BEC preparation	51
4.1	Ultrahigh vacuum system	52
4.2	Laser system	53
4.3	Absorption imaging	58
4.3.1	CCD camera	59
4.3.2	Imaging optical setup	59
4.4	Experimental control and 50 Hz line trigger	61

4.4.1	Control electronics	62
4.4.2	50 Hz AC line synchronisation	63
4.5	Experimental sequence for BEC	64
4.5.1	Mirror MOT	64
4.5.2	Compressed U-wire MMOT	64
4.5.3	Optical pumping	65
4.5.4	Z-wire magnetic trap	67
4.5.5	Bose-Einstein condensate in the Z-wire trap	72
4.5.6	RF spectroscopy	75
4.6	Summary	78
5	Loading atoms into the $0.7\ \mu\text{m}$-period triangular magnetic lattice	79
5.1	Z-wire trapped atoms-surface interactions	80
5.1.1	Z-wire trap distance calibration	80
5.1.2	Trap lifetime versus Z-wire trap distance	82
5.1.3	Atom fraction versus Z-wire trap distance	85
5.2	Loading a sub-micron period magnetic lattice: simulation	89
5.2.1	$0.7\ \mu\text{m}$ -period 2D magnetic lattice	89
5.2.2	$0.7\ \mu\text{m}$ -period 1D magnetic lattice	92
5.3	Projection of ultracold atoms towards the 2D lattice potential	93
5.3.1	Reflection from a $0.7\ \mu\text{m}$ -period triangular magnetic potential	95
5.4	Loading a $0.7\ \mu\text{m}$ -period triangular magnetic lattice: preliminary results	98
5.5	Summary	109
6	Summary and future directions	111
6.1	Summary	111
6.2	Future directions	113
	Bibliography	115

Publications

135

List of Figures

2.1	Two-dimensional quadrupole magnetic field formed by current carrying wire	14
2.2	Waveguide for atoms on an atom chip	15
2.3	Quadrupole U-wire trap	15
2.4	Ioffe-Pritchard Z-wire trap	16
2.5	Configurations of a standard MOT and a mirror MOT	17
2.6	Threshold for runaway evaporation	21
2.7	Schematic of trapped atoms close to a conducting layer	27
2.8	Effects of Casimir-Polder interaction	29
2.9	Optimised square magnetic lattice	31
2.10	Optimised triangular magnetic lattice	32
3.1	Co/Pd multilayer structure and grain size measurement	35
3.2	Co/Pd hysteresis loop and magnetic domain structure	36
3.3	Fabrication process using e-beam lithography plus reactive ion etching	38
3.4	Proximity effect in electron-beam lithography	40
3.5	Electron beam lithography proximity effect correction	40
3.6	SEM image of the fabricated sample with four lattice structures	41
3.7	SEM images of the 1D 0.7 μm -period magnetic lattice structure	42
3.8	SEM images of the 2D 0.7 μm -period magnetic lattice structure	43
3.9	MFM measurement of the 1D 0.7 μm -period lattice structure	44

3.10	MFM measurement of the $0.7\ \mu\text{m}$ -period square lattice structure	45
3.11	Schematic of the hybrid magnetic lattice atom chip	46
3.12	The designed DBC atom chip wire pattern	48
3.13	The fabrication procedure of the DBC chip	49
3.14	Photography of hybrid magnetic lattice atom chip assembly	50
4.1	Schematic drawing of the vacuum system	52
4.2	Energy-level diagram of the ^{87}Rb D_2 line with laser frequencies	54
4.3	Schematic drawing of laser system	55
4.4	Surrounding optics on the machine table.	57
4.5	Absorption imaging optics and effective pixel size measurement	60
4.6	50 Hz AC line synchronisation circuit	63
4.7	Schematic of optical pumping to magnetically trapped states	66
4.8	Z-trap radial frequency measurement	68
4.9	Z-trap axial frequency measurement	70
4.10	Evolution of collective mode excitation	70
4.11	Z-wire trap lifetime measurement	71
4.12	Atom number, temperature and phase space density versus RF frequency	72
4.13	Bimodal density profile in Z-wire trap	73
4.14	Anisotropic expansion of a BEC	74
4.15	RF spectrum of a BEC in Z-wire magnetic trap	75
4.16	RF induced coupling between magnetic sublevels of $F = 1$ state	76
4.17	RF coupling strength measurement of magnetic states in a BEC	77
5.1	Distance calibration of a Z-wire trap near the chip surface	81
5.2	Z-wire trap lifetime measurements near the chip surface	82
5.3	Z-wire trap lifetime versus trap-surface distance	84

5.4	Z-wire trap radial frequency and trap depth versus trap-surface distances	85
5.5	Remaining atom fraction in Z-wire trap versus trap-surface distance	87
5.6	Two theoretical models of the remaining atom fraction	88
5.7	Optimised square and triangular magnetic lattice potential	90
5.8	Loading procedure for 1D $0.7 \mu\text{m}$ -period magnetic lattice	92
5.9	Trap potential of the created 1D $0.7 \mu\text{m}$ -period magnetic lattice	93
5.10	Square and triangular magnetic potential pattern without bias fields	94
5.11	Reflected ultracold clouds from the $0.7 \mu\text{m}$ -period triangular magnetic potential	96
5.12	Reflection dynamics of the ultracold cloud from the $0.7 \mu\text{m}$ -period triangular magnetic potential	97
5.13	Triangular magnetic lattice	99
5.14	Triangular magnetic lattice trap potential in z -direction for various B_x bias field	100
5.15	Absorption images of atoms trapped in the $0.7 \mu\text{m}$ -period triangular magnetic lattice	102
5.16	Lifetime measurements of atoms trapped in the $0.7 \mu\text{m}$ -period triangular magnetic lattice	103
5.17	The measured lattice lifetimes are fitted with the model of surface-induced thermal evaporation	105
5.18	Triangular magnetic lattice trap potential in z -direction for various B_x bias field with an offset $\delta d = 25 \text{ nm}$	106
5.19	Calculated 3-body recombination lifetime τ_{3b}	108

List of Tables

2.1	Calculated parameters for a 2D square lattice at the superfluid-Mott insulator transition point	25
5.1	Calculated parameters for the optimised 2D magnetic lattices	91
5.2	Calculated parameters for ^{87}Rb $ F = 1, m_F = -1\rangle$ atoms trapped in the $0.7\ \mu\text{m}$ -period triangular magnetic lattice including Casimir-Polder interaction	101
5.3	Calculated parameters for ^{87}Rb $ F = 1, m_F = -1\rangle$ atoms trapped in the $0.7\ \mu\text{m}$ -period triangular magnetic lattice with offset parameter $\delta d = 25\ \text{nm}$	106
5.4	Measured and calculated lifetimes of magnetic lattice trap	108

CHAPTER 1

Introduction

1.1 The quantum world and ultracold quantum gases

Matter exists in different states according to our daily life experience. Normally, from high temperature to low temperature, the states of matter can be categorised into plasma, gas, liquid and solid. Our intuition based on this macroscopic world helps us to understand phenomena that occur in the classical world more easily. However, once we acquired the capability to cool matter to extremely low temperatures, sometimes it can enter a new phase under certain conditions: a quantum condensed phase, such as traditional superconductivity, superfluidity and high- T_c superconductivity. In this peculiar quantum world, our established intuition in the classical world often creates a barrier in understanding the behaviour of a system governed by quantum mechanics. Although we are far from clearly understanding all of these phenomena, this fascinating quantum world has attracted a lot of attention from scientists since the beginning of the twentieth century. From an applications point of view, scientists believe that understanding the underlying mechanisms of these quantum phenomena may guide us towards building, for example, a power network with room temperature superconductors one day in the future. This would

change the landscape of the world energy consumption and benefit the whole human society.

Back in 1925, inspired by Bose's initial work on photons, Einstein extended this newly developed statistical description to non-zero mass indistinguishable particles. The Bose-Einstein statistics describes the statistical distribution of non-interacting bosons [1–3]. When bosons are cooled to temperatures below a critical temperature it is predicted that all the particles can occupy in the lowest energy states, producing a macroscopic population in the same state now known as a Bose-Einstein condensate (BEC). Since then, physicists have gradually realised that the transition to the quantum condensed phase should be a key concept in understanding these fascinating phenomena. The Bardeen-Cooper-Schrieffer (BCS) theory [4–6] is an outstandingly successful example to explain low- T_c superconductivity. The central picture is that two electrons can form a pair at low temperature, called a Cooper pair. The Cooper pairs can be considered as composite bosons: they can form a condensate when the temperature is below a critical temperature T_c . This condensate state of electrons exhibits superconductivity in which current can flow in a conductor without friction. However, most of the highly complex superconductivity systems cannot be explained by such a simple theory.

Creating a pure BEC in the Lab became a long dream of many physicists. Such a clean system can be accurately described by simple theoretical models. Starting from this pure system, interesting effects can be studied in isolation from the complicated environment. With the rapid development of laser cooling and trapping techniques in the 1980s [7–9], physicists finally created BECs with alkali atoms in 1995 [10–12] by combining laser cooling and evaporative cooling techniques. After twenty years, ultracold quantum gases research continues to inspire us and the achievements are far beyond the most optimistic expectations. Experiments and theories grow simultaneously as the complexity of the systems under study is increased. Using a combination of lasers and precisely designed electromagnetic fields, we are adding more control knobs to the system which give us the capability to freely vary system parameters such as the trapping geometries, dimensionality and strength of interaction. Growth

of the complexity of ultracold quantum gas systems allows the subject to cross the borders of traditional atomic physics and to merge with condensed-matter physics, information science and particle physics.

One example of the intersection of ultracold quantum gases with condensed-matter physics is the optical lattice. Atoms can be loaded into optical lattices, which are created by the interference of intersecting laser beams, so that their motion is analogous to the motion of electrons in a crystal lattice [13, 14]. A milestone experiment was the first observation of the quantum phase transition between the superfluid state and the Mott insulator state in a 3D optical lattice [15]. The underlying theory of the phase transition is based on the Bose-Hubbard quantum tunnelling model, introduced in [16] to describe the destruction of superfluidity because of strong interactions and disorder. Subsequently, the superfluid-Mott insulator transition has been observed in 1D and 2D optical lattices [17, 18]. Recently, state of the art quantum gas microscope techniques have opened a new avenue to compare with the theory more precisely through the observation of individual atoms [19, 20]. A better model for the motion of electrons in a crystal lattice is the Fermi-Hubbard model which requires loading fermionic atoms into an optical lattice [21, 22].

Not long after the creation of a BEC in alkali-atom vapours, degenerate Fermi gases were realised with the help of the sympathetic cooling technique [23, 24]. The research on degenerate Fermi gases almost immediately attracted much attention simply because the electron is a fermion and all the constituent particles of matter are fermions. A big advantage of the ultracold gas system is that the interactions between particles can be controlled through a Feshbach resonance [25]. A Feshbach resonance allows direct control of the s -wave scattering length, which characterises the interparticle interaction at low temperature, through the application of a magnetic field. In the case of fermions, a Feshbach resonance smoothly links two different regimes. On one side of the resonance, the weak interaction between atoms of opposite spin leads to the formation of weakly bound Cooper pairs and the physics described by BCS theory emerges. On the other side are tightly bound molecules; these molecules are composite bosons and can undergo condensation. The unitary

regime in the middle contains rich physics [26].

Another breakthrough was the realisation of spin-orbit coupling of ultracold atoms. One challenge of quantum simulation is to emulate the effect of magnetic fields on electrons using neutral atoms. By introducing spin-orbit coupling of neutral atoms, scientists can engineer a vector potential for atoms which is equivalent to that experienced by electrons moving in a magnetic field [27, 28]. These engineered artificial gauge potentials open the door to explore physics in new regimes. Scientists can now tailor quantum systems to have properties which do not even exist in nature.

1.2 The atom chip: cold matter lab on a chip

The original version of the atom chip [29–32] combines the dramatic progress in ultracold quantum gases with the mature technology of the semiconductor industry. Atom chips minimise and integrate components that can create ultracold quantum gases, accurately manipulate and measure them, while controlling both the internal and external degrees of freedom. The atom chip has been shown to be a robust and precise device to manipulate quantum matter [33]. The complexity [34] of an atom chip can easily be scaled up. It is also considered to be a promising candidate which can bring quantum gas systems out of the Lab.

Initial interest in the microscopic magnetic trap was due to the possibility of entering a new regime in which the extension of the ground-state wave function in the trap becomes smaller than the wavelength of the atomic transition line. Microfabricated planar current-carrying wires on a chip were suggested to create such traps [35]. In the early days, loading atoms into these microscopic traps was quite challenging since the trap volume is very small. Many works were focused on guiding precooled atoms with a tailored magnetic waveguide created from free-standing current-carrying wires [36] and microfabricated wires on a chip [37–39]. For efficient loading of a microscopic magnetic trap on an atom chip, two different approaches were developed independently. The first is the Mirror MOT approach: in this scheme the chip surface also serves as a reflective mirror which allows one to cool and trap

atoms close to the surface [33, 40]. In the second approach, atoms are cooled and collected at a different location and subsequently transported to the atom chip surface by magnetic transport [41] or optical tweezers [42].

The first BECs on atom chips were realised shortly after, in 2001 [41, 43]. Since then, research on atom chips has developed rapidly on both the fundamental physics side and the applications side. More and more species can now be trapped and studied on a chip. A Fermi gas has been cooled to degeneracy on an atom chip [44]. Trapped atoms can be excited to Rydberg states near a chip surface [45, 46]. Even deceleration and trapping of molecules has been demonstrated on a chip [47, 48].

Compared to a macroscopic magnetic trap produced by magnetic coils, the geometry of a microtrap created on an atom chip can be easily shaped by patterning a tailored wire structure. It turns out that atom chip microtraps are well suited to realising a one-dimensional geometry [49–52]. A 1D quantum many-body system is exactly solvable [53]. Therefore, the theory can be precisely checked by experiment. A 1D Bose gas also exhibits rich physics, very different from 2D and 3D. One dramatic example is that a 1D Bose gas can become more strongly interacting as its density decreases [54].

The atom chip usually traps atoms close to the surface in the range of micrometers to hundreds of micrometers. Ultracold atoms or a BEC can be considered as a sensitive probe to study effects that only dominate when the trap is very close to the surface, such as the Casimir-Polder interaction [55–57] and Johnson noise [58]. Also, the trapped cloud can be used to probe the electron transport within a current-carrying wire [59], the magnetic field near a surface [60, 61] and the microwave field near a surface [62, 63].

A major research topic of the atom chip is the atom interferometer. An atom interferometer enables the study of the matter-wave properties of a BEC. The atom chip turns out to be a robust device to perform interferometry measurements. An atom Michelson interferometer on a atom chip was demonstrated first [64]. A more commonly implemented scheme is to dynamically split a single trap into a double well; this process is analogous to a beam splitter in optics. A simple two current-

carrying wire structure was introduced to perform double-well splitting [65] and this was later demonstrated in an experiment [66]. One drawback of this scheme is that it is difficult to maintain spatial coherence during the splitting of the wavepacket. To overcome this limitation, the Heidelberg group demonstrated a coherent beam splitter based on a radio-frequency-induced double-well potential [67]. Subsequently, the same group reported a full Mach-Zehnder interferometer for BECs on an atom chip by recombining the two separated wavepackets [68, 69].

The atom chip offers robust creation of a BEC and highly controlled manipulation of the cloud motion. And it is easy to scale up, which makes the atom chip a promising candidate for quantum gate operation [70, 71]. Experiments have shown that long coherence times of superposition states of the trapped atoms can be maintained close to a chip surface [72, 73], which is crucial for quantum gate operation. An important tool in these systems are state-dependent microwave potentials, which offer a unique way of controlling the interaction between internal states, since the usual magnetic Feshbach resonance cannot be implemented in an atom chip experiment. The Munich group demonstrated an atom interferometer with a state-sensitive beam splitter [74]. Furthermore, by precisely controlling the interactions, spin squeezing and multi-particle entanglement has been achieved on an atom chip [75], which may be useful for a chip-based atomic clock [76] and an interferometer operating beyond the standard quantum limit. In addition, optical fibre cavities on an atom chip have demonstrated the capability of single-atom control [77–79]. This looks promising for the demonstration of a gate operation on an atom chip.

The original atom chip configurations were based on single-layer current-carrying wires deposited on substrates. In recent years, many new technologies and techniques have been conceived and implemented. As a natural extension of a single-layer atom chip, multilayer atom chips have been fabricated and implemented for versatile manipulation of atoms [80], and superconducting atom chips [81, 82] and hybrid atom chips integrated with photonics devices [83] have been implemented.

In the Swinburne group, we have chosen permanent magnets as an alternative to current-carrying wires. Permanent magnetic materials have the advantage that

large magnetic field gradients and curvatures can be produced, free from technical noise and fluctuations, compared to current-carrying wires. The required magnetic field profile can be produced by patterning the magnetic structure through well-established nano-fabrication technology.

1.3 Hybrid atom chip with a magnetic lattice

Permanent magnetic materials were first used as magnetic mirrors [84–89] in the field of atom optics. Researchers then demonstrated the capability of loading atoms into micromagnetic traps [90, 91] based on permanent magnets and even to achieve a BEC in such traps [92–94]. In the Swinburne group, we are particularly interested in designing a lattice potential structure with a permanent magnetic thin film. Compared to the widely used optical lattices, magnetic lattices offer several unique features: they have a large design flexibility allowing a variety of lattice geometries; the lattice period is not limited by the wavelength of the optical lattice laser; magnetic traps are state-selective so that RF evaporative cooling is allowed in a magnetic lattice trap and RF spectroscopy [95, 96] can be used as a powerful probe for the measurements.

Several proposals based on different techniques have been suggested to realise a magnetic lattice, such as an array of current-carrying wires [97–99], an array of superconducting vortices [100], synthesising a spatially periodic magnetic field based on pulsed gradient magnetic fields [101] and RF-dressed magnetic lattice potentials [102]. Here, we will focus only on the development of patterned permanent magnetic films and summarise the brief history.

A 1D magnetic lattice is the easiest structure that can be transferred from a magnetic mirror configuration. In 2005, the Imperial College group created a 1D 100 μm -period magnetic structure based on a sinusoidally magnetised videotape [92]. They demonstrated loading ^{87}Rb $|F = 2, m_F = +2\rangle$ atoms and achieving a BEC in one of the lattice traps. The dynamics of atoms confined in a single magnetic waveguide was studied. Later, in 2010, the Imperial College group demonstrated the

capability of selectively loading one or several lattice sites [103], and implemented an effective transport of the confined atoms over long distances, up to ~ 1 cm. In 2007, the MIT group implemented a similar type of experiment with $|F = 1, m_F = -1\rangle$ ^{87}Rb atoms in a 1D $100\ \mu\text{m}$ -period magnetic lattice created by a commercial hard disk [104]. A 1D $4\ \mu\text{m}$ -period magnetic lattice created with current-carrying wires was constructed in the Tübingen group who demonstrated the diffraction of a BEC [105, 106].

In 2008 the Swinburne group produced a 1D magnetic lattice structure on a TbGdFeCo film with a period scaled down to $10\ \mu\text{m}$ [107]. About 150 lattice sites were loaded with pre-cooled ^{87}Rb atoms in the $|F = 2, m_F = +2\rangle$ state. The dynamics of the reflection of an ultracold atomic cloud from such a lattice potential was also studied [108, 109].

In parallel, the Amsterdam group created a 2D rectangular magnetic lattice with periods of 22 and $36\ \mu\text{m}$ in orthogonal directions using FePt magnetic film [110]. More than 30 lattice sites were loaded with ^{87}Rb atoms in the $|F = 2, m_F = +2\rangle$ state. After improving the loading process they later demonstrated loading over 500 lattice sites and shuttled the trapped cloud across the chip surface by controlling an external magnetic field [111]. RF evaporative cooling was performed to further lower the temperature. However, the final temperature of the trapped cloud was limited by rapid three-body losses [112] and quantum degeneracy could not be reached in individual lattice sites.

In order to reduce three-body losses, the Swinburne group trapped atoms in the $|F = 1, m_F = -1\rangle$ state. The three-body recombination rate for a thermal cloud is roughly three times smaller than for the $|F = 2, m_F = +2\rangle$ state [113, 114]. This change increases the lifetime of the lattice traps and allows one to perform more efficient RF evaporation. Finally, we realised BECs across more than 100 sites of a 1D $10\ \mu\text{m}$ -period magnetic lattice. Single-site resolved imaging provided the capability to simultaneously measure RF spectra of each individual lattice site *in situ*. When slowly ramping down the final RF frequency, the RF spectra changed from a thermal Boltzmann distribution with a broad width to a bimodal distribution

and finally to reach a narrow peak with an inverted approximately parabolic shape which signified an almost pure BEC [95, 96].

A 2D magnetic lattice potential with equal barrier heights in different trapping directions is crucial for equal tunnelling. Earlier proposals for creating such a 2D lattice are difficult to implement because of the complexity of fabrication [115, 116]. In 2010, Schmied et al. [117] developed a linear programming algorithm to design tailored lattices of magnetic microtraps based on patterned magnetised films. The designed pattern is a one-layer binary structure containing only a full magnetisation area and a non-magnetisation area. Such a simple pattern can be easily adapted to current nanofabrication processes. Nearly arbitrary geometries of trapping potential patterns, in principle, can be produced with desired constraints.

Inspired by this optimised program, both the Amsterdam group and our group developed new types of magnetic lattices. $10\ \mu\text{m}$ -period square and triangular lattices were fabricated with FePt film by UV lithography by the Amsterdam group [118]. Cold atoms were successfully loaded into hundreds of lattice traps. Such a period is suitable for quantum information science with long-range interacting Rydberg atoms. On the other hand, our group fabricated a structure with four magnetic lattice structures having periods down to $0.7\ \mu\text{m}$ on a Co/Pd multi-atomic layer film [119]. The sub-micron-period lattice is designed to allow us to explore quantum tunnelling effects. It is a promising candidate as a quantum simulator of 2D systems in condensed matter science.

1.4 Overview of thesis

This thesis reports on the design and fabrication of a new magnetic lattice atom chip. The Co/Pd magnetic film contains four lattice structures: a 1D $5\ \mu\text{m}$ -period structure, a 1D $0.7\ \mu\text{m}$ -period structure, a $0.7\ \mu\text{m}$ -period square lattice structure and a $0.7\ \mu\text{m}$ -period triangular lattice structure. In addition, a new atom chip has been fabricated using direct bonded copper. This atom chip contains four pairs of separate U-wire and Z-wire traps which allows us to prepare ultracold atom

clouds in the different magnetic lattices. Ultracold atoms or BECs can be brought very close ($\sim 0.3 \mu\text{m}$) to the $0.7 \mu\text{m}$ -period magnetic film structures. The atom-surface interaction is first studied. We then study the reflection of atom cloud from the $0.7 \mu\text{m}$ -period triangular magnetic potential, and the loading of atoms into the $0.7 \mu\text{m}$ -period triangular magnetic lattice traps.

The structure of the thesis is as follows:

In Chapter 2 we first summarise the basic knowledge of magnetic trapping and Bose-Einstein condensation. Then the interaction between the atoms and a chip surface is discussed. In the last part of the chapter, we discuss the design principle of the magnetic lattice.

The fabrication and characterisation of the magnetic film and atom chip are presented in Chapter 3. This chapter starts with the features of the Co/Pd magnetic film. Then we introduce the design and fabrication of the sub-micron-period magnetic lattice. The fabricated magnetic film is characterised by different methods. The newly designed atom chip is presented in the last part of the chapter.

The experimental apparatus is described in Chapter 4 and the experimental procedure for preparing a BEC is discussed. The properties of the BEC and the Z-wire trap are presented. This is the starting point for further experiments on magnetic lattice loading.

Chapter 5 presents the main results of this thesis. First, the interaction between Z-wire trapped ultracold atom cloud and the atom chip surface is studied and the reflection dynamics of an atom cloud from the $0.7 \mu\text{m}$ -period triangular magnetic potential is studied. Finally, preliminary results for the trapping of ultracold atoms in a $0.7 \mu\text{m}$ -period triangular magnetic lattice are reported.

Possible future directions are discussed in Chapter 6.

CHAPTER 2

Theoretical background

In this chapter I review fundamental concepts of the magnetic lattice atom chip. These concepts are important for understanding the whole experimental cycle and further for designing a new type of experiment. Starting from the principle of magnetic trapping I discuss the basic wire trap configuration used in our work. Then the process of evaporative cooling is analysed which usually serves as the last step for achieving BEC. Finally, the properties of a BEC are presented. In addition, the atom-surface interactions are discussed since in a magnetic lattice the atoms can be very close to the surface of the chip. In the last part of the chapter, the design methods and basic properties of a magnetic lattice are discussed.

2.1 Magnetic trapping of neutral atoms

In the area of ultracold atom research, atoms are manipulated through interactions with an electromagnetic field. The discussion here follows that in [120]. The principle of magnetic trapping of a neutral atom is based on the interaction of the atomic magnetic moment $\boldsymbol{\mu}$ with an external magnetic field \mathbf{B} . In a classical picture, the atom experiences a potential energy

$$E = -\boldsymbol{\mu} \cdot \mathbf{B} = -\mu B \cos \theta. \quad (2.1)$$

The angle θ between $\boldsymbol{\mu}$ and \mathbf{B} is constant because of the rapid Larmor precession of $\boldsymbol{\mu}$ around the magnetic field axis. In a quantum mechanical picture, the Zeeman energy levels of an atom with angular momentum \mathbf{F} are

$$E_{F,m_F} = \mu_B g_F m_F B, \quad (2.2)$$

where μ_B is the Bohr magneton, g_F is the Landé g-factor of the angular momentum state F and m_F is the magnetic quantum number associated with the projection of \mathbf{F} onto the direction of \mathbf{B} . The classical term $\cos \theta$ is now replaced by m_F/F ; the classical picture of constant θ is equivalent to the atom remaining in a state with constant m_F .

An atom trap requires a local minimum of the magnetic potential energy, Eq.(2.2). For $g_F m_F > 0$ atoms “low-field seekers” require a local magnetic field minimum; while for $g_F m_F < 0$ atoms “high-field seekers” require a magnetic field maximum; and atoms in a state with $g_F m_F = 0$ are not influenced by the magnetic field to lowest order. Since no local magnetic field maxima are allowed in a source-free region according to Maxwell’s equations [121, 122], only low-field seeking states can be trapped with static magnetic fields.

When a low-field seeking atom is confined in a magnetic trap, it oscillates around the trap bottom. The atom experiences a changing magnetic field in its moving frame because of this oscillation and a transition to a high-field seeking state can be induced. The trap is only stable if the atom’s magnetic moment adiabatically follows the direction of the magnetic field. This requires that the rate of change $\dot{\theta}$ must be slower than the precession of the magnetic field:

$$\frac{d\theta}{dt} \ll \omega_L = g_F m_F \mu_B B / \hbar. \quad (2.3)$$

When the trap bottom reaches zero (or very small) magnetic field B , the condition in Eq.(2.3) can be violated. In this case, the precessing angle changes when an atom passes through the zero magnetic region. So transitions between m_F levels can occur and bring atoms to untrapped states. This trap loss mechanism is known as a Majorana spin flip [123].

2.2 Magnetic traps on atom chips

Instead of using magnetic coils as in a standard BEC experiment, magnetic traps created on an atom chip use lithographically patterned current-carrying wires. Many of the developed microfabrication techniques in the semiconductor industry can be incorporated in an atom chip experiment. An atom chip simplifies a BEC apparatus significantly. Magnetic traps with large field gradient and curvature can be produced close to the trapping wires with modest electric currents [29, 30].

2.2.1 Principle of wire magnetic traps

The principle of a simple wire trap can be illustrated by considering the magnetic field created by an infinitely thin long straight wire, carrying a current I , as shown in Figure 2.1, whose magnitude, gradient, and curvature at a distance r from the wire are [29, 30]

$$B = \frac{\mu_0 I}{2\pi r}, \quad B' = -\frac{\mu_0 I}{2\pi r^2}, \quad \text{and} \quad B'' = \frac{\mu_0 I}{\pi r^3}, \quad (2.4)$$

respectively. Here $\mu_0 = 4\pi \times 10^{-7} \text{ N/A}^2$ is the vacuum permeability. By applying a uniform bias field B_0 perpendicular to the wire, the field is cancelled by the field from the current-carrying wire at a distance

$$r_0 = \frac{\mu_0 I}{2\pi B_0}. \quad (2.5)$$

In the vicinity of this line, the magnetic field has the form of a two-dimensional quadrupole field with gradient

$$B'(r_0) = -\frac{\mu_0 I}{2\pi r_0^2} = -\frac{2\pi B_0^2}{\mu_0 I} \quad (2.6)$$

in the plane perpendicular to the wire.

On an atom chip, atoms are trapped with the help of planar current-carrying wires on a chip substrate plus a uniform bias field B_0 , as schematically shown in Fig. 2.2. The substrate provides mechanical stability and efficient heat transport from the wires. The chip wires have a rectangular cross-section: w is the width

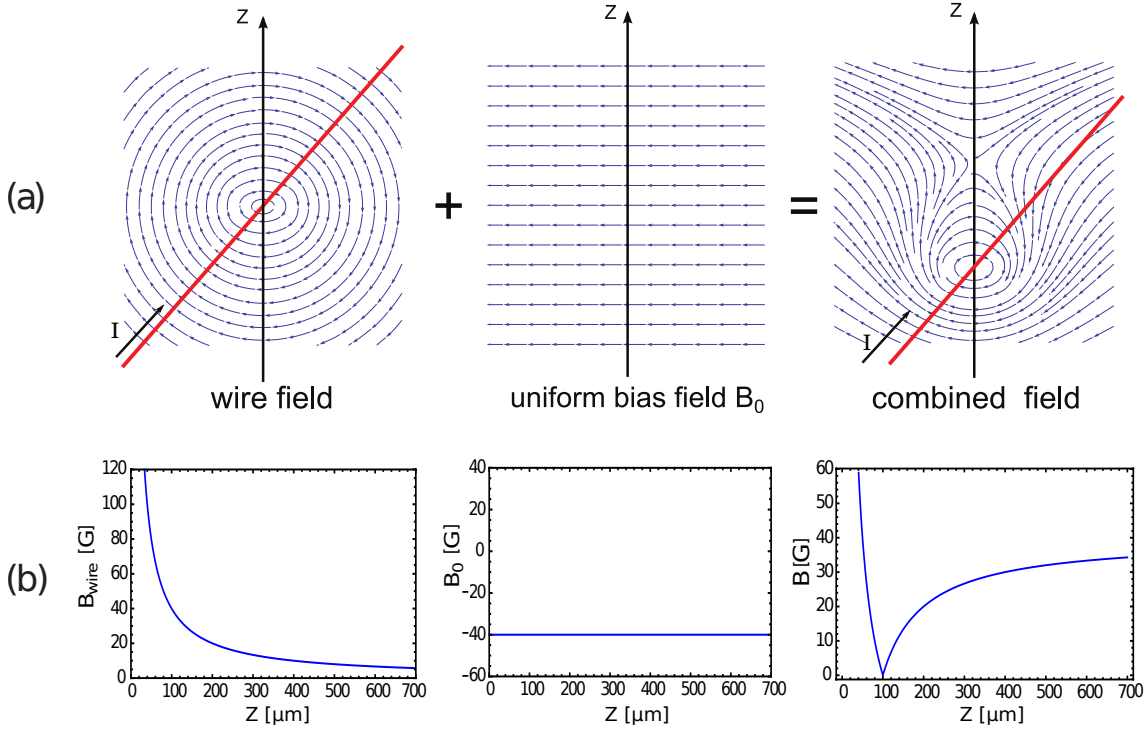


Figure 2.1: (a) A two-dimensional quadrupole field is formed by combining the radial field of a straight wire with a uniform bias field B_0 . Red solid line represents the current carrying wire and blue arrows represent the magnetic field displayed in the plane which is perpendicular to the current wire. (b) Magnetic field magnitude B for a current $I = 2$ A and bias field $B_0 = 40$ G.

and t is the thickness of the wire. The field of an infinitely thin wire is a good approximation to the field of real wires as long as $r_0 \gg w, t$.

The straight wire trap provides two-dimensional confinement and can thus be used to guide atoms on a chip. Traps providing three-dimensional confinement can easily be obtained by either bending the wire ends or adding additional cross wires. The most popular wire trap configurations are the U-shape wire and the Z-shape wire [29,30]. In both cases, the central part of the wire in combination with the bias field forms a two-dimensional quadrupole field for transverse confinement, while the bent wire parts provide an axial confinement.

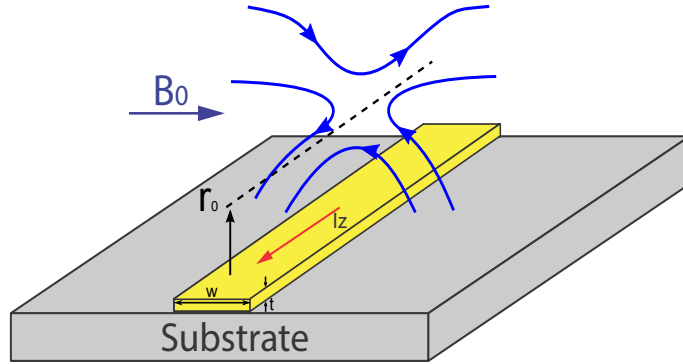


Figure 2.2: Waveguide for neutral atoms formed at a distance r_0 from a lithographically fabricated current-carrying wire of finite width w and thickness t .

2.2.2 U-wire and Z-wire configurations

In the case of a U-wire (see Figure 2.3 for geometry), the field components B_y generated by the two bent wires point in opposite directions and cancel at $y = 0$. The resulting potential is that of a three-dimensional quadrupole trap, with field zero at $y = 0$ and $z = z_0$.

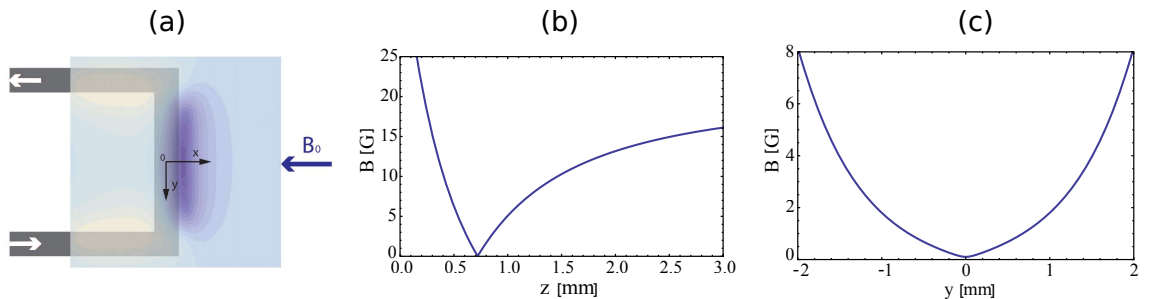


Figure 2.3: Quadrupole U-wire trap: (a) wire layout in the $z = 0$ plane, the orientation of the bias field B_0 and current (white arrow). On top of the wire structure is a contour plot of the magnetic trap in the xy plane, $z = z_0$. Darker region shows the trap minimum, and the trap position is shifted towards $x > 0$. (b)(c) Magnetic field modulus on a line along z and y through the trap centre. The field is calculated for a wire length $L = 5$ mm, $I = 10$ A, $B_0 = 20$ G, wire thickness $t = 0.127$ mm, using the Radia package.

In the case of a Z-wire (see Figure 2.4 for geometry), the field components B_y point in the same direction, adding up to a finite field along y along the trap centre. The result is a three-dimensional Ioffe-Pritchard trap with the trap centre located

at $y = 0$ and $z = z_0$.

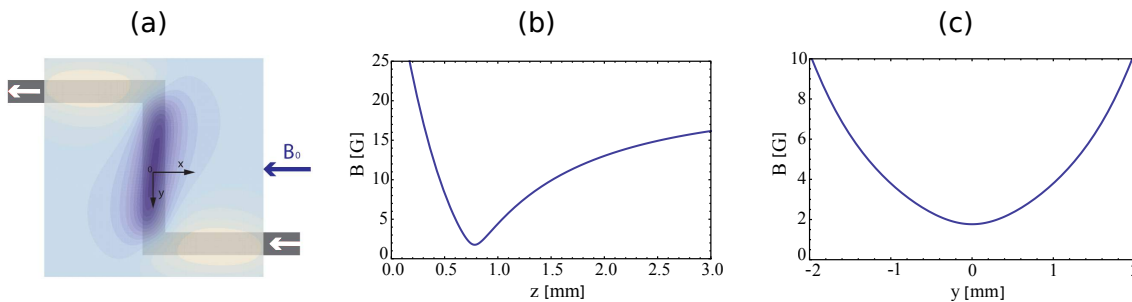


Figure 2.4: Ioffe-Pritchard Z-wire trap: (a) wire layout in the $z = 0$ plane, the orientation of the bias field B_0 and current (white arrow). On top of the wire structure is a contour plot of the magnetic trap in the xy plane, $z = z_0$. Darker region shows the trap minimum, and the trap is tilted along the y -direction. (b)(c) Magnetic field modulus on a line along z and y through the trap centre. The field is calculated for a wire length $L = 5$ mm, $I = 10$ A, $B_0 = 20$ G, wire thickness $t = 0.127$ mm, using the Radia package.

For plotting the U-wire and Z-wire magnetic trap, Fig. 2.3 and Fig. 2.4, we use the Mathematica software with the Radia add-on package which was developed at the European Synchrotron Radiation Facility at Grenoble. Radia is a fast multi-platform software dedicated to 3D magnetostatics computation ¹.

2.3 Mirror magneto-optical trap (MMOT)

In order to load the magnetic trap produced by the atom chip, a mirror magneto-optical trap configuration was invented [29, 40]. For a standard MOT setup [124], Fig. 2.5 (a), six circularly polarised and red-detuned laser beams along three orthogonal axes overlap with a magnetic quadrupole field produced by a pair of magnetic coils arranged in an anti-Helmholtz configuration. The MOT has proven to be a very robust tool for collecting a large cold atomic cloud.

For a mirror MOT, Fig. 2.5 (b), two of the six beams of a normal MOT are replaced by reflected beams from a metallic mirror. Two laser beams are parallel to

¹<http://www.esrf.eu/Accelerators/Groups/InsertionDevices/Software/Radia>

the chip surface (gold mirror) and another two 45° beams form a plane perpendicular to the parallel beams. The axis of the anti-Helmholtz coils is oriented along the direction of one 45° beam. The centre of the produced quadrupole magnetic field is overlapped with the four laser beams. Since the circular polarisation of a laser beam changes helicity upon reflection from the metallic mirror, the MMOT can reproduce the same light-field configuration as a standard MOT. In a mirror MOT configuration, atoms can be collected directly above the chip surface and transferred straight into the magnetic trap produced by the atom chip.

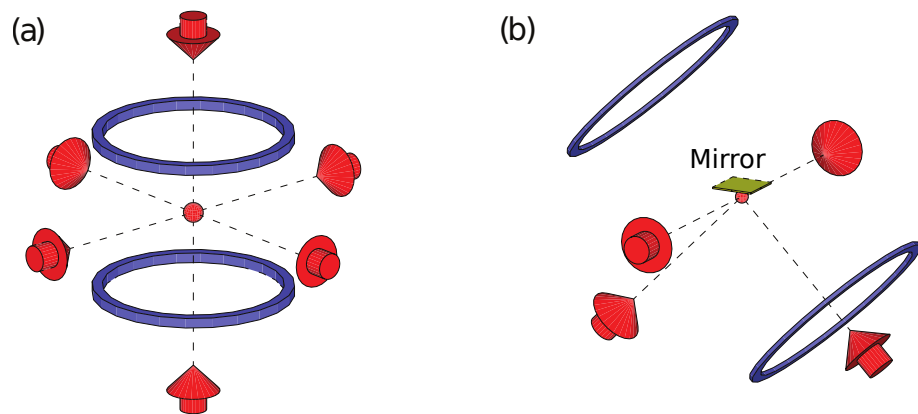


Figure 2.5: Configurations of (a) a standard six-beam MOT and (b) a mirror MOT.

2.4 The thermodynamics of cold atoms

In this section, the thermodynamic properties of the trapped cold atoms are briefly summarised. The trap potential for a thermal cloud trapped in a harmonic trap is given by

$$U(x, y, z) = \frac{1}{2}M (\omega_x^2 x^2 + \omega_y^2 y^2 + \omega_z^2 z^2), \quad (2.7)$$

where M is the mass of atom and ω is the trap frequency. Due to the Maxwell-Boltzmann velocity distribution of the thermal atoms, this gives rise to a Gaussian thermal density distribution in the harmonic trap

$$n_{th}(x, y, z) = n_0 \exp \left[- \left(\frac{x^2}{2\sigma_x^2} + \frac{y^2}{2\sigma_y^2} + \frac{z^2}{2\sigma_z^2} \right) \right], \quad (2.8)$$

where the rms cloud width along each axis $i \equiv x, y, z$ is given by

$$\sigma_i^2 = \frac{k_B T}{M \omega_i^2} \quad (2.9)$$

and the peak density is

$$n_0 = \frac{N}{(2\pi)^{3/2} \sigma_x \sigma_y \sigma_z} \quad (2.10)$$

Therefore, the temperature T of the cloud can be estimated from Eq.(2.9) for a given trap frequency and cloud width. Time-of-flight expansion measurement is a common technique to measure the temperature. In a time-of-flight measurement atoms are released from the trap at $t = 0$ and then the cloud undergoes expansion due to its finite temperature and simultaneously falls under gravity. The evolution of the cloud width is recorded by taking an image of the cloud with a CCD camera. The cloud position and width are given by

$$z(t) = z(0) + \frac{1}{2} g t^2 \quad (2.11)$$

$$\sigma_i(t)^2 = \sigma_i(0)^2 (1 + \omega_i^2 t^2) \quad (2.12)$$

or

$$\sigma_i(t)^2 = \sigma_i(0)^2 + \frac{k_B T}{M} t^2 \quad (2.13)$$

where $\sigma_i(0)$ represents the in-trap rms width.

2.5 Forced evaporative cooling

Evaporative cooling of an atomic cloud trapped in a magnetic trap is based on the preferential removal of atoms above a certain truncation energy ϵ_t from the trap and subsequent thermalization to a new equilibrium state at a lower temperature by elastic collisions of the remaining atoms. Since no photon redistribution is involved, evaporative cooling not only lowers the temperature further but also increases the cloud phase space density significantly. It turns out to be a crucial step in almost all BEC experiments. Detailed discussions about the theory of evaporative cooling of trapped atoms can be found in [125, 126], here only the basic principle of evaporative cooling is introduced.

For a constant truncation barrier ϵ_t , elastic collisions between atoms in a magnetic trap produce atoms with energies higher than ϵ_t which are evaporated from the trap. The evaporation rate can be expressed as [125]

$$\tau_{ev}^{-1} = -\frac{\dot{N}}{N} = -N \frac{\eta e^{-\eta}}{\tau_{el} \sqrt{2}}, \quad (2.14)$$

where the elastic collision rate $1/\tau_{el} = n_0 \sigma_{el} \bar{v} \sqrt{2}$, $\sigma_{el} = 8\pi a_s^2$ is the elastic collision cross section, $\bar{v} \sqrt{2} = \sqrt{\frac{16k_B T}{\pi M}}$ is the average relative velocity between two atoms, and

$$\eta = \frac{\epsilon_t}{k_B T} \quad (2.15)$$

is the truncation parameter. As the temperature drops, η becomes larger and the evaporation rate is exponentially suppressed. In order to force the evaporation to proceed at a constant rate, the trap barrier ϵ_t is reduced in a way that η remains constant. In a magnetic trap, forced evaporation cooling is implemented by coupling the hottest atoms out of the trap using RF radiation which resonantly couples them to non-trapped magnetic sublevels. A resonance occurs when the Zeeman splitting of the magnetic sublevels is equal to the RF frequency:

$$g_F \mu_B B = \hbar \omega_{RF} \quad (2.16)$$

For a 3D magnetic trap, hotter atoms far away from the trap centre have a large Zeeman splitting. When ramping down the frequency of the RF radiation (effectively reduce the trap barrier ϵ_t), the outer shell of the 3D trap filled with hotter atoms is first removed by this RF “knife”. Efficient evaporative cooling results in a smaller, colder and denser cloud, even though atoms are being removed. The efficiency of the evaporative cooling can be described by

$$\alpha = \frac{d \ln T}{d \ln N}. \quad (2.17)$$

α is a constant during the evaporation process (constant η) and the temperature drops to $T(t)/T(0) = [N(t)/N(0)]^\alpha$. In principle, the RF ramping speed should be as slow as possible to obtain efficient evaporation at the expense of a minimal loss in atom number. However, the loss of trapped atoms is not only induced by evaporation, but also suffers from other loss mechanisms. For alkali atoms, the dominant

loss mechanism is usually background gas collisions. τ_{loss} is the time constant for trap loss due to background gas collisions. On the other hand, a fast evaporation could simply lose atoms without considerable cooling if the thermal equilibrium process is slow. Therefore, an important criterion for sustained evaporation is to maintain or increase the elastic collision rate including trap loss mechanisms [125]

$$\frac{\dot{\tau}_{el}^{-1}}{\tau_{el}^{-1}} = \frac{1}{\tau_{el}} \left(\frac{\alpha(\delta - 1/2) - 1}{\lambda} - \frac{1}{R} \right). \quad (2.18)$$

where $\alpha = \frac{\eta}{\delta+3/2} - 1$ and the ratio of $\lambda = \tau_{ev}/\tau_{el} = \frac{\sqrt{2}e^\eta}{\eta}$ for large η , $\delta = 3/2$ for a 3D harmonic trap, $R = \tau_{loss}/\tau_{el}$ is the number of elastic collisions per trapping time; it is also called the ‘‘ratio of good-to-bad collisions’’.

If $\dot{\tau}_{el}(t) < 0$, the collision rate decays rapidly with time, and then the rethermalisation takes an infinite time and the evaporation process stops. By contrast, if $\dot{\tau}_{el}(t) > 0$, exponential growth of the collision rate allows a faster than exponential growth in the phase space density. This is known as runaway evaporation. Therefore, runaway evaporation requires

$$R \geq R_{min} = \frac{\lambda}{\alpha(\delta - 1/2) - 1}. \quad (2.19)$$

Equation (2.19) sets requirements on the initial conditions for the evaporation to reach BEC. Figure 2.6 shows the minimum number of elastic collisions per trapping time R_{min} versus the truncation parameter η . In order to have runaway evaporation and a sustainable increase in the phase space density, we must prepare the initial condition within the blue area.

2.6 Theory of Bose-Einstein Condensation

Bose-Einstein condensation is a macroscopic occupation of the ground state of the system by bosonic particles when the temperature is below a critical temperature T_c^0 . The discussion in this section follows mainly ref. [127]. At temperature T the total number of particles is given, in the grand-canonical ensemble, by

$$N = \sum_{\varepsilon_i} \frac{1}{\exp[\beta(\varepsilon_i - \mu)] - 1}, \quad (2.20)$$

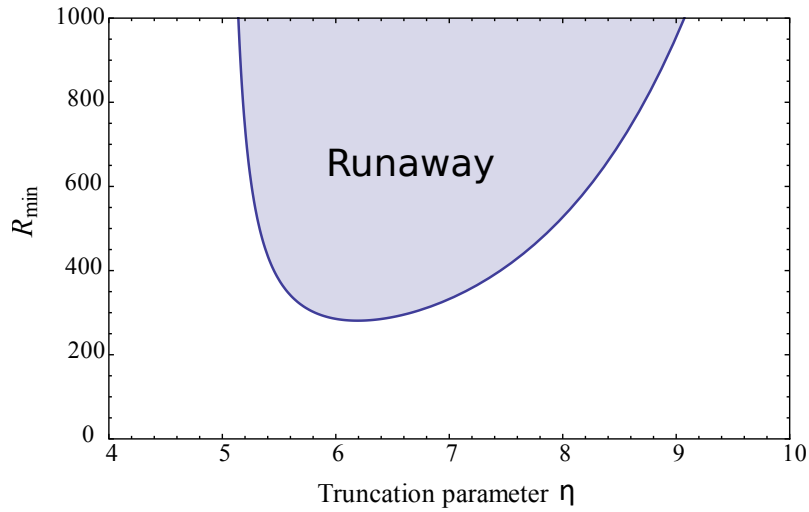


Figure 2.6: Threshold for runaway evaporation. Solid blue line shows the minimum ratio R_{min} of good-to-bad collisions versus truncation parameter η for a harmonic trap potential, $\delta = 3/2$ [125].

where μ is the chemical potential and $\beta = (k_B T)^{-1}$. First, we consider N atoms trapped in a harmonic trap $U(x, y, z)$, Eq.(2.7), and neglect the atom-atom interaction. In this case, the many-body Hamiltonian is the sum of single-particle Hamiltonians, where the eigenenergy of the single-particle Hamiltonian in the i^{th} state is given by

$$\varepsilon_i = \left(n_x + \frac{1}{2}\right) \hbar\omega_x + \left(n_y + \frac{1}{2}\right) \hbar\omega_y + \left(n_z + \frac{1}{2}\right) \hbar\omega_z \quad (2.21)$$

and $\{n_x, n_y, n_z\}$ are non-negative integers. The total particle number N can be written as the sum of the number of atoms in the ground state N_0 and the number of atoms in all excited states. N_0 can be on the order of N when the chemical potential is equal to the energy of the lowest state, $\mu = \hbar(\omega_x + \omega_y + \omega_z)/2$. Thus we can write

$$N = N_0 + \sum_{n_x, n_y, n_z \neq 0} \frac{1}{\exp[\beta\hbar(\omega_x n_x + \omega_y n_y + \omega_z n_z)] - 1}. \quad (2.22)$$

In the thermodynamic limit $N \rightarrow \infty$, we can assume that the level spacing becomes smaller and smaller so that the sum can be replaced by an integral:

$$N = N_0 + \int_0^\infty \frac{dn_x dn_y dn_z}{\exp[\beta\hbar(\omega_x n_x + \omega_y n_y + \omega_z n_z)] - 1}. \quad (2.23)$$

This integral Eq.(2.23) can be easily calculated. One finds

$$N - N_0 = \zeta(3) \left(\frac{k_B T}{\hbar \bar{\omega}} \right)^3, \quad (2.24)$$

where $\zeta(n)$ is the Riemann ζ function and $\bar{\omega} = (\omega_x \omega_y \omega_z)^{1/3}$ is the geometric mean of the trapping frequency. The transition temperature of a BEC can be obtained by imposing that $N_0 \rightarrow 0$:

$$T_c^0 = \frac{\hbar \bar{\omega}}{k_B} \left(\frac{N}{\zeta(3)} \right)^{1/3} = 0.94 \frac{\hbar \bar{\omega}}{k_B} N^{1/3}. \quad (2.25)$$

The T dependence of the condensate fraction for $T < T_c^0$:

$$\frac{N_0}{N} = 1 - \left(\frac{T}{T_c^0} \right)^3. \quad (2.26)$$

In quantum mechanics, the indistinguishability of bosonic particles arises when the wavefunctions of individual particles start to overlap. The phase space density is defined as the number of particles occupying a volume equal to the de-Broglie wavelength cubed

$$\Phi = n \lambda_{dB}^3. \quad (2.27)$$

where n is the density of atoms and the thermal de-Broglie wavelength $\lambda_{dB} = h/\sqrt{2\pi M k_B T}$. From the above discussion, when the phase space density Φ is on the order of one or greater, the de-Broglie waves of the individual bosons have significant overlap and the Boltzmann distribution is replaced by Bose-Einstein distribution.

For a bosonic gas confined in a 3D uniform trap, the BEC transition temperature is $T_c^0 = \frac{2\pi}{[\zeta(3/2)]^{2/3}} \frac{\hbar^2 n^{2/3}}{M k_B}$ [128], and the corresponding phase space density is $\Phi_c = \zeta(3/2) = 2.612$. For a bosonic gas confined in a 3D harmonic trap, as we discussed in this section, $T_c^0 = \frac{\hbar \bar{\omega}}{k_B} \left(\frac{N}{\zeta(3)} \right)^{1/3}$, and the corresponding phase space density is $\Phi_c = \zeta(3) = 1.202$.

2.6.1 Thomas-Fermi approximation

The previous discussion ignores the effect of atom-atom interaction. However, to understand the condensate properties it is important to include the interactions. Applying a mean-field approach to treat this problem leads to the Gross-Pitaevskii (GP)

equation

$$i\hbar \frac{\partial}{\partial t} \psi(r, t) = \left(\frac{-\hbar^2}{2M} \nabla^2 + U(r) + g|\psi(r, t)|^2 \right) \psi(r, t), \quad (2.28)$$

where on the right hand side the first term corresponds to the kinetic energy, the second term corresponds to the external trapping potential, the third term corresponds to the interaction due to the mean field produced by the other atoms, $g = \frac{4\pi\hbar^2 a_s}{M}$ is the coupling constant, and a_s is the s -wave scattering length. When $a_s > 0$ the interaction is repulsive and when $a_s < 0$ the interaction is attractive.

The condensate wave function can be written as $\psi(r, t) = \psi(r)e^{-i\mu t/\hbar}$. Therefore, the GP equation, Eq.(2.28), can be expressed as

$$\left(\frac{-\hbar^2}{2M} \nabla^2 + U(r) + g|\psi(r)|^2 \right) \psi(r) = \mu\psi(r). \quad (2.29)$$

Considering a condensate that is confined in a harmonic trap, the ratio between the mean-field interaction energy E_{int} and the kinetic energy E_{kin} is $\frac{E_{int}}{E_{kin}} \propto \frac{N|a_s|}{a_{ho}}$, where $a_{ho} = \left(\frac{\hbar}{M\bar{\omega}}\right)^{1/2}$ is the harmonic oscillator length. In the case of atoms with repulsive interaction, under most experiment conditions, the limit of $Na_s/a_{ho} \gg 1$ is well satisfied. At this limit, the interaction term is strong and dominates, and the kinetic energy term of the GP equation, Eq.(2.29), can be neglected. This is known as the Thomas-Fermi approximation:

$$(U(r) + g|\psi(r)|^2) \psi(r) = \mu\psi(r). \quad (2.30)$$

The density profile of the condensate in the Thomas-Fermi approximation is

$$n(r)_{TF} = \psi^2(r) = \frac{\mu - U(r)}{g} \quad (2.31)$$

in the region where $\mu > U(r)$, and $n_{TF} = 0$ outside this region. The boundary of the condensate is $\mu = U(r)$. In a harmonic trap, $U(r) = \frac{1}{2}M \sum_i \omega_i^2 r_i^2$, where $i = x, y, z$, and the density profile of the condensate is an inverted parabola. The condensate boundary is an ellipsoid with radius R_i given by

$$\mu = \frac{1}{2}M\omega_i^2 R_i^2 \quad (2.32)$$

So the condensate wave function can be expressed in terms of these radii:

$$\psi(r) = \left(\frac{\mu}{g}\right)^{1/2} \left(1 - \sum_i \frac{r_i^2}{R_i^2}\right)^{1/2}. \quad (2.33)$$

Using the normalisation condition of $\psi(r)$, we obtain a relation between the chemical potential μ and the number of atoms in the condensate

$$\mu = \frac{\hbar\bar{\omega}}{2} \left(\frac{15Na_s}{a_{ho}}\right)^{2/5}. \quad (2.34)$$

2.6.2 BECs in a lattice potential: quantum tunnelling

The GP equation describes weakly interacting Bose gases very well. Two main developments in the past years have made an ultracold gas system accessible to a strongly correlated system. One is the ability to tune the interaction strength in ultracold gases by means of a Feshbach resonances [25]. The other development is the possibility of changing the dimensionality with tailored lattice potentials by means of either optical lattices [13] or magnetic lattices [129]. When a BEC is loaded into a 2D periodic lattice potential, the condensate is usually split into more than 10^5 lattice sites with a mean occupation of 1-2 atoms per site [14]. The atoms can only move through the lattice by tunnelling from one site to the next. Now the tunnelling energy plays the role of the kinetic energy and the effective mass of the atoms can be varied through the lattice potential depth [130]. In this way, the system can enter a strongly correlated regime by dynamically controlling the lattice trap depth. As a result, a quantum phase transition from a superfluid state to a Mott insulator state can occur at a certain critical point [18].

The behaviour of an atomic system trapped in a lattice potential can be described by the Bose-Hubbard model [16, 131]

$$\hat{\mathbf{H}} = -J \sum_{\langle i,j \rangle} \hat{a}_i^\dagger \hat{a}_j + \sum_i \frac{U}{2} \hat{n}_i (\hat{n}_i - 1), \quad (2.35)$$

where the operator \hat{a}_i^\dagger creates an atom at the site i , $\hat{n}_i = \hat{a}_i^\dagger \hat{a}_i$ is the on-site number operator, and the notation $\langle i, j \rangle$ restricts the sum to nearest neighbours only.

J is the tunnelling matrix element and U is the on-site interaction energy. The relative strength between J and U can be controlled by the lattice trap depth V_0 , V_0 is usually measured in units of the recoil energy $E_r = \hbar^2 k^2 / (2M)$. We use the approximate expressions $J/E_r = \frac{4}{\sqrt{\pi}} (V_0/E_r)^{3/4} \exp[-2(V_0/E_r)^{1/2}]$ and $U/E_r = \sqrt{8/\pi} k a_s (V_0/E_r)^{3/4}$ [14] to estimate the tunnelling matrix element and the on-site interaction. The tunnelling time between two neighbouring lattice sites is $\tau_{tunnel} = \hbar/J$ [15].

The magnetic lattice structures in which we are interested can create 2D magnetic lattice potentials with equal trap depths along different lattice directions, as discussed in Sect. 2.8. For a 2D square lattice, quantum Monte-Carlo simulations predict a quantum phase transition between a superfluid state and a Mott insulator state occurs at $(J/U)_c \approx 0.06$ [132]. This has been demonstrated in experiments with optical lattices [18]. Based on this prediction and the above formula, we estimate the relevant parameters which are required to access the quantum phase transition in a 2D square lattice. Our calculations are listed in Table 2.1.

Table 2.1: Calculated parameters for a 2D square lattice with different lattice period a at the superfluid-Mott insulator transition point $(J/U)_c \approx 0.06$.

Period a	0.1 μm	0.7 μm	5 μm	10 μm
E_r	2.76 μK	56 nK	1.1 nK	276 pK
V_0/E_r	6.13	11.9	19.7	22.8
V_0	503 mG	20 mG	0.65 mG	0.19 mG
J	170 nK	820 pK	3.3 pK	0.46 pK
U	2.9 μK	14 nK	55 pK	7.7 pK
τ_{tunnel}	45 μs	9.3 ms	2.3 s	17 s

From these estimates we can see that there is little chance for systems with large lattice periods (5 and 10 μm) to access the superfluid-Mott insulator transition with neutral atoms. A 0.7 μm -period magnetic lattice is a promising candidate to reach this critical point when the magnetic fields are precisely controlled. With further scaling of the lattice period down to 0.1 μm , or even smaller, we enter a regime which

is difficult to achieve with optical lattices. All the energy scales are increased by more than two orders of magnitude compared with a $0.7 \mu\text{m}$ -period lattice. This boosts the quantity J^2/U which is the energy scale associated with superexchange [133].

2.7 Atom-chip surface interactions

In atom chip experiments, the ultracold atoms are trapped at a distance d from the room temperature chip surface, which usually varies from only a few micrometres to hundreds of micrometres. This unique situation of exploring atom-surface interactions has attracted much attention from both an experimental and theoretical side. Atom-surface interactions give rise to additional mechanisms of atom loss, decoherence and heating. The discussion in this section follows the discussion in [134].

2.7.1 Johnson noise

In a conductor of conductivity σ at temperature T , thermal agitation drives the electrons to move randomly, leading to current noise. This effect is known as Johnson noise. The thermal currents exist in any conductor, independent of whether an external current is applied or not. So they exist in both the trapping wires and the reflecting metal mirror on the surface of an atom chip. The fluctuating magnetic field caused by the thermal current noise introduces spin-flip processes, and hence atom loss in a magnetic trap, and finally sets the limit of trap performance near conductors.

At a distance d from a conducting, non-magnetic layer of thickness t , the spectral density of the magnetic field fluctuations is given by [135]

$$B_{i,j}(\omega, d) = \frac{\mu_0^2 \sigma k_B T}{16\pi d} \cdot s_{ij} \cdot g(d, t, \delta), \quad (i, j = x, y, z) \quad (2.36)$$

where $s_{ij} = \text{diag}(\frac{1}{2}, 1, \frac{1}{2})$ is a tensor which is diagonal in the coordinate system of Fig. 2.7, the dimensionless function $g(d, t, \delta)$ depends on the geometry and the skin depth $\delta = \sqrt{2/(\sigma\mu_0\omega)}$ and thus contains the frequency dependence of $B_{i,j}(\omega, d)$. The spectral density is related to the mean-square fluctuations of the magnetic field

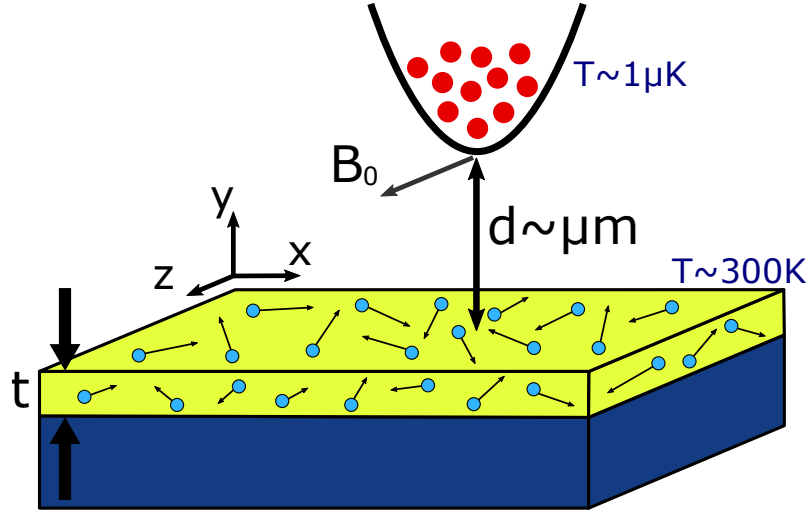


Figure 2.7: Schematic of trapped atoms close to a conducting layer. Green circles represent thermal agitated electrons. Trap loss is caused by spin flips introduced by Johnson noise. Figure adapted from [134].

components

$$\langle B_i^2(d) \rangle = \frac{1}{\pi} \int_0^\infty B_{ii}(\omega) d\omega \quad (2.37)$$

The fluctuating magnetic field couples to the magnetic moment μ of the atoms in the trap. Components perpendicular to μ drive spin flips, which results in decoherence and atom loss from the magnetic trap. The rate of these processes is given by Fermi's golden rule [136–138]. Considering transitions between an initial state $|i\rangle$ and a final state $|f\rangle$ at frequency ω_{fi} , the transition rate Γ is given by

$$\Gamma = \frac{1}{\hbar^2} \sum_{\alpha, \beta=x,y,z} \langle i | \mu_\alpha | f \rangle \langle f | \mu_\beta | i \rangle B_{\alpha\beta}(\omega_{fi}, d), \quad (2.38)$$

where $\mu_\alpha = -\mu_B g_F F_\alpha$ is the magnetic moment in the α direction. As a specific example, we calculate the transition rate between $|i\rangle = |F = 1, m_F = -1\rangle$ and $|f\rangle = |F = 1, m_F = 0\rangle$ at a Larmor frequency $\omega_{fi} = \omega_L$. The trap bottom B_0 is parallel to the surface and we choose this direction as the z -axis in Fig. 2.7. In this case, the F_α component can be written in terms of the raising and lowering operators $F_\pm \equiv F_x \pm iF_y$. Evaluation of the matrix elements yields $|\langle 1, 0 | \mu_x | 1, -1 \rangle| = |\langle 1, 0 | \mu_y | 1, -1 \rangle| = \mu_B / \sqrt{8}$ and $|\langle 1, 0 | \mu_z | 1, -1 \rangle| = 0$. Finally, we obtain [134]

$$\Gamma = \frac{3\mu_0^2 \mu_B^2 \sigma k_B T}{256 \hbar^2 \pi d} \cdot g(d, t, \delta). \quad (2.39)$$

For a skin depth $\delta \gg \max\{d, t\}$, $g(d, t, \delta) \simeq t/(t+d)$ [135]. Therefore, the lifetime due to spin flips caused by Johnson noise is

$$\tau_s = \frac{1}{\Gamma} = \frac{256\pi\hbar^2}{3\mu_0^2\mu_B^2\sigma k_B T} \cdot \frac{d(t+d)}{t} \quad (2.40)$$

2.7.2 Casimir-Polder interaction

An atom in its ground state close to a metallic or dielectric surface feels an attractive potential $V_s(d)$. Such a potential arises due to the interaction of the fluctuating electric dipole of the atom with the fluctuating electromagnetic field, which depends on the distance d from the surface. For large distance $z \gg \lambda_T$, where $\lambda_T = \hbar c/k_B T$ is the thermal photon wavelength ($\lambda_T = 7.6 \mu\text{m}$ for $T = 300 \text{ K}$), thermal fluctuations of the field are dominant. In thermal equilibrium, the potential scales like $-T/z^3$ (Lifshitz or thermal regime). At smaller distances, $\lambda_T \gg z \gg \lambda_{opt}/2\pi$, quantum fluctuations dominate, and the potential scales like $-1/z^4$ (Casimir-Polder regime). For the D₂ line of ⁸⁷Rb atoms, $\lambda_{opt}/2\pi \approx 120 \text{ nm}$. At even smaller distances, $\lambda_{opt}/2\pi \gg z \gg a_0$ (a_0 is the Bohr radius), the potential scales like $-1/z^3$ (van der Waals-London regime). In most atom chip experiments, thermal fluctuations are negligible, ultracold atoms are trapped in a regime where the Casimir-Polder and van der Waals-London interactions are significant.

Therefore, $V_s(d) \approx V_{CP}(d)$, the attractive Casimir-Polder potential V_{CP} is given by [139]

$$V_{CP}(d) = -\frac{C_4}{d^3(d + 3\lambda_{opt}/2\pi^2)}. \quad (2.41)$$

This formula interpolates between the Casimir-Polder and van der Waals regimes. $C_4 = \frac{1}{4\pi\epsilon_0} \frac{3\hbar c\alpha_0}{8\pi} \frac{\epsilon_r - 1}{\epsilon_r + 1} \phi(\epsilon_r)$ [55] is the Casimir-Polder coefficient, where $\alpha_0 = 5.25 \times 10^{-39} \text{ Fm}^2$ is the static atomic polarisability for a ground state Rb atom, $\phi(\epsilon_r)$ is a numerical factor [140] that depends on the relative permittivity ϵ_r of the top surface layer, ϵ_0 is the vacuum permittivity and c is the speed of light. In our experiment, in which silica film is coated on top of the magnetic lattice atom chip, C_4 is taken to be $8.2 \times 10^{-56} \text{ Jm}^4$ for $\epsilon_r = 4.0$ and $\phi(\epsilon_r) = 0.771$.

In the absence of atom-surface interactions, the trap depth would be given by the

value of the trapping potential at the surface. The trapping potential for a harmonic magnetic potential can be expressed by

$$V_t(z) = \frac{1}{2}m\omega_t^2(z - d)^2 \quad (2.42)$$

The trapping potential is truncated at the chip surface, and the trap depth is given by $V_t(0) = \frac{1}{2}m\omega_t^2d^2$. According to this estimation, the trap depth reaches zero only when the trap position is at the chip surface ($d = 0$). However, the attractive Casimir-Polder potential V_{CP} lowers the trap depth to V_b , and makes the trap disappear at finite distance $d > 0$. Figure 2.8 (a) shows the combined potential $V_t(z) + V_{CP}(z)$ seen by an atom close to a silica surface.

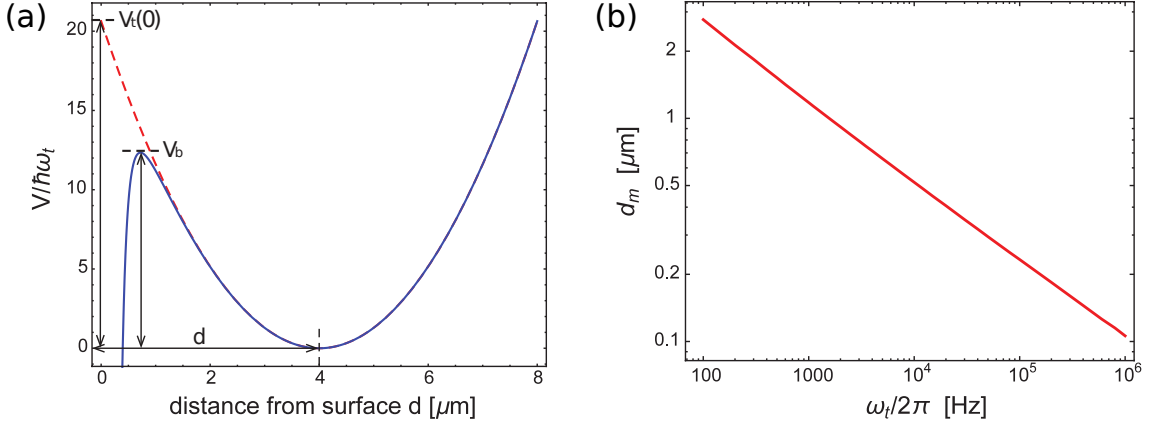


Figure 2.8: (a) Decrease in trap depth due to the attractive surface potential. Red dashed line shows the trapping potential of a harmonic trap V_t . Blue curve shows the combined potential of V_t and the Casimir-Polder interaction V_{CP} . The trap frequency is $\omega_t/2\pi = 300$ Hz and the trap position is $d = 4 \mu\text{m}$. (b) Calculated minimum trap-surface distance d_m versus trap frequency ω_t .

We now wish to determine the minimum trap-surface distance d_m required to trap atoms of energy $E = \zeta\hbar\omega_t$, where ζ is a constant. From the requirement $V_b(d_m, \omega_t) = \zeta\hbar\omega_t$, d_m can be calculated numerically as a function of ω_t . A limiting condition is $\zeta = 1/2$, since the lowest bound state is $1/2\hbar\omega_t$ for a harmonic trap. The result is shown in Fig. 2.8 (b).

In conclusion, it is possible to manipulate atoms at a distance of a few hundred nanometers from the chip surface with ω_t in the range of several kHz to hundreds

of kHz. Such trap frequencies are indeed realistic. One example is the magnetic lattice traps based on tailored permanent magnetic structures. As we will show in Sect. 5.2, trapping frequencies with hundreds of kHz are easily achieved by scaling the lattice period down to $0.7 \mu\text{m}$.

2.8 Sub-micron period magnetic lattices

A periodic array of magnetic micro-traps which we call a magnetic lattice can be created by patterned magnetic films [141], current carrying wires [97–99, 105], vortex arrays in superconducting films [100], or pulsed gradient magnetic fields [101, 142]. Magnetic lattices based on patterned magnetic films have a high degree of design flexibility and may, in principle, be tailored with nearly arbitrary geometries and lattice spacing [117] without restrictions imposed by optical wavelengths.

Since only low-field seeking atoms can be trapped in magnetic lattices, this property allows radio-frequency (RF) evaporative cooling to be performed in the lattice traps and RF spectroscopy to be used to characterise the trapped atoms *in situ* [94, 143]. An array of about one hundred BECs in the ^{87}Rb $|F = 1, m_F = -1\rangle$ state has been achieved in our 1D $10 \mu\text{m}$ -period magnetic lattice [95, 96]. This achievement makes the magnetic lattice a promising candidate for quantum simulation of condensed matter physics. As discussed Sect. 2.6.2, one requirement for such a quantum simulator is that the tunnelling time between adjacent lattice sites needs to be less than the coherence time of the system. In this sense, a $10 \mu\text{m}$ -period magnetic lattice loaded with neutral atoms is too large to study quantum tunnelling. To overcome this limit and access the critical parameters for the superfluid to Mott insulator quantum phase transition [129], it is natural to scale the lattice period down to less than $1 \mu\text{m}$.

Optimised 2D magnetic lattices structures can be designed with a linear programming algorithm developed by Schmied et al. [117]. This algorithm can output an optimised pattern for a single-layer magnetic thin film with perpendicular magnetisation according to input constraints, such as the lattice geometry, lattice period

and lattice trap distance to the film surface. The patterned magnetic film will create a designed lattice potential at certain positions together with required bias fields. Moreover, the lattice potential has equal barrier heights from one lattice site to all nearest neighbours. The optimised pattern is a binary pattern with either a full magnetisation area or a non-magnetisation area and can be readily implemented with e-beam lithography plus reactive ion etching which is suitable to produce sub-micron-period magnetic lattice structures.

To produce a square lattice, only the magnetic field gradient tensor needs to be constrained. In Fig. 2.9 (a), we show the optimised magnetic pattern produced by the algorithm [117]. The pattern produces a square lattice of microtraps at a trapping height $h = a/2$ with equal barrier heights in the x - and y - directions, Fig. 2.9 (b).

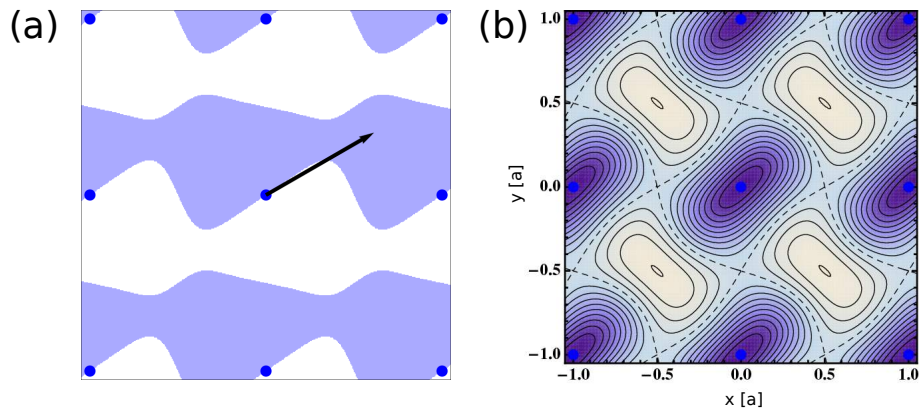


Figure 2.9: (a) Optimised magnetic pattern for a square lattice at a trapping height $h = a/2$. Blue areas are fully magnetised while white areas are non magnetised. Dark blue dots indicate the trap positions and the arrow shows the Ioffe direction. (b) Pseudopotentials of the magnetic pattern in the trapping plane ($h = a/2$). Dark regions represent the potential minima. Figure adapted from [117].

In Fig. 2.10 (a), we present the optimised magnetisation pattern that produces a triangular lattice of microtraps at a trapping height $h = a/2$ with equal barrier heights in three directions (Fig. 2.10 (b)). The required constraints are not only for the field gradient tensor at each trap site, but also for the field gradient vector at one of the barrier positions at $\{x, y, z\} = \{a/2, 0, a/2\}$.

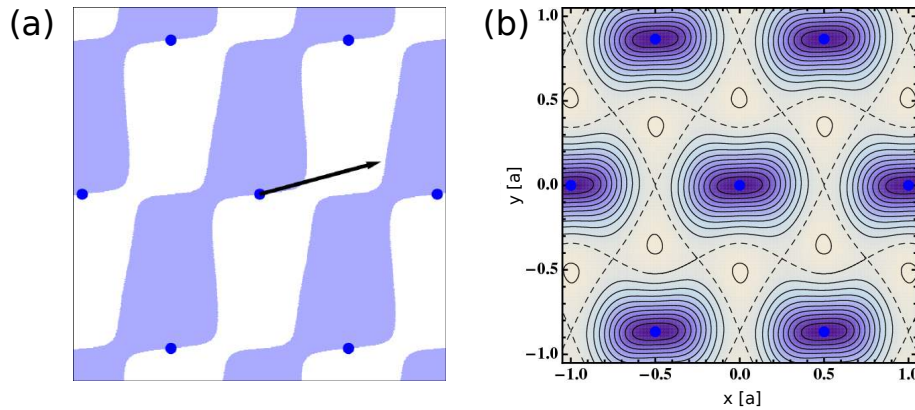


Figure 2.10: (a) Optimised magnetic pattern for a triangular lattice at a trapping height $h = a/2$. Blue areas are fully magnetised while white areas are non magnetised. Dark blue dots indicate the trap positions and the arrow shows the Ioffe direction. (b) Pseudo-potentials of the magnetic pattern in the trapping plane ($h = a/2$). Dark regions represent the potential minima. Figure adapted from [117].

Another program has been developed in our group which takes the optimised pattern structure as a input and calculates the relevant parameter for the optimised magnetic lattice traps, such as trap frequency, trap barrier height, trap bottom at arbitrary bias magnetic fields and including the Casimir-Polder interaction. The results are shown in Chapter 5.

2.9 Summary

In this chapter, the basic theory of magnetic trapping is introduced. The requirement of runaway evaporation is discussed, which is crucial in order to achieve effective evaporative cooling and to produce Bose-Einstein condensation. The properties of a BEC, especially in the Thomas-Fermi regime, are summarised. In addition to this general background theory, atom-surface interactions close to a chip surface, the design method and the trap properties of magnetic lattice traps, which are specific to our magnetic lattice atom chip work, are presented in the last part of the chapter.

CHAPTER 3

Magnetic lattice atom chip design and fabrication

This chapter describes the design, fabrication and characterisation of a hybrid atom chip that combines a patterned permanent magnetic film with a current-carrying wire structure. Four magnetic lattice structures including a 1D $5\ \mu\text{m}$ -period structure, a 1D $0.7\ \mu\text{m}$ -period structure, a $0.7\ \mu\text{m}$ -period square lattice structure and a $0.7\ \mu\text{m}$ -period triangular lattice structure are patterned on a perpendicularly magnetised Co/Pd multi-atomic layer film. The current-carrying wire structure is fabricated with commercial direct-bonded copper (DBC) using wet etching, which is a simple, rapid and low cost method for atom chip fabrication. Finally, the fabricated magnetic lattice film is glued onto the current-carrying wire structure and mounted in an ultrahigh vacuum chamber. The main part of this work has been published in the paper *J. Phys. D: Appl. Phys.* **48**, 115002 (2015).

The Co/Pd multi-atomic layer film was produced by the group of Prof. Dr. Manfred Albrecht at University of Augsburg in Germany. The fabrication of the magnetic lattice structures was carried out at the nano-fabrication facility at the Melbourne Centre for Nanofabrication (MCN) by Armandas Balcytis from the Centre for Micro-Photonics at Swinburne. The magnetic lattice characterisation and DBC atom chip fabrication was carried out by the Swinburne group.

3.1 Co/Pd multilayer mono-atomic magnetic films

Permanent magnetic materials are appealing in atom chip experiments because of the possibility of providing inherently stable magnetic traps and a versatile magnetic trapping potential landscape [144]. Metallic multilayers composed of alternating layers of a ferromagnetic transition metal (Fe, Co, Ni) and noble metal (Pd, Pt) [145–147] is one of the most promising permanent magnetic materials. Co/Pd multi-atomic layer magnetic film is the material chosen in our experiment to fabricate the sub-micron period magnetic lattice structure because of the large perpendicular magnetic anisotropy (PMA), high degree of magnetic homogeneity and small grain size (6 nm) [148].

The thermomagnetic properties for Co/Pd film can be tailored by adjusting the thickness of the individual Co and Pd layers and the total thickness of the layered structure. Surface magnetic atoms (Co) have a preferential magnetic polarisation due to the anisotropic environment at the surface. With decreasing Co thickness a perpendicular easy axis of magnetisation for thin Co layer grows. For a thickness below 1.2 nm the magnetisation direction is perpendicular to the film plane. For an ultra-thin (< 0.4 nm) Co layer, which is equivalent to less than two atomic layers, both the top and bottom layers have an interface with Pd and this configuration is usually optimal for the interface anisotropy. Perpendicular magnetic anisotropy and a square hysteresis loop can be obtained when very thin Co layers (~ 0.2 - 0.3 nm) are alternated with slightly thicker Pd layers (~ 0.8 - 2 nm). For a combination of 0.2 nm thick Co and 0.9 nm thick Pd, the films show a maximum saturation magnetisation and anisotropy constant, and also the squareness of hysteresis loop [147]. The enhanced magnetisation is caused by polarisation of the Pd atoms within about 1 nm by the neighbouring Co [147]. Optimum magnetic properties tend to be obtained for a total thickness in the 10-30 nm range. Usually, the saturation magnetisation M_s and the Curie temperature T_{Curie} increase with increasing Co/Pd ratio. The Curie temperature T_{Curie} normally is in the range of 300 to 400 °C.

The magnetic film used in our experiment consists of a stack of 8 bi-layers of

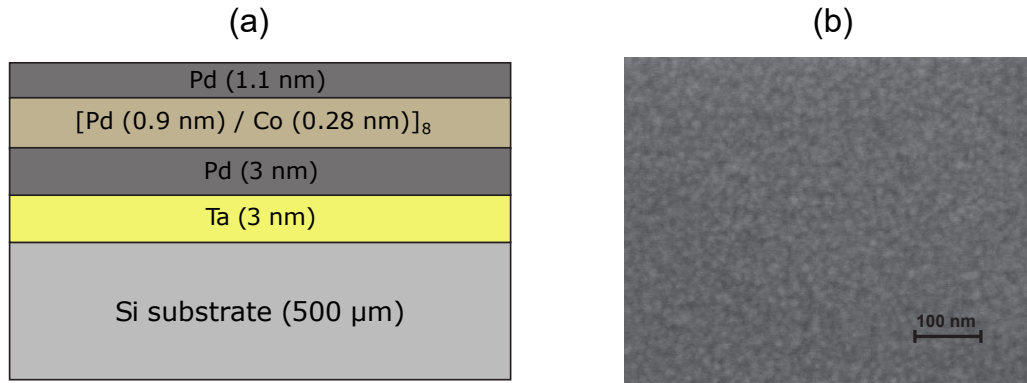


Figure 3.1: (a) Schematic of the multilayer structure of Co/Pd magnetic film. (b) SEM image of the surface of the Co/Pd film. The material shows high homogeneity and small grain size; the measured average grain size is around 10 nm.

Co/Pd, sputter-deposited onto a 500 μm-thick Si(100) substrate with a native oxide layer, as shown in Figure 3.1. This bi-layered film is set on a seed layer of 3 nm-thick Pd and Ta to provide a good (111) texture to start the deposition of the magnetic layers, leading to an improvement of the crystallographic orientation of the layers and to an improvement of the PMA. Eight bi-layers of alternating Co (0.28 nm) and Pd (0.9 nm) are chosen in order to have a large magnetisation and a large PMA. The Co/Pd multilayers are dc magnetron sputter-deposited at room temperature. The argon pressure is adjusted to 3.5×10^{-3} mbar for all depositions, while the base pressure of the deposition chamber is 1.0×10^{-8} mbar. During the depositions the thickness is monitored using a quartz micro balance, which is calibrated by X-ray reflectometry measurements on Co and Pd thin film samples. Finally, a layer of 1.1 nm of Pd is deposited on top of the stack to provide protection against oxidation.

3.2 Co/Pd film characterisation

The Co/Pd multilayer film is magnetised in a strong (~ 1 T) magnetic field created by an electromagnet ¹. The film is positioned perpendicular to the external

¹1½-inch electromagnet type C from Newport Instruments

magnetic field. An accompanying setup for magneto-optical Kerr effect (MOKE) measurements consisting of the electromagnet, a diode laser (780 nm), polarising optics and a sensitive photodetector is used to monitor the dynamic process of the magnetisation. Linearly polarised light experiences a rotation of the polarisation plane, a Kerr rotation, when reflected from a magnetic material. The degree of rotation is proportional to the magnetic moment at the film surface but is also strongly dependent on other parameters such as the composition of the magnetic material, the magnetisation direction, the angle of incidence, the probe laser wavelength and any coating layers on the magnetic material. Because of this, MOKE is normally used for qualitative analysis of a magnetic material allowing measurements of the shape of the magnetic hysteresis loop and the coercivity. A magnetic hysteresis loop can be mapped out through monitoring the Kerr rotation.

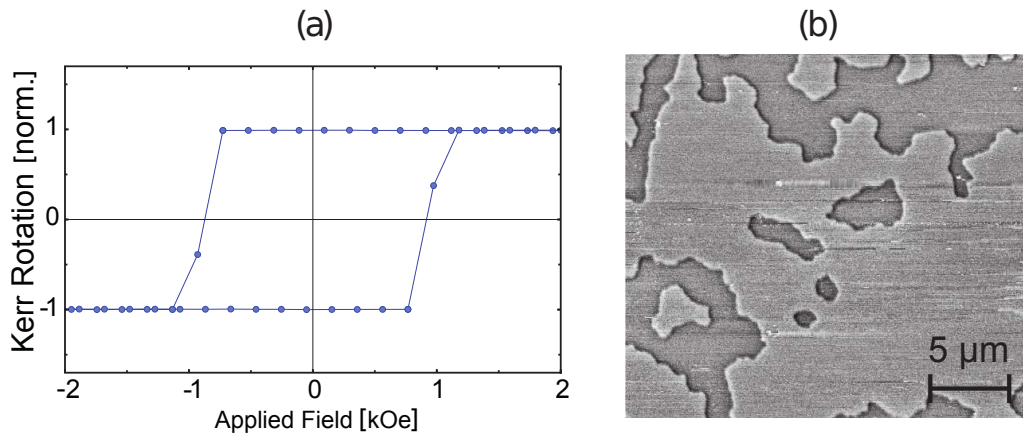


Figure 3.2: (a) Hysteresis loop of the Co/Pd film measured by Kerr rotation. (b) Magnetic force microscope image of the magnetic domain structures of an AC-demagnetised Co/Pd multilayer film. The typical domain size is about $5\ \mu\text{m}$. Figure adapted from [119].

The electromagnet is operated to provide a magnetic field with a maximum strength of $\pm 1\ \text{T}$. The laser is incident on the film at $\sim 45^\circ$ from the normal. The Kerr rotation causes a subsequent change in the photodetector signal which is proportional to the perpendicular magnetic moment. The photodetector signal and the driving current of the electromagnet are simultaneously recorded and the data is post-processed to extract the hysteresis loop. The coercivity of this film measured from the hysteresis loop is $H_c = 1.0\ \text{kOe}$, as shown in Fig. 3.2 (a). The absolute

value of the saturation magnetisation M_s was measured using a superconducting quantum interference device (SQUID) at the University of Augsburg in Germany. The calibrated value for Co/Pd is $4\pi M_s = 5.9$ kG.

The magnetic properties of the Co/Pd film are analysed by an atomic and magnetic force microscope (AFM/MFM). The instrument² is housed in an acoustic hood to reduce vibration during scanning. When using the instrument in MFM mode, the cantilevers are high resolution silicon probes with a 40 nm-thick CoCr magnetic coating. The MFM is operated in two passes. In the first pass the surface topology is measured in semi-contact mode. A phase-sensitive second pass is performed at a constant height from the surface to provide the magnetic force signal. A MFM image of an AC-demagnetised Co/Pd multilayer film showing the magnetic domain structure is illustrated in Figure 3.2 (b). The island shape of the domain structure reveals the magnetisation pointing up or down perpendicular to the film plane due to the strong PMA. The magnetic domains are very stable in extent and position over time.

3.3 Sub-micron-period magnetic lattice structure fabrication

The sub-micron-period magnetic structures were fabricated by e-beam lithography (EBL) plus reactive ion etching (RIE). This method provides high structure resolution and high versatility of arbitrary patterning. Four $1\text{ mm} \times 1\text{ mm}$ lattice structures with different periods are patterned on the Co/Pd magnetic film: a 1D $5\text{ }\mu\text{m}$ -period lattice, a 1D $0.7\text{ }\mu\text{m}$ -period lattice, a $0.7\text{ }\mu\text{m}$ -period square lattice and a $0.7\text{ }\mu\text{m}$ -period triangular lattice.

The Co/Pd film-coated wafer is first cleaned by several ultra-sonication steps in organic solvents: first in acetone, then isopropanol and finally in methanol. After wet cleaning the wafer is blow-dried using dry nitrogen (N_2) gas and the residual

²NT-MDT SPM Solver P7LS microscope

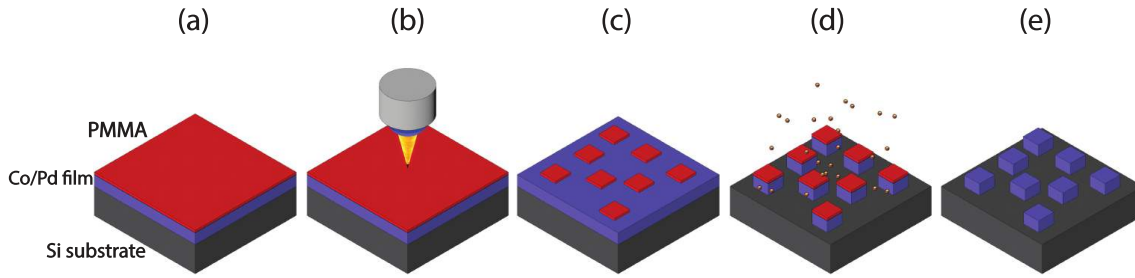


Figure 3.3: Fabrication process for the magnetic lattice structure consisting of (a) spin coating of PMMA resist, (b) EBL exposure, (c) resist development, (d) plasma etching by ion bombardment, and finally (e) removal of the remaining resist. Figure adapted from [119].

solvent is removed by heating on a 180 °C hot-plate for 3 minutes. The fabrication procedure is illustrated in Figure 3.3. First, a 300 nm-thick layer of positive tone PMMA (polymethyl methacrylate) 495k polymer is spin-coated onto the wafer, with a further subsequent 30 second 180 °C hot-plate baking step to remove the remaining anisol in which the PMMA is dissolved. EBL exposure is performed using a Raith EBPG5000plusES tool operating at 100 kV electron acceleration voltage. The 1 mm² write-field afforded by this machine allowed one to expose the entire magnetic lattice structure without moving the sample stage, thereby avoiding any errors of stitching small patterns together. A 5 nm full-width half-maximum electron spot size is employed and scanned along the designated pattern at 50 MHz rate afforded by the pattern generator. The complexity of the lattice structure is the main factor limiting the patterning speed. Exposure durations ranged from 30 min for the 1D grating structures to 2 hours for the square and triangular 2D lattice structures. Energetic electrons destroy the bonds joining the resist polymer chains, thereby locally increasing the solubility of exposed areas in select solvents. Therefore, after resist exposure the pattern is developed for 80 seconds in a 1:3 mixture of MIBK (methyl isobutyl ketone) and IPA (isopropanol). When development is finished the wafer is immersed in IPA, which acts as a stopper. After that the surface is again blow-dried with N₂. The next step involves pattern transfer from the resist to the Co/Pd film itself. This is done through physical sputtering via argon ion (Ar⁺)

bombardment in an inductively coupled plasma reactive ion etching (ICP-RIE) tool (Samco RIE-101iPH). In this process the remaining unexposed resist areas act as a protective mask against the ions. The exposed areas are stripped of Co/Pd film down to the underlying Si wafer (the etching depth ≥ 25 nm), whereas the coated regions remain unaffected. After the dry etching step all of the remaining resist is removed by sonicating the wafer in acetone at 60°C . The elevated temperature is necessary in order to remove the parts of the resist which are cross-linked and hardened during Ar^+ bombardment.

The wafer with the magnetic lattice patterns etched in the Co/Pd film is then coated with a reflective 50 nm layer of Au using magnetron sputtering in a AXXIS (K.J.Lesker) physical vapour deposition system. The sputtering of gold tends to smooth out the ~ 25 nm deep etching gaps on the magnetic film. The unevenness is estimated to be around 10 nm. An additional final 25 nm thick layer of protective silica is deposited over the gold to prevent rubidium atoms from reacting with the gold surface. This is done by means of electron-beam evaporation in the same AXXIS machine. The final fabrication step involves cutting the wafer down to the required $35 \times 40 \text{ mm}^2$ size, whilst keeping the four lattice structures situated at the centre. This was done using a 1030 nm femtosecond laser beam (PHAROS, Light Conversion) and by moving the wafer along the cutting trajectory on a high-precision Aerotech stage. After cutting, the wafer is again washed in acetone and IPA, followed by a final N_2 blow drying step.

3.3.1 Correction for proximity effects

When EBL exposure is performed on large areas ($\sim 1 \text{ mm}^2$) it is found that the uniform dose distribution does not produce a uniform pattern structure. We find that the structure is deformed from the centre area towards the edge, Figure 3.4. It is important to correct for these so-called proximity effects. As electrons impact the resist-coated substrate they become scattered and spread over a wide area ($\sim 25 \mu\text{m}$ radius), far beyond the initial 5 nm spot-size. These secondary electrons cause parasitic exposure of areas around the sub-micron features being defined, which in

turn causes changes in the dissolution rate of the resist. Therefore, the unexposed regions receiving the scattered electrons are also partially developed, which results in the developed patterns having dimensions different from the target ones.

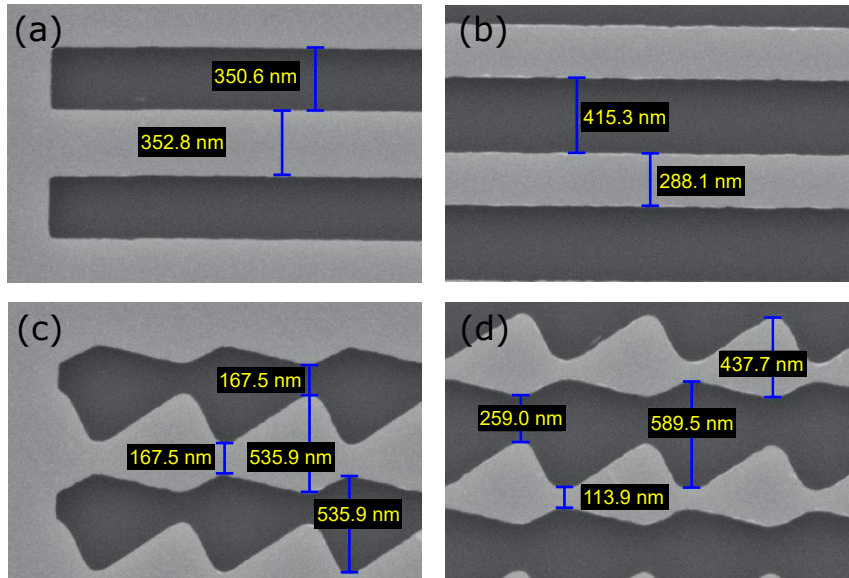


Figure 3.4: Proximity effect in e-beam lithography: fabricated 1D $0.7\ \mu\text{m}$ -period lattice at the edge of the structure (a) and in the centre area (b); fabricated $0.7\ \mu\text{m}$ -period square lattice at the edge of the structure (c) and in the centre area (d).

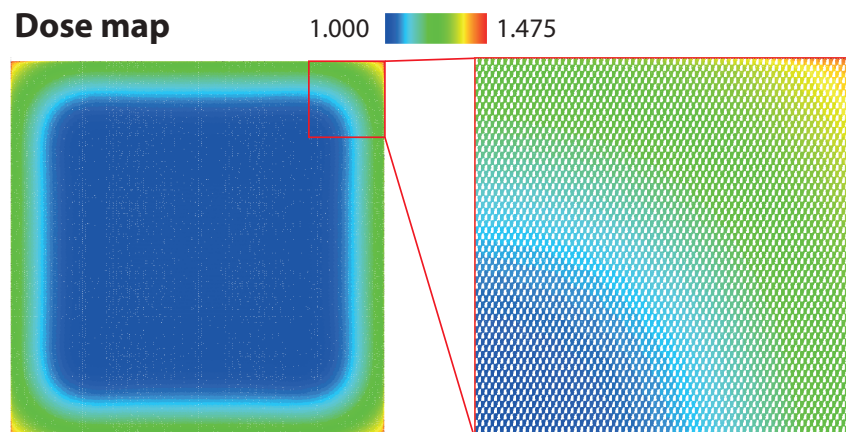


Figure 3.5: Modified exposure dose map of a $0.7\ \mu\text{m}$ -period triangular lattice based on Monte Carlo simulations to correct for the proximity effect in EBL.

Thanks to the serial scanning nature of EBL, proximity effects can be compensated by dose scaling. Instead of using a uniform exposure dose, the dose of different

features is allowed to be modified separately. Hence, after conducting Monte-Carlo simulations to evaluate how the electron beam is scattered and obtaining the point spread function, the exposure dose can be designed to compensate any parasitic exposure. In general terms, when a 1 mm^2 size structure is exposed, the central part is scanned using the base dose whereas a $\sim 25 \mu\text{m}$ wide periphery region is given $\times 1.5$ of the base dose. As an example, an optimised exposure dose for a $0.7 \mu\text{m}$ -period triangular lattice is shown in Figure 3.5.

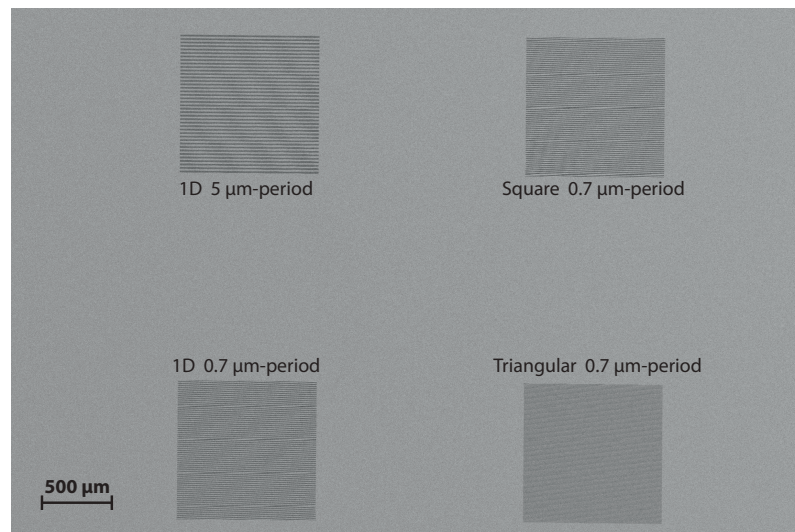


Figure 3.6: SEM image of the centre region of the fabricated magnetic film. Four lattice structures are patterned. The unevenness of the patterned magnetic film is smoothed out by sputtering of 50 nm thick Au layer. The coated magnetic film serves as a high quality reflecting mirror in the experiment.

By scaling the exposure dose and optimising the fabrication procedure, we have produced high quality magnetic lattices with period down to $0.7 \mu\text{m}$. The large size ($35 \text{ mm} \times 40 \text{ mm}$) of the film is designed to allow us to make a large Mirror MOT, Sect. 2.3. Four lattice structures are patterned in the centre of the film, Fig. 3.6. The 50 nm reflective Au layer smooths out the irregularities of the patterned magnetic film (such as the grating structure). No diffraction of MOT light has been observed in the experiment. For the $0.7 \mu\text{m}$ -period 1D, 2D square and triangular lattices, there are more than 1.4×10^3 , 2×10^6 and 1.5×10^6 lattice sites, respectively. Because of the large number of lattice sites, end-effects [115] are small in the central

region and analysis based on an infinite number of lattice sites can be used as a good approximation.

3.4 Film characterisation

The fabricated sample is magnetised and characterised before mounting on the current-carrying atom chip. The surface topology is checked with scanning electron microscope (SEM) images, as shown in Figures 3.7 and 3.8.

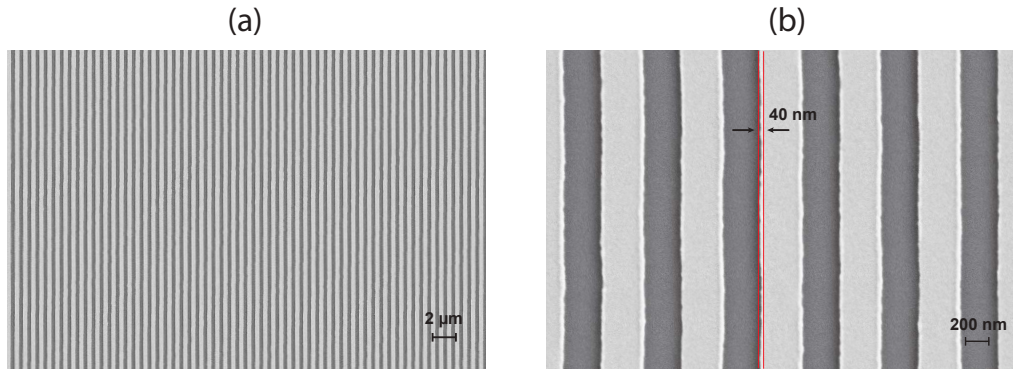


Figure 3.7: SEM images of the 1D $0.7\ \mu\text{m}$ -period magnetic lattice structure. The dark regions correspond to the etched part and the bright regions are the magnetic film. (a) Large-scale image. A Fourier transform of the SEM image reveals that the lattice period is $688\ \text{nm}$. (b) Small-scale SEM image. The edge roughness has an amplitude of about $40\ \text{nm}$. Figure adapted from [119].

A magnetic force microscope (MFM) scan over the magnetised sample is carried out to map the magnetic field over the structures. The semi-contact mode provides a measure of the difference of the phase of the oscillating cantilever-sample system instead of directly mapping the magnetic field over the surface. The tip is driven to oscillate at its resonant frequency with a small amplitude in the vertical z -direction. To lowest order the magnetic force causes a phase shift and a shift in the resonant frequency [149]

$$\Delta\phi \approx \frac{Q}{k_s} \frac{\partial F_z}{\partial z} \propto \frac{\partial^2 B_z}{\partial z^2}, \quad \Delta f \approx -\frac{f_n}{2k_s} \frac{\partial F_z}{\partial z} \propto \frac{\partial^2 B_z}{\partial z^2} \quad (3.1)$$

where Q is the cantilever quality factor, f_n is the natural resonant frequency of the

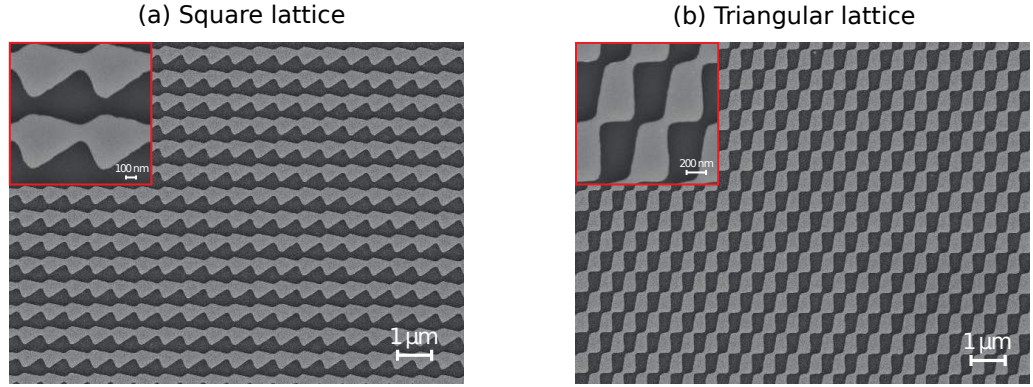


Figure 3.8: SEM images of the fabricated 2D $0.7 \mu\text{m}$ -period (a) square and (b) triangular magnetic lattice structures. The light grey regions correspond to the magnetic film regions which are not etched and the dark grey regions are the etched regions. The insets show the zoomed images.

cantilever tip and k_s is the spring constant. Therefore, the MFM signal is primarily sensitive to the second spatial derivative of the z -component of the magnetic field. If we consider the magnetic field from a 1D magnetic lattice structure, the MFM signal is just proportional to the magnetic field, i.e., an oscillating signal in the y -direction with the period of the structures. The amplitude of the oscillating signal decays exponentially with increasing tip-sample-surface distance, with a decay length $k^{-1} = a/2\pi$, where a is the lattice period. A way to check the quality of the magnetic lattice across the sample is to determine the dependence of the amplitude of the oscillating MFM signal on the distance of the MFM tip from the etched magnetic film. From the oscillating profile of the MFM signal, we measured a period of $a_{osc} = 651 \pm 3 \text{ nm}$, and from the fitted decay length we obtain $a_{osc} = 662 \pm 11 \text{ nm}$, where the uncertainty comes from the residuals of the fits, Figure 3.9. These values are close to the result from the SEM analysis (688 nm) confirming the quality of the periodicity of the 1D structure. Some of the difference between the two measurements comes from the calibration of the spatial dimensions in the MFM apparatus and from high harmonic terms that we have neglected in this analysis. In addition, a $\sim 40 \text{ nm}$ amplitude of the edge roughness is observed in SEM images, Fig. 3.7. Since the distance of the 1D $0.7 \mu\text{m}$ -period magnetic lattice traps to the magnetic film surface is normally

about ~ 480 nm (Sect. 5.2.2), which is much larger than the edge roughness of the grating structure, we expect the potential roughness in the longitudinal direction of the lattice trap is small.

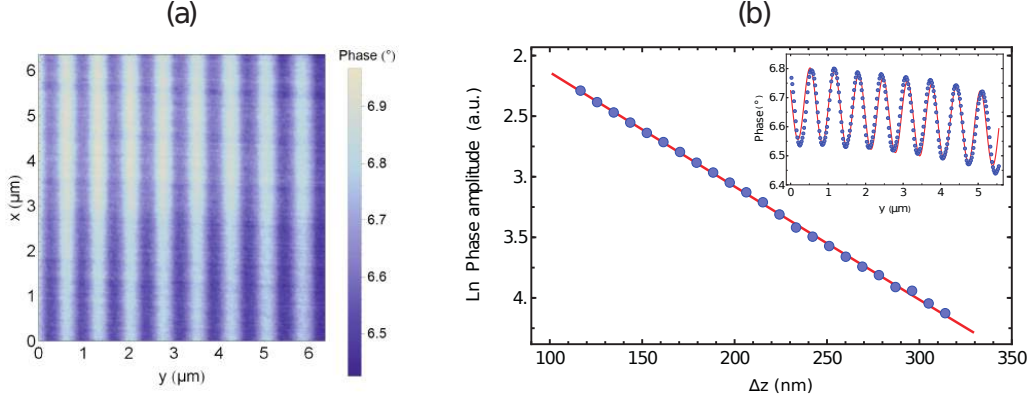


Figure 3.9: (a) MFM measurement of the 1D $0.7 \mu\text{m}$ -period lattice structure with a probe tip height of 50 nm. (b) Plot of the natural logarithm of the amplitude of the MFM signal versus tip height Δz . The red line is a fitted decay curve. Inset: Plot of the profile of the MFM signal in the y -direction at a tip height of 50 nm. The red curve is a fit to the data points for the oscillating signal. Figure adapted from [119].

The SEM images of the fabricated square and triangular lattice structures, Figure 3.8, also show good agreement with the designed pattern. Because of the capability of patterning large areas without moving the sample stage, we avoid any errors of stitching many small patterns together. The drift during the patterning time of ~ 2 hours is negligible.

The magnetic properties of the lattice structure have also been characterised with MFM measurements. The second derivative of the produced magnetic field is calculated for comparison with the measured MFM data. Figure 3.10 shows the surface topology and calculated field for the optimised square lattice. The calculated second derivative is in qualitative agreement with the MFM measurements of the lithographically patterned Co/Pd multilayer. In the MFM data there are several sharper (nearly) horizontal lines that are not reproduced by the simulations. This feature could be explained by the formation of magnetic domains near the boundaries of the structure. However, we cannot rule out the possibility of artifacts introduced

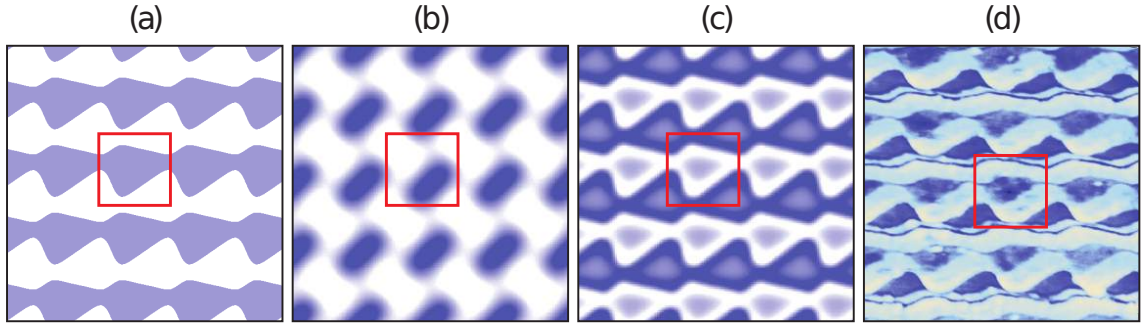


Figure 3.10: (a) Optimised square magnetic lattice pattern generated by the Schmied et al. [117] code. (b) Calculated magnetic potential of a square lattice at height $z = a/2$ from the magnetic film surface. (c) Calculated second derivative of B_z at a constant height. (d) MFM measurement from the fabricated $0.7 \mu\text{m}$ -period square lattice structure. The red square indicates one unit cell.

by the MFM when the surface topology changes at the edges.

3.5 Hybrid atom chip

The magnetic field produced by patterned permanent magnetic films is well suited to tight confinement of ultracold atoms close to the surface, but is too short-range to effectively allow the loading of atoms directly from the background atomic vapour. To support the magnetic film microtrap and facilitate good loading efficiency, a hybrid technology [93] was developed to combine the permanent magnetic film structure with a current-carrying wire atom chip.

The new current-carrying wire atom chip is made with direct bonded copper (DBC). The wire structures are defined by wet etching. This method provides an easy, fast and low cost way to produce a high quality atom chip for cold atom experiments. The atom chip is designed with four separated U/Z-wire structures, which are positioned below each of the four magnetic lattice structures, Fig. 3.11. By choosing different working wires, this allows one to trap atoms below the desired magnetic lattice structure.

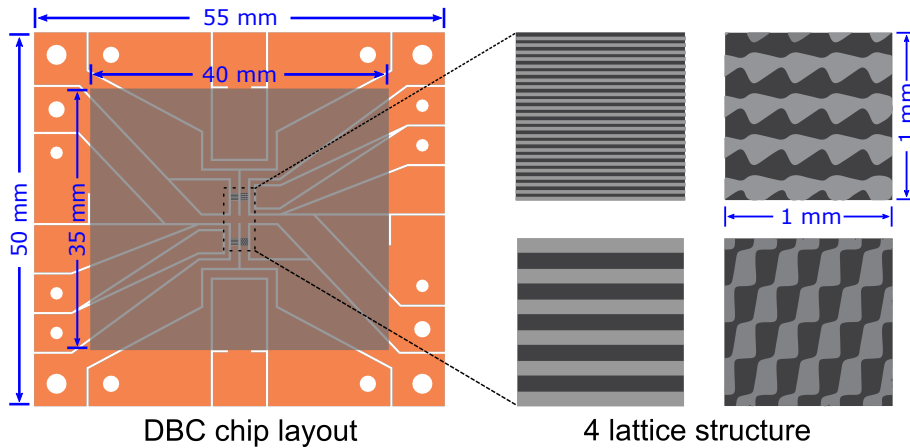


Figure 3.11: Schematic drawing of the designed magnetic lattice atom chip. Four separated U/Z-wire structures positioned beneath the fabricated lattice structures are used to trap the ultracold atom cloud and load the magnetic lattice traps.

3.5.1 Direct bonded copper

Direct bonded copper (DBC) substrates are composed of a ceramic substrate with a sheet of pure copper bonded to one or both sides by the oxygen-copper eutectic. The copper and substrate are carefully heated to $\sim 1065^\circ\text{C}$ which is just below the melting point of pure copper ($\sim 1085^\circ\text{C}$) in a nitrogen atmosphere containing $\sim 1.5\%$ oxygen. Under these conditions, a thin melt layer occurs at the oxide-copper interface that wets the ceramic surface and fills surface irregularities. The resulting bonds are very strong and the material has excellent thermal conductivity³. Aluminium nitride is commonly used as the DBC substrate because of its high thermal conductivity ($\sim 170\text{ W/m}^\circ\text{C}$) and high bond strength.

Evaporation and lift-off metallisation is the standard technique for fabricating high quality wire structures [150]. However, the thickness is limited by the slow deposition rate and substantial material consumption to a few micrometres at maximum. Thicker structures ($\gg 1\ \mu\text{m}$) can be fabricated by electroplating or sputtering of the metal. However, it is still a challenge to make the thickness around

³J. F. Burgess and C. A. Neugebauer, U.S. patent 3,911,553 (October, 1975)

100 μm . DBC substrates are widely used in power electronics due to their high current handling and heat dissipation properties. Because DBC substrates are also UHV compatible they have become a promising material for producing an atom chip [151, 152], especially for atom chips with thicker wires ($> 100 \mu\text{m}$). Another practical benefit of DBC atom chips is the excellent wire to substrate adhesion. Atom chips that use electroplated or evaporated wires need an adhesion layer to avoid delamination of the atom chip wires.

It is straight-forward to produce various rectangular wire cross sections because of the availability of copper layers with different thickness. Quality wire structures can be easily produced by wet etching. Better defined structures are possible using ablative laser micromachining. In the following section, we present a fabricated atom chip based on DBC substrate⁴ with 127 μm -thick copper bonded on both sides.

3.5.2 Atom chip design: four U-wire and four Z-wire configuration

The wire structures of the fabricated DBC atom chip are shown in Figure 3.12 (a). The size of the atom chip is 50 mm \times 55 mm. It contains four separate U/Z wire configurations. As discussed in the previous chapter, the U-wire trap is used in (compressed MMOT) an intermediate step to improve the efficiency of the atom transfer from the initial Mirror MOT to the final Z-wire trap. The Z-wire trap provides a Ioffe-Pritchard magnetic trap. A cold atom sample or a BEC is first prepared in the Z-wire trap. By varying the combination of current and bias field, the atoms can be positioned at different distances from the surface to study the atom-surface interaction. This is also a versatile method for loading atoms into the magnetic lattice traps. The desired U/Z-wire configuration is determined by connecting different pins: 1, 5, 6, 9, 13, 14. For example, when pin 1 and 5 (U-wire), 1 and 13 (Z-wire) are connected, the working trap area is the upper-left. In

⁴From Stellar Ceramics, AlN: 5.4" \times 7.5" \times 0.005" DBCu: 0.012" B/S

each U/Z-wire configuration, the same central segment is shared which is 5 mm long and 1 mm wide. The current-carrying capability of the atom chip wires is tested by running a current up to 40 A (current density 3×10^4 A/cm²) through the U-wire and the Z-wire. The current is turned on for two minutes and no significant increase in temperature is observed. The measured resistance of the U/Z-wire is ~ 4 m Ω . Pins 2 and 3, 10 and 11 provide two wires for RF evaporative cooling or RF spectroscopy. The central segment of these wires is 3.4 mm long and 0.5 mm wide. Pins 7 and 8, 15 and 16 provide two end-wires. Additionally, six small trenches oriented along parallel and perpendicular directions are marks for aligning the magnetic film with the DBC chip. The DBC chip is mounted on a copper heat sink through terminals 4 and 12. The rear side of the atom chip is shown in Fig. 3.12 (b); the shape is designed to match the copper heat sink for efficient heat dissipation.

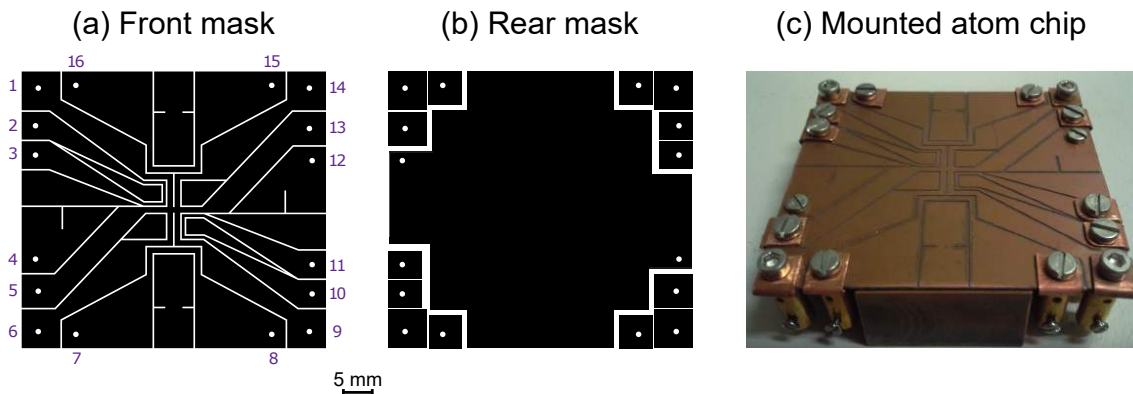


Figure 3.12: (a) Toner mask for the front side of the atom chip. The wire pattern is defined by chemical etching of the area which is not covered by the mask. (b) Toner mask for the rear side of the atom chip. This side is physically attached to a copper block for heat dissipation. (c) Photograph of the fabricated atom chip mounted on the copper block.

The designed wire pattern is transferred from a mask to the copper layer of the DBC substrate by means of UV lithography and wet etching. The process is illustrated in Fig. 3.13. First, the DBC substrate is polished and ultrasonic cleaned. A 20 μ m-thick layer of positive photoresist (AZ4620) is spin-coated on the chip surface. Then the mask is applied on top of the resist. After UV photolithography, the patterned resist serves as a mould for subsequent developing. Here, we choose

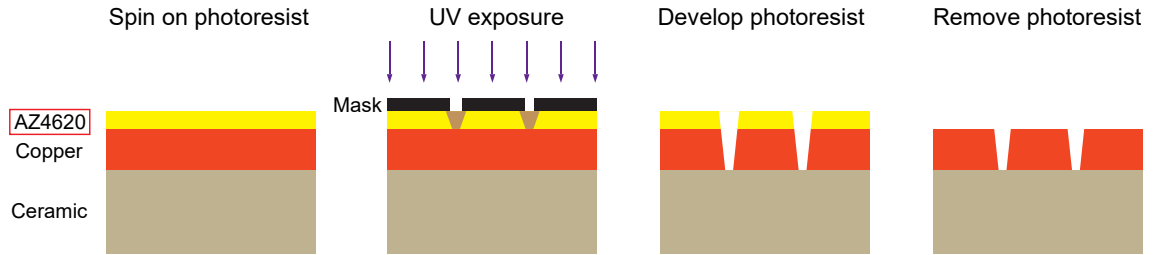


Figure 3.13: DBC chip wire structures are defined by UV lithography with a contact mask. The process steps are described in text.

wet etching to transfer the wire patterns from the resist to the copper sheet. The sample is immersed in a 1:10 mixed solution of ammonium persulphate and water at 60 °C. The uncovered part is completely etched out in one hour. Finally, the remaining photoresist is removed with acetone. Figure 3.12 (c) shows the produced atom chip mounted on a copper heat sink.

3.5.3 Assembly and pre-baking of hybrid magnetic lattice chip

The fabricated magnetic film is glued on the DBC atom chip using a UHV compatible, thermally conductive and electrically insulating two-component epoxy (EPO-TEK H77). A thin layer of epoxy is applied to the copper wire structure, then the magnetic film is carefully aligned with the marks to position it in the centre of the chip. The combined magnetic film and wire structure is cured for one hour on a hotplate at ~ 110 °C so that the epoxy turns into a glassy state to form a strong bond. The complete atom chip is then pre-baked in a separate chamber at a maximum temperature of 110 °C for two days. The baking temperature is chosen on the low side of the affordable temperature. The main concern is to avoid any thermal demagnetisation of the very thin magnetic film and meanwhile this temperature is high enough to remove trapped water vapour and other gases. Fig. 3.14 shows the complete magnetic lattice atom chip.

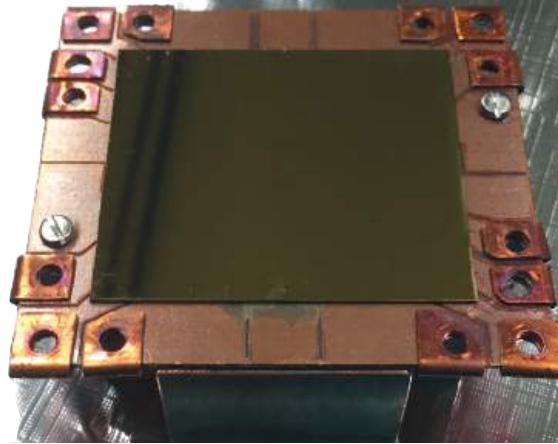


Figure 3.14: Photograph of the complete magnetic lattice atom chip after pre-bake.

3.6 Summary

This chapter presents the design and fabrication of the sub-micron-period magnetic lattice structure film and the supporting DBC atom chip. The general properties of the magnetic Co/Pd multilayer film are discussed. An optimised procedure of e-beam lithography and reactive ion etching is introduced to produce high quality magnetic lattice structures with a period down to $0.7\ \mu\text{m}$. The fabricated magnetic film is characterised with various methods, including SEM for film surface topology and homogeneity and MFM for the produced magnetic field. In order to load atoms into different lattice traps, an atom chip containing four U/Z-wire structures has been fabricated. A simple way to produce an atom chip with a DBC substrate is also introduced.

CHAPTER 4

Experimental setup and BEC preparation

This chapter describes the experimental setup of the magnetic lattice experiment. The setup includes an ultrahigh vacuum system which houses the atom chip and magnetic lattice structure; magnetic field coils surrounding the scientific vacuum chamber to provide the bias magnetic fields to create the magnetic traps; a laser system which provides laser light to cool and manipulate the atoms and to diagnose the properties of the cloud of ultracold atoms and the BEC; and an experimental control system which provides various time sequences for trapping the ultracold atoms and for producing the BEC. Based on this system, we routinely produce a BEC in our daily experiment. The roadmap towards BEC and the properties of a BEC are also discussed in this chapter.

The experimental setup was built by former students who worked on this project and full details can be found in their theses [153–155]. The work described in this chapter mainly includes installing the fabricated sub-micron-period magnetic lattice atom chip in the chamber and producing BEC with this new atom chip in the UHV chamber .

4.1 Ultrahigh vacuum system

Experiments with ultracold atoms require an ultrahigh vacuum (UHV) chamber to isolate the atoms from the environment. In order to reach the condition of runaway evaporation in a magnetic trap (Sect. 2.5), UHV is a crucial requirement for reducing the collisions of the trapped atoms with atoms of the background gas and increasing the lifetime of the magnetic trap. A schematic drawing of the vacuum system is shown in Figure 4.1.

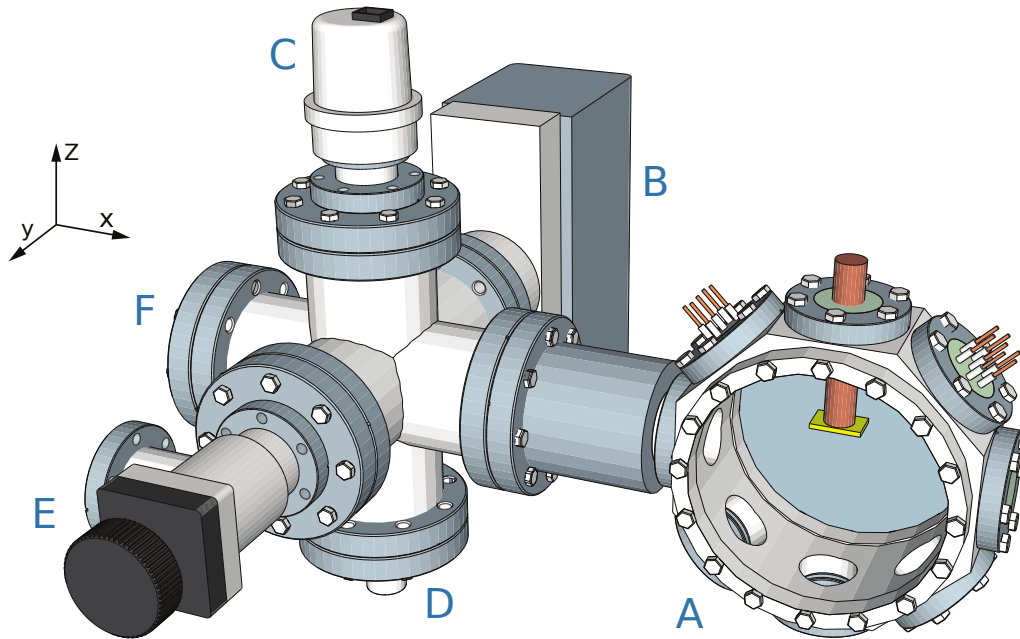


Figure 4.1: Schematic drawing of the vacuum system (without the surrounding magnetic coils and optics). A: octagonal chamber and the mounted atom chip. B: ion pump. C: compact cold cathode gauge. D: getter pump. E: all-metal angle valve. F: access viewport for the imaging and optical pumping beams.

The centre part of the UHV system is a spherical octagon chamber made from (nonmagnetic) 316L stainless steel from Kimball Physics (MCF600-SO200800). This main vacuum chamber has ten CF (conflat) ports including two 6" diameter ports and eight 2.75" diameter ports. The hybrid magnetic lattice atom chip is mounted upside down in the centre of the chamber on an electrical feedthrough having a single copper conducting rod of diameter 20 mm attached to a 2.75" diameter CF

flange through an electrical insulated seal. The copper rod serves as a base connector and a heat sink. One of the 2.75" ports is attached to a six-way cross through an adapter. A combination of ion pump (Varian VacIon Plus 55-StarCell) and getter pump (SAES getter, CapaciTorr D 400-2) are chosen to achieve and maintain UHV. The top port of the six-way cross is attached to a compact cold cathode gauge (Pfeiffer IKR 270) for monitoring the vacuum. Another port of the cross has a 2.75" diameter viewport (F, not visible in Fig. 4.1) which serves as an optical access for the imaging and optical pumping beams. The last port is sealed by an all-metal angle valve to provide access for the initial pumping stage. The electrical connection of the atom chip and two Rb dispensers is provided by two electrical feedthroughs. The remaining ports of the main chamber are sealed with optical viewports.

Since the new sub-micron period magnetic lattice structure and DBC atom chip are used in the present experiment, the vacuum chamber needs to be opened and the former 1D 10 μm -period magnetic lattice structure be replaced. Ultra-high purity (UHP) N_2 gas is flushed in the chamber through the angle valve to protect the magnetic film from possible oxidation and reduce water vapour and other particles inside the chamber during this process. After careful assembling, the chamber is pumped down to UHV again through careful baking of the whole vacuum system. About 1×10^{-11} mbar level vacuum is achieved after a two-week vacuum baking at about 110 °C.

4.2 Laser system

The laser system is comprised of four lasers housed on a single optical table. It creates four different beams required for a BEC experiment, which are called the trapping light, the repumper light, the optical pumping light and the imaging light. These four laser beams with different frequencies and the energy levels of the ^{87}Rb D_2 transition are illustrated in Figure 4.2. The optical table is floated with compressed air to minimise mechanical vibrations which affect the laser locking stability. The optical table is properly covered to block any scattered light from entering the

vacuum chamber which is mounted on a separate “machine table” next to the laser system. The covering also reduces acoustic noise and improves temperature stability inside. Finally, the different beams created from the laser system are transferred to the machine table through polarisation-maintaining optical fibres.

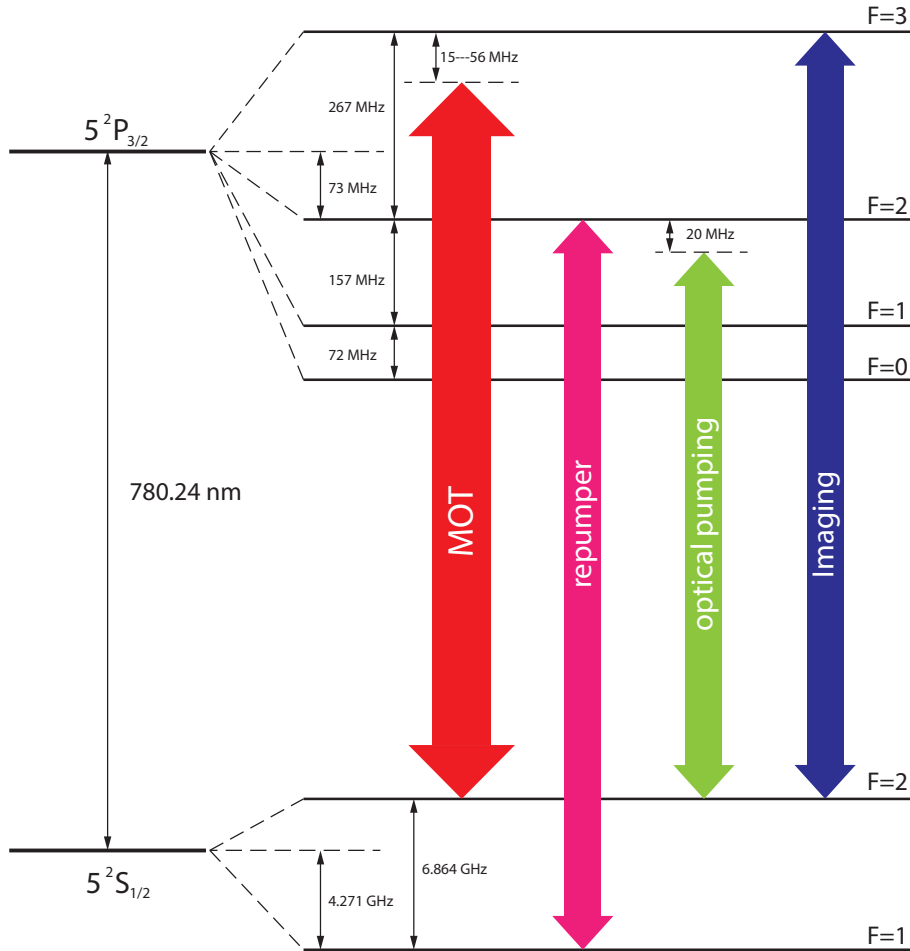


Figure 4.2: Energy level diagram of the ^{87}Rb D₂ line. Four different laser frequencies are used in the experiment.

The BEC experiment starts with the creation of a magneto-optical trap. This requires the trapping light to be red-detuned by several linewidths from resonance with the $F = 2 \rightarrow F' = 3$ cycling transition. To collect a large number of atoms, we require as much light as possible. Therefore, a tapered amplifier laser system (Topica TA100) with typically ~ 600 mW output is used as our trapping laser. A small amount of light (~ 3 mW) from the rear output of the TA100 is used for

the locking spectroscopy. The beam frequency is first blue-shifted $2f_1$ by passing AOM 1 (Isomet 1205C-2) in a double-pass configuration and locked to the ^{87}Rb $F = 2 \rightarrow F' = 3$ closed transition through a modulation-free polarisation spectroscopy system [156, 157], as shown in Fig. 4.3 (a). The main output of the TA100 is passed through AOM 2 (Isomet 1206C) whose frequency is fixed at $f_2 = 125$ MHz. The first-order diffracted beam is coupled into a polarisation-maintaining optical fibre which gives an output power ~ 200 mW. The effective detuning from the closed transition $F = 2 \rightarrow F' = 3$ is $f_2 - 2f_1$. During an experiment, the frequency of the trapping light is only varied through AOM 1, since the double-pass configuration maintains the beam position. In the MOT stage, $f_1 = 70$ MHz and the frequency of the trapping laser is red-detuned 15 MHz from the transition. In the following polarisation-gradient cooling (PGC) stage [158], this detuning is increased to 56 MHz to compress and further cool the cloud.

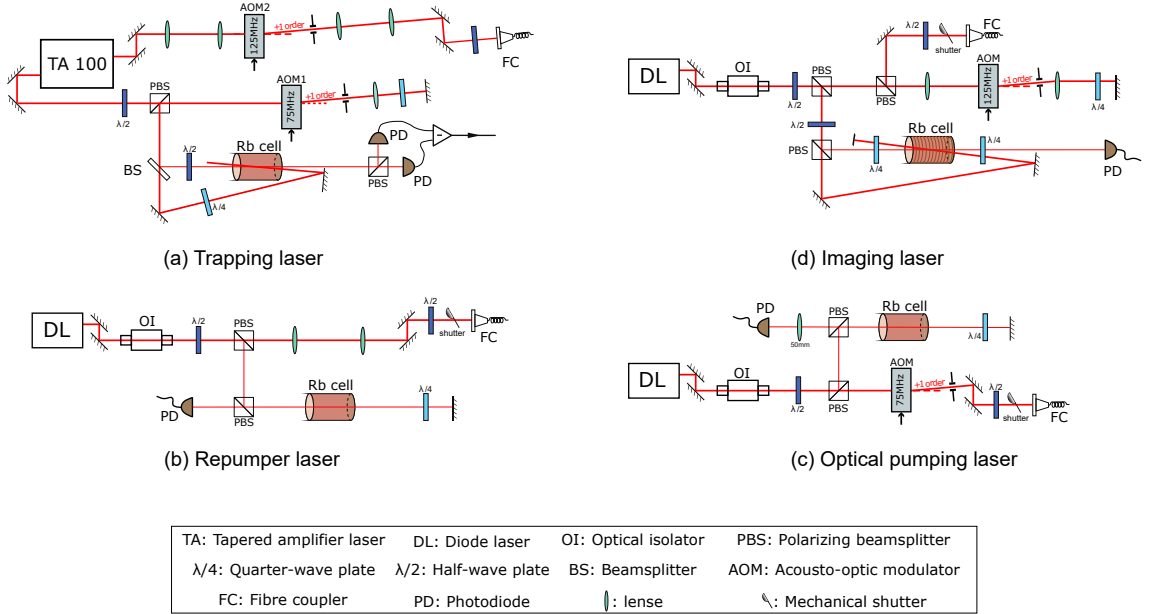


Figure 4.3: Schematic drawing of the laser system: optics for (a) the trapping laser, (b) the repumper laser, (c) the optical pumping laser and (d) the imaging laser.

In the MOT stage, the trapping beam with high intensity and mixed polarisation can introduce a high probability of off-resonant excitation of the $F = 2 \rightarrow F' = 2$ transition. The $F' = 2$ state can spontaneously decay into the lower ground-state

$F = 1$, which is a dark state. Once atoms are populated in the dark state, they are out of the cooling cycle. Therefore, a repumper laser is required to prevent all the atoms being rapidly pumped into this state and lost from the trap. A MOGLabs diode laser (ECD-004) is used for the repumper laser. It has ~ 50 mW output power. The repumper laser is locked to the $F = 1 \rightarrow F' = 2$ transition using a standard modulation locking technique [159], Fig. 4.3 (b). The repumper light is coupled to a polarisation-maintaining fibre. In order to improve the coupling efficiency, beam mode matching is done by a lens telescope. It yields ~ 20 mW at the fibre output.

In the experiment, after the polarisation-gradient cooling (PGC) stage the atoms are distributed over all ground-state magnetic sublevels. In order to create a BEC in the $|F = 1, m_F = -1\rangle$ state, the atoms are then optically pumped into this state for magnetic trapping. A MOGLabs diode laser with ~ 40 mW output is employed as an optical pumping laser. The light is locked to the $F = 2 \rightarrow F' = 1$ and $F = 2 \rightarrow F' = 3$ transition crossover with a modulation locking scheme, Fig. 4.3 (c). Before coupling into the optical fibre, the beam is passed through an AOM (Isomet 1205C-2) operating at 75 MHz. As a result, the beam is red-detuned by ~ 20 MHz from the $F = 2 \rightarrow F' = 2$ transition. The fibre output is ~ 3 mW. The required polarisation (σ^-) is achieved by passing through a $\lambda/4$ waveplate. The σ^- light pumps atoms into the $|F = 2, m_F = -2\rangle$ state. In order to transfer atoms from the $|F = 2, m_F = -2\rangle$ state to the $|F = 1, m_F = -1\rangle$ state, a small amount of π -polarisation is introduced by deliberately misaligning the optical pumping beam from the quantisation axis, Sect. 4.5.3.

Finally, to determine the properties of the atom cloud, we image the cloud and analyse the casted shadow. The imaging laser (a third MOGLabs diode laser) is locked to the $F = 2 \rightarrow F' = 1$ and $F = 2 \rightarrow F' = 3$ transition crossover, Fig. 4.3 (d). The error signal is obtained through modulating the Zeeman splitting of the Rb sample in a vapour cell. The output of the imaging laser is ~ 40 mW. A double-pass AOM (Isomet 1206C) configuration is built to tune the detuning between the laser frequency and the $F = 2 \rightarrow F' = 3$ transition. The output power from the optical fibre is ~ 5 mW.

In the laser system, AOMs are employed not only to shift laser frequencies, but also some of them serve to control the timing of the laser beams. These AOMs can be considered as fast switches, with a response time on the order of $\sim 1 \mu\text{s}$. However, the attenuation provided by the AOMs used to switch off the laser beams is usually a factor of 10^4 on a single pass. To achieve a long magnetic trap lifetime, therefore, mechanical shutters are used to block off the laser beams completely even though their response time is slow, on the order of $\sim 1 \text{ ms}$.

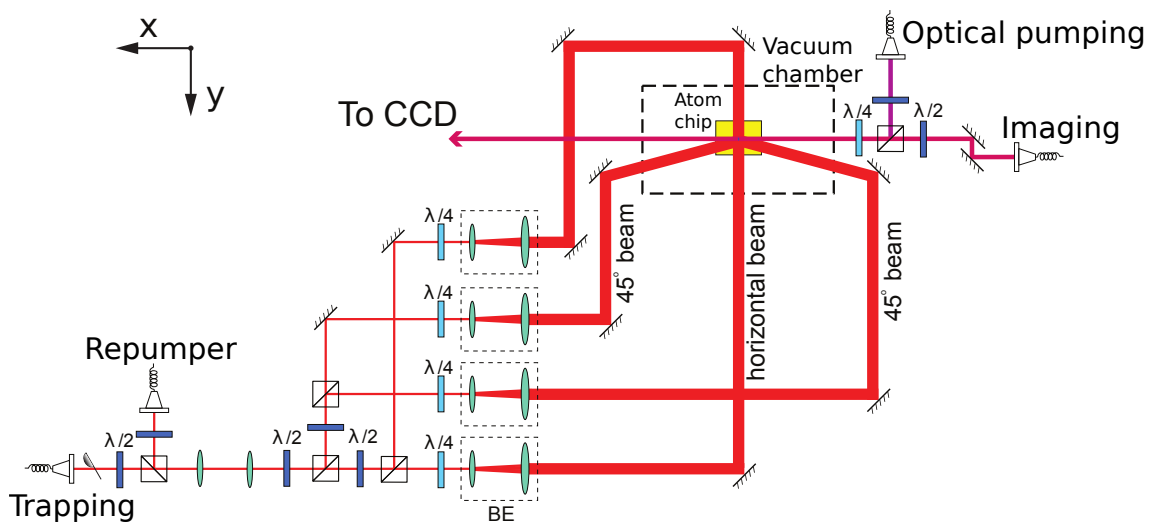


Figure 4.4: Surrounding optics on the machine table. The MOT beams including the trapping light and the repumper light are expanded (BE: beam expanding telescope) and guided into the octagonal chamber. The image and optical pumping beams pass through the chamber along the x -direction through the viewport in the six-way cross.

Polarisation-maintaining fibres bring different light beams to the machine table on which the vacuum chamber is mounted. At the same time, polarisation-maintaining fibres work as a spatial filter to provide a clean Gaussian mode. The spatial mode quality is crucial for the imaging beam. On this table, the trapping and repumper beams are combined using a polarisation beam splitter and sent to the UHV chamber after division into four different beams and expansion to a diameter of $\sim 20 \text{ mm}$, as shown in Fig. 4.4. The power in each beam is around 40 mW . The optical pumping and imaging beams are also combined using the same method. The imaging beam is σ^+ polarised by carefully aligning with a $\lambda/4$ waveplate. Meanwhile, the optical

pumping beam is automatically σ^- polarized.

4.3 Absorption imaging

All of the information about the atom clouds prepared in our experiments is obtained by absorption imaging [120]. With this technique, the shadow cast by the atoms in a beam of resonant laser light is imaged onto a CCD camera. Following Lambert-Beer's law one can write the intensity distribution $I(y, z)$ of the probe light (imaging direction: x -direction) after passing through the cloud as

$$I(y, z) = I_0(y, z)e^{-OD(y, z)}, \quad (4.1)$$

where $I_0(y, z)$ is the intensity distribution of the probe beam before the absorption. The optical density

$$OD(y, z) = \sigma \int n(x, y, z) dx \quad (4.2)$$

is given by the photon absorption cross section σ and the cloud density $n(x, y, z)$. When imaging untrapped clouds, a small magnetic field is applied to give a well-defined quantisation axis, since the imaging light is σ^+ polarised with respect to this quantisation axis. The probe beam forms a closed cycle between the $|F = 2, m_F = +2\rangle$ and the $|F = 3, m_F = +3\rangle$ states. The absorption cross section can be written as

$$\sigma = \frac{\sigma_0}{1 + I/I_s + 4(\delta/\Gamma)^2}, \quad (4.3)$$

where $\sigma_0 = \frac{3\lambda^2}{2\pi}$ is the resonant absorption cross section; for ^{87}Rb D₂ line, $\sigma_0 = 2.9 \times 10^{-13} \text{ m}^2$. I_s is the saturation intensity, δ is the laser detuning and Γ is the natural radiative linewidth. The largest absorption signal is obtained by imaging on resonance, $\delta = 0$. We usually choose $I \ll I_s$ so that $\sigma \approx \sigma_0$ is a constant. The atomic column density can be determined as

$$n(y, z) \equiv \int n(x, y, z) dx \approx \frac{OD(y, z)}{\sigma_0}. \quad (4.4)$$

The intensity distribution of the light in the plane of the atoms is imaged onto a CCD camera. In each experimental cycle, the camera takes three pictures, one clean

image which discharges all the dark counts, one absorption image (I_{abs}) with atoms and one reference (I_{ref}) image without atoms. Taking the last two pictures allows one to compensate for inhomogeneities in the intensity distribution of the imaging beam [120]. Then the optical density is determined as

$$OD = -\ln[I/I_0] = -\ln[I_{abs}/I_{ref}]. \quad (4.5)$$

From the optical density, the total number of atoms located in an area A in the plane of the atoms is calculated by summing over the pixels (i, j) corresponding to that area

$$N = \int_A n(y, z) dy dz = \frac{A}{\sigma_0} \sum_{(i,j) \in A} OD_{ij}. \quad (4.6)$$

4.3.1 CCD camera

The camera used in the experiment is a frame transfer camera (MicroMAX: 1024B) from Princeton Instruments. The CCD chip consists of two equal sized pixel arrays, one array (1024×1024 pixels²) is sensitive to the external light, the other is masked (not exposed to light) and used as a store array. The area of each pixel is $A_0 = 13 \mu\text{m} \times 13 \mu\text{m}$. The quantum efficiency of the camera chip is $Q \approx 0.7$ at $\lambda = 780$ nm. This value describes the average number of electrons produced in the CCD chip by one photon. When the CCD camera takes an image, the imaging light is pulsed onto the CCD chip. Assuming I is the imaging light intensity and τ is the pulse duration, the number of photons in the imaging pulse shining on one pixel can be determined from $IA_0\tau/(h\nu)$, where ν is the light frequency. The number of produced electrons on that pixel is $QIA_0\tau/(h\nu)$. The measured digitised values I_{abs} and I_{ref} are proportional to the produced electron numbers on the CCD chip.

4.3.2 Imaging optical setup

The laser beam used for detection is spatially filtered by an optical single mode fibre. After collimation, the very uniform imaging beam is guided into the UHV chamber which contains the atomic cloud. The collecting optics are shown in Fig. 4.5 (a),

the image is formed by two high-quality lenses, a near-infrared achromatic doublet (ThorLabs) with focal lengths $f_1 = 120$ mm and $f_2 = 500$ mm. They are arranged in the following way: the first lens is placed at a distance f_1 from the object and the CCD sensor is at a distance f_2 from the second lens. The distance between the two lenses is not important. The magnification M obtained is $M = f_2/f_1$. In the experiment, the magnification is checked by measuring the effective pixel size. The measurement is made by recording the position of the cloud centre at different free-falling times t . The position of the free falling cloud can be determined from the kinematic equation:

$$z = \frac{g}{2}t^2 + v_0t + z_0 \quad (4.7)$$

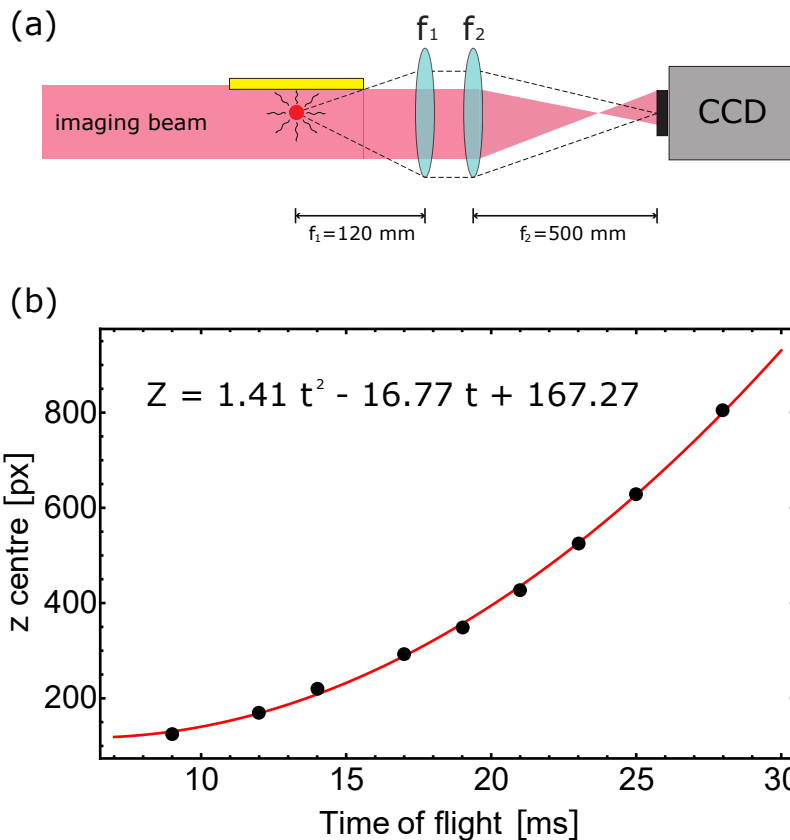


Figure 4.5: (a) Two-lens setup for absorption imaging. (b) Time-of-flight measurement of the effective camera pixel size in the objective plane. The experimental points (black circles) are fitted by a second-order polynomial function (red solid curve).

Fitting of the experimental points, as shown in Fig. 4.5 (b), with a second-order polynomial function gives the coefficient C in units of $[\text{pixel}\cdot\text{s}^{-2}]$ in front of t^2 . Therefore, the effective pixel size in the object plane is $g/(2C) = 3.48 \mu\text{m}$. This measured value agrees with the calculated value $3.12 \mu\text{m}$. The resolution of the imaging system for this experiment is about $10 \mu\text{m}$.

The imaging beam is usually oriented parallel to the chip surface. To image atoms at a small atom-surface distance, Sect. 5.1.1, the beam can be tilted by a few degrees towards the surface, so that both the direct and mirror images in the reflecting chip surface are visible [160].

The predominant source of noise in absorption imaging set-ups is interference fringes in the imaging beam, caused by diffraction from the chip surface, from dirt on the optics, and by reflections from the various optical surfaces in the beam path. If there are mechanical vibrations present, these fringes cannot be cancelled out completely by the method discussed above. To minimise mechanical vibrations, all the elements along the imaging line must be bolted tightly. The time delay between the absorption image and the reference image should be reduced as much as possible. For this reason, the frame transfer mode is activated for the CCD camera, so that the delay can be reduced to a few ms [155].

4.4 Experimental control and 50 Hz line trigger

The whole experiment is controlled by many synchronised trigger signals. These signals can be divided into two categories, the digital signals (the signals that control the shutters and AOMs on and off, and other trigger signals) and the analog signals (the signals that control the current ramping in the atom chip wires and in the magnetic field coils, and also the signals that drive the frequencies of AOMs). All of these control signals are created by three National Instruments (NI) cards housed in one personal computer: one PCI-6259 with 32 digital output channels and two PCI-6713 cards with a total of 16 analog output channels. The output signals from these cards are synchronised by linking the cards with a RTSI cable. The cards

are programmed under a Labview environment. To run the experiment, the whole programmed sequence is first loaded into the buffer of the computer. Then the computer executes the program based on the defined step size. The size of the data of the programmed sequences is inversely proportional to the step size. Different stages of the BEC experiment actually have different tolerances on the step size. For instance, the initial MOT stage has quite a rough requirement whereas the imaging stage requires a very precise short pulse. Therefore, to improve the efficiency of the program we divide it into two arrays: the first array contains the MOT loading stages which has a large step size, 10 ms, while the rest of the program forms the second array which has a small step size, 100 μ s. A step size of 100 μ s is usually sufficient in the experiment. In addition, a second computer is used to control the image acquisition of the CCD camera.

4.4.1 Control electronics

The current in the magnetic field coils and chip wires is controlled by home-made IGBT switches [153]. These switches typically have a switching time $\sim 800 \mu$ s for the U-wire and Z-wire current and a switching time ~ 10 ms for the magnetic field coils. To create traps, external coils are mounted surrounding the vacuum chamber. A pair of coils in an anti-Helmholtz configuration used to produce a quadruple field for the mirror MOT is mounted at 45° to the chip surface (Fig. 2.5 (b)). The separation of the two coils is about 250 mm. It produces a quadruple field of gradient about 15 G/cm when passing 10 A current. A large bias field along the x -direction B_x is produced by an external pair of coils. Each coil was produced by winding 104 turns of copper wire of diameter 2 mm on a plastic former of radius 175 mm. The coils can produce about 50 G magnetic field at 10 A. Three other independent small coils of relatively low inductance are positioned in an orthogonal geometry around the vacuum chamber to cancel stray magnetic fields and to produce additional field components.

4.4.2 50 Hz AC line synchronisation

Time-varying magnetic fields are normally present in the lab. These fields are predominantly 50 Hz and harmonic frequencies which originate from lab equipment power supplies. Various measures can be employed to minimise these fields such as placing the power supplies far away from the scientific chamber and adding cancellation coils to create an opposing AC field. On the other hand, instead of actually cancelling these magnetic fields, a simpler solution is to ensure the experiment performs magnetically sensitive steps at well-defined phases of the AC line. We can synchronise the experiment to a zero-crossing of the AC power line using a circuit designed by the Rice group [161], Fig. 4.6.

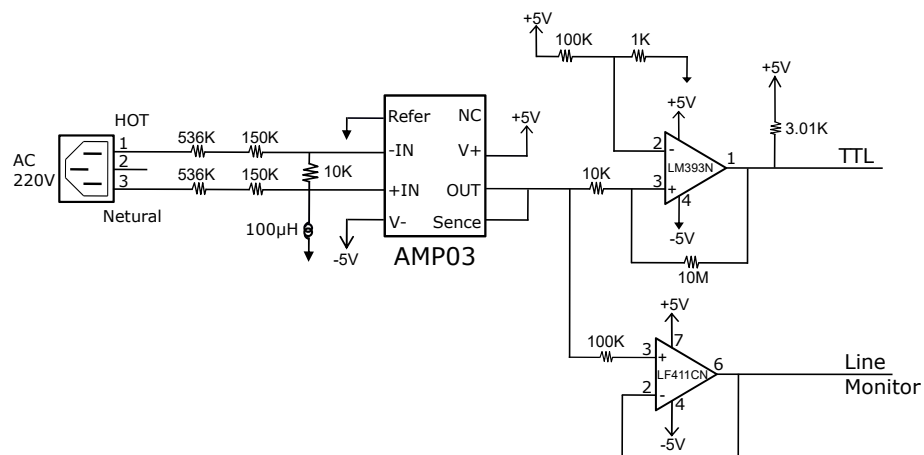


Figure 4.6: Schematic of the AC line synchronisation circuit.

The circuit continuously converts the AC line signal to a TTL signal, which is fed to one of our NI cards. Our Labview program allows the experiment sequence to wait for the TTL trigger at the desired position. The following sequence is only executed once the trigger has arrived. In this way, the desired experiment can be locked to a fixed phase of the AC line. This locking suppresses the noise of the measurements which are sensitive to the magnetic environment. One example is RF spectroscopy measurements which are discussed in Sect. 4.5.6.

4.5 Experimental sequence for BEC

4.5.1 Mirror MOT

The experimental cycle begins with loading a mirror MOT (MMOT) [29]. The Rb dispensers are switched on in a pulsed mode to make an efficient loading of the MMOT and to maintain a high vacuum level (to prevent reduction of the lifetime of the atoms in the magnetic trap). The dispenser is switched on with 5.8 A for 26 s at the beginning of the experimental cycle. In the last phase of the cycle, the dispenser is switched on again with 2.9 A. This current is below the threshold for releasing Rb atoms, but keeps the dispenser warm so that it can heat up more quickly when pulsed in the next cycle. The total experiment cycle time lasts for 65 s.

The position of the MMOT centre can be displaced slightly by adding a uniform bias field to the quadrupole field. Good performance of the MMOT is achieved when the centre is located 1-2 mm from the surface [29]. The MOT beams consist of combined trapping beams whose frequency is red-detuned 15 MHz ($\sim 2 \Gamma$) and repumper beams. We typically collect 2×10^8 atoms in the MMOT located ~ 1.2 mm below the chip surface in the first 26 s, and the typical atom temperature is $\sim 100 \mu\text{K}$.

4.5.2 Compressed U-wire MMOT

After loading the MMOT, the trapped atoms need to be brought closer to the chip surface and finally transferred to the magnetic trap created by the chip wire (Z-wire trap). In order to achieve good initial conditions for evaporative cooling in a magnetic trap, several intermediate steps are required.

The MMOT is first transferred to a compressed U-wire MMOT (CMOT) by ramping down the current in the external quadrupole coils with the simultaneous creation of a quadrupole trap on the atom chip by ramping up the current through the U-wire and the field in the bias magnetic coils B_x . This transfer is done within 30 ms to avoid significant atom losses. The strong confining force in the CMOT allows the atoms to be kept tightly trapped as they are raised towards the surface.

Typically, we transfer $\sim 1.5 \times 10^8$ atoms to the CMOT. The positioning of the CMOT closer to the surface is crucial for aligning the cloud with the centre of the Z-wire trap. Meanwhile, the CMOT geometry, in which the radial field gradient is much higher than the axial field gradient, helps to change the cloud shape from roughly spherical in the MMOT to ellipsoidal. This also helps to match the cloud shape to the shape of the Z-wire magnetic trap. However, the increased density of the cloud results in an increase in the temperature to $\sim 140 \mu\text{K}$. Eventually, the compression of the cloud is limited by the radiation pressure. Thus the phase space density of the cloud is limited.

In order to increase the phase space density, the frequency of the trapping light is further red-detuned to 56 MHz ($\sim 9 \Gamma$) during the compression. This decreases the scattering rate and leads to a reduction of the radiation pressure which finally helps to increase the cloud density. A small fraction of atoms in the centre (zero magnetic field) of this configuration are cooled by polarisation gradient cooling. To increase this effective volume we rapidly reduce the magnetic field gradient to 0.11 T/m ($I_U = 2.8 \text{ A}$, $B_x = 2.5 \text{ G}$) in 5 ms while ensuring the centre of the quadrupole field does not shift. This procedure reduces the cloud temperature from $140 \mu\text{K}$ down to $40 \mu\text{K}$. After this, the CMOT light is shut off and the U-wire current is switched to zero, leaving the atoms in a uniform magnetic field of $B_x = 2.5 \text{ G}$.

4.5.3 Optical pumping

After polarisation gradient cooling, the atoms are distributed across the m_F states of the ground states. When atoms are transferred to the Z-wire magnetic trap, only low field-seeking states can be trapped. To magnetically trap as many atoms as possible, the atoms are pumped into the $|F = 1, m_F = -1\rangle$ state in an optical pumping stage. This state is chosen because it has a three-times smaller three-body recombination coefficient [113, 114] and two-times weaker magnetic confinement than the $|F = 2, m_F = +2\rangle$ state. A schematic of the optical pumping is shown in Fig. 4.7.

The optical pumping light is red-detuned 20 MHz from the $F = 2 \rightarrow F' = 2$

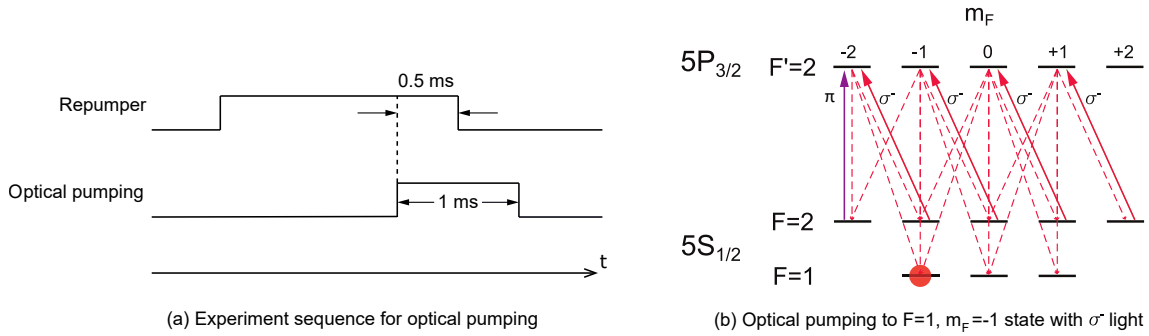


Figure 4.7: Optical pumping to the $|F = 1, m_F = -1\rangle$ trapping state. The red dashed lines denote spontaneous emission.

transition since the cloud is optically thick for resonant light. The atoms can be optically pumped into the $|F = 1, m_F = -1\rangle$ state with σ^- light. The optical pumping stage is performed by applying 1 ms-long σ^- -polarised light. Repumper light is also required since it brings atoms in the $|F = 1, m_F = +1\rangle$ state and the $|F = 1, m_F = 0\rangle$ state into the optical pumping cycle. It can be provided from the MOT repumper light by carefully designing the experiment sequence so that there is a 0.5 ms overlap between the repumper and the optical pumping light, as shown in Fig. 4.7 (a). In addition, a small amount of π -polarisation component is added to the optical pumping beam by deliberate misalignment with the quantisation axis. When the repumper light is switched off 0.5 ms before the optical pumping light, most of the population in the $|F = 2, m_F = -2\rangle$ state is transferred to the $|F = 1, m_F = -1\rangle$ state due to the π transition via the $|F' = 2, m_F = -2\rangle$ excited state.

The efficiency of the optical pumping is checked by comparing the atom number captured in the magnetic trap with and without the optical pumping pulse applied. An optimised optical pumping stage normally gives a factor of 2.5 improvement. After the optical pumping pulse has finished, both the optical pumping and repumper shutters are closed, leaving the atoms in the dark and captured by the magnetic trap.

4.5.4 Z-wire magnetic trap

In order to maximise the capture efficiency in the Z-wire magnetic trap, the mode-matching needs to be carefully optimised. The following requirements are considered. First, a proper trapping frequency in the Z-wire trap is necessary to prevent a breathing mode excitation. Second, the trap and the cloud should be properly overlapped, otherwise the atom cloud will slosh around in the magnetic trap. Both situations will heat the cloud. The proper trapping frequency ω_i in each direction can be determined by measuring the size σ_i and temperature T of the cloud after optical pumping, $\omega_i = \frac{1}{\sigma_i} \sqrt{\frac{k_B T}{m}}$ ¹. The third consideration is the trap depth. To keep as many of the atoms as possible, the trap must be as deep as possible. In practice, all of these optimising parameters are fundamentally constrained by the atom chip itself, which is the maximum current density that the chip wires can safely carry.

In the experiment, the initial Z-wire magnetic trap is formed by passing 35 A current through the Z-wire and increasing the B_x bias field to 33 G. The trap bottom is adjusted to ~ 3 G by applying a bias field $B_y = 7$ G to prevent spin-flip loss and to enlarge the trap depth. The magnetic field gradient is about 150 G/cm in the vertical z -direction for this initial Z-wire trap. Approximately 5×10^7 atoms are transferred to the initial magnetic trap at a temperature of $\sim 80 \mu\text{K}$. The transfer efficiency is mainly limited by the small volume and finite depth of the Z-wire magnetic trap. The initial magnetic trap lasts for 5 ms, then the trap is compressed in the next 100 ms by ramping up the Z-wire current I_z , the bias fields B_x and B_y to 37.6 A, 52 G and 8.3 G, respectively. The magnetic field gradient correspondingly increases to about 380 G/cm in the vertical z -direction. Since the magnetic trap is conservative the optimum compression is adiabatic, i.e., the phase space density of the initial magnetic trap is preserved. The adiabatically compressed magnetic trap brings the cloud closer to the surface, increases the trap depth and most importantly boosts the

¹Since the mean potential energy in the trap in each direction should match the thermal energy in this direction, $\frac{1}{2}m\omega_i^2\sigma_i^2 = \frac{1}{2}k_B T$.

elastic collision rate ² so that the runaway condition can be fulfilled, and effective evaporative cooling is possible.

At the end of the compression phase, the Z-wire trap is located below $670 \mu\text{m}$ above the chip surface. The trap frequency in the radial direction can be measured by the dipole-oscillation method: shifting the position of the trap centre then returning back to the initial position after half of an oscillation period, and measuring the induced oscillation frequency of the centre of the cloud. The position shift must be a small displacement to ensure the cloud remains in the harmonic region of the potential.

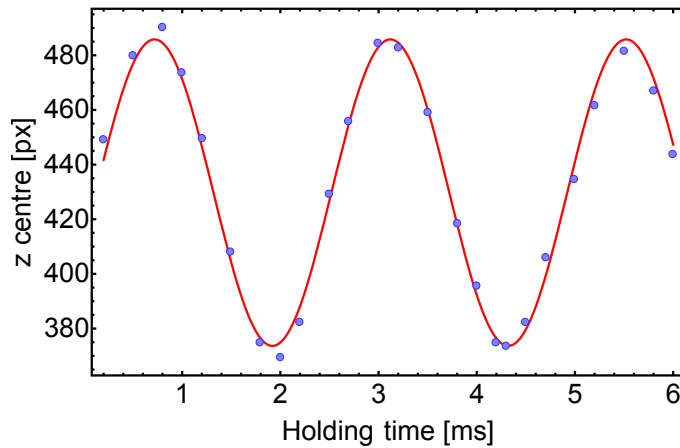


Figure 4.8: Experimental measurement of the radial trapping frequency of the Z-wire magnetic trap via dipole oscillations. The measured radial trapping frequency $\omega_r/2\pi = 416 \pm 2 \text{ Hz}$.

Figure 4.8 shows the radial trapping frequency measurement of the Z-wire trap for $I_z = 37.6 \text{ A}$, $B_x = 52 \text{ G}$, $B_y = 8.3 \text{ G}$. The trapped cloud is first cooled using RF evaporation to reduce its size and the temperature. The cloud is then kicked by decreasing the current in the wire for half of an oscillation period ($\sim 1 \text{ ms}$) and then returning it to the initial value. During this process all the bias fields are kept constant. The final centre positions of the cloud are recorded with time-of-flight

² $1/\tau_{el} = \sqrt{2\bar{n}}\sigma_{el}\bar{v}$; adiabatic compression increases both the average cloud density \bar{n} and the mean relative thermal velocity $\sqrt{2\bar{v}}$.

measurements after different holding times t . The position of the cloud centre is measured using Gaussian fits to the radial profile. The measured points are fitted with a simple sine curve. This gives an oscillation frequency of $\omega_r/2\pi = 416 \pm 2$ Hz. The measured value agrees well with the expected trap frequency ($\omega_r/2\pi = 426$ Hz) determined from the magnetic field calculation.

In our chip configuration, it is difficult to introduce a dipole-oscillation in the axial direction. Therefore, a collective mode excitation method [162] is used to measure the axial trapping frequency. In this method, the trapped cloud is first evaporatively cooled to a temperature $T/T_c \approx 2$. The density of the thermal cloud and the corresponding interactions are very small. The cloud is then perturbed by switching off the bias field B_y for a certain time, keeping $I_z = 37.6$ A and $B_x = 52$ G constant at the same time. As a result of this operation the trap confinement suddenly changes in both the radial and the axial directions. The thermal cloud starts evolving according to this perturbation. For a harmonically confined thermal gas, the lowest normal mode in the excitation spectrum is the dipole oscillation $\hbar\omega$. Due to parity constraints, only the second lowest mode $2\hbar\omega$ can be excited. Finally, the trap is switched off and the cloud response is monitored through time-of-flight measurements. The observable in this case is the width of the expanding cloud as a function of the holding time. The measurements are shown in Fig. 4.9. The quality of the data is limited by the single measurement and the perturbation also introduces a small dipole oscillation. The quality of the data can be improved by simply taking the average value of multiple measurements. A carefully designed perturbation which only introduces the second lowest excitation can also improve the quality of the measurement.

By fitting the measured data to a simple sine curve, the extracted collective mode excitation frequency is 36 ± 2 Hz. Therefore, this frequency should be twice the axial trapping frequency, $\omega_{ax}/2\pi = 18 \pm 2$ Hz. The calculated axial trapping frequency is 18 Hz, which is very close to the measured value. Therefore, the sinusoidal fitting is appropriate. For comparison, we also study the BEC case. The same measurement is performed on a trapped condensate. We expect to see the excitation frequency

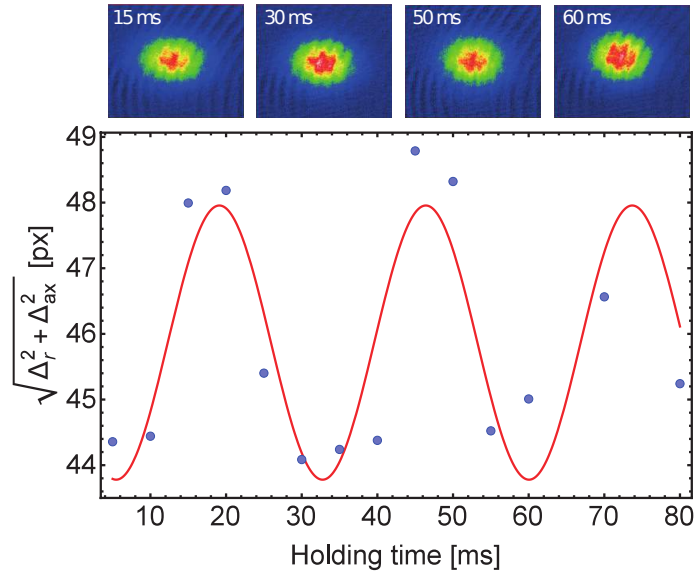


Figure 4.9: Measurement of the axial trapping frequency of the Z-wire trap via collective mode excitation of a thermal cloud. The spatial profile of the cloud starts to evolve under a certain perturbation.

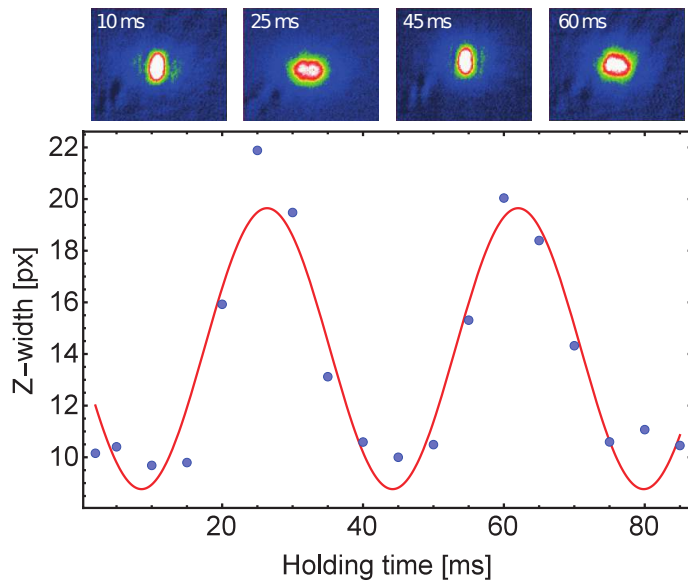


Figure 4.10: Collective mode excitation of a condensate. The evolution of the condensate shows a radial width oscillation.

deviate from that of the spectrum of a thermal cloud as a result of the strong interaction in the condensate. The measured result is shown in Fig. 4.10. The frequency of the excitation is determined from a sine wave fit to the freely oscillating cloud

width. The measured collective mode excitation frequency is $\omega_c/2\pi = 28 \pm 1$ Hz. For a cigar-shaped trap geometry ($\omega_{ax}/\omega_r \ll 1$), this corresponds to a quadrupole mode ($\ell = 2, m = 0$) excitation, $\omega_c = \sqrt{5/2}\omega_{ax}$ [163]. From this formula, the derived axial trapping frequency is $\omega_{ax}/2\pi = 17.7 \pm 1.0$ Hz, which also agrees with our previous thermal cloud excitation measurement.

After adiabatic compression, the trap frequency increases on the one hand. On the other hand, the temperature of the cloud also increases. By monitoring the cloud expansion, we estimate the cloud temperature to be around $200 \mu\text{K}$. Therefore, the calculated elastic collision rate $1/\tau_{el} \approx 150 \text{ s}^{-1}$. The trap loss rate $1/\tau_{loss}$ can be monitored from a trap lifetime measurement, which is performed by measuring the atom number in the trap for different holding times. In Fig. 4.11, we can see there is possible evidence of double-exponential decay, the fast atom decay at short times is probably due to the finite trap depth. The lifetime of the trap is determined mainly by the slow decay tails at long times. A lifetime of ~ 20 s is extracted from the fitting. Using the initial lifetime $\tau_{loss} = 4$ s, the value for $R = \tau_{loss}/\tau_{el}$ is therefore ~ 600 , which is within the regime where runaway evaporation can be achieved (Fig. 2.6).

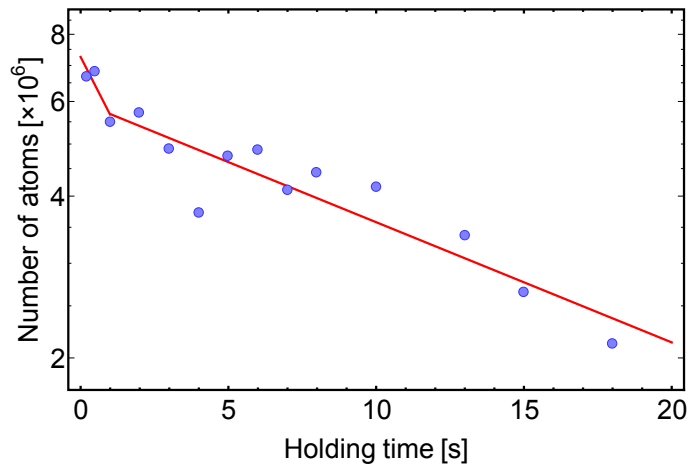


Figure 4.11: Log scale plot of the remaining $|F = 1, m_F = -1\rangle$ state atom number in the Z-wire trap versus different holding times. The blue points are the experimental data. The red solid line is a fit to an exponential decay function with lifetimes of 4 s and 19.4 s at short and long times, respectively.

4.5.5 Bose-Einstein condensate in the Z-wire trap

Once the runaway evaporation condition is achieved, it is time to apply forced RF evaporative cooling to the compressed atom cloud. A RF field is coupled to the atoms through the wire (see Fig. 3.12 (a), pins 2 and 3 or 10 and 11) positioned on the chip close to the Z-wire trap. The RF field is generated by an unamplified 30 MHz synthesised function generator (Stanford Research Systems DS345). The produced RF magnetic field is oriented in the plane perpendicular to the trap axis to drive $\Delta m_F = \pm 1$ transitions.

The RF function generator is used in sweep mode. The output frequency logarithmically ramps from a specified start frequency ν_i down to an end frequency ν_f in a certain duration when it is triggered. The amplitude of the RF signal is set to be 5 V peak-to-peak. This corresponds to a Rabi frequency $\Omega_0/2\pi = 6$ kHz, Sect. 4.5.6. In the experiment, we sweep from $\nu_i = 30$ MHz to various ν_f over a period of 12 s. Parameters of the Z-wire trap ($I_z = 37.6$ A, $B_x = 52$ G, $B_y = 8.3$ G) are kept constant during the evaporation. The atom number and the temperature of the cloud are measured by time of flight measurements at different end RF frequencies. When the RF ramp is optimised the cloud becomes more and more cold and dense by reducing the end RF frequency. The temperature and atom number dependence on the end RF frequency is shown in Fig. 4.12 (a).

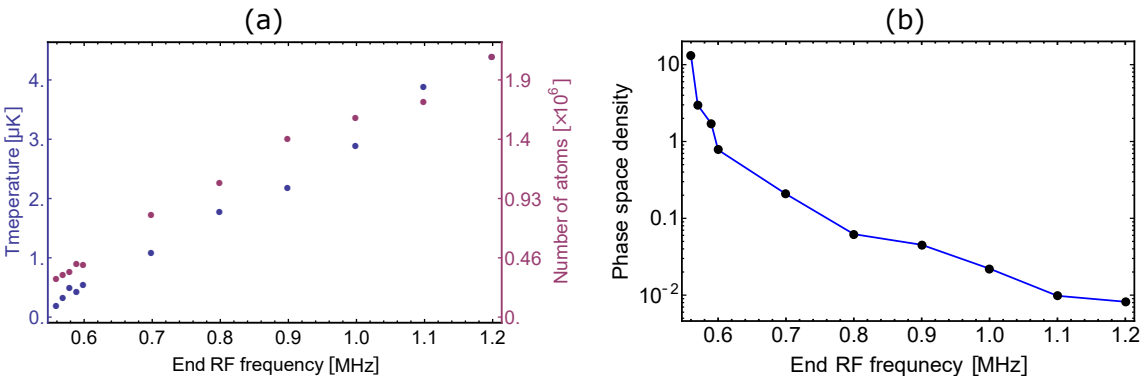


Figure 4.12: (a) Dependence of atom number and temperature in the Z-trap on the end RF frequency. (b) Log scale plot of the corresponding phase space densities versus different end RF frequencies.

To show the phase transition more clearly, the corresponding phase space densities are plotted on a log scale, Fig. 4.12 (b). A phase space density $\Phi = 1.7$ is observed at the end RF frequency $\nu_f = 590$ kHz which is larger than the critical value $\Phi_c = 1.202$ for a BEC in a harmonic trap. If the end RF frequency is further reduced to $\nu_f = 560$ kHz, then the phase space density $\Phi = 13.2$ is achieved.

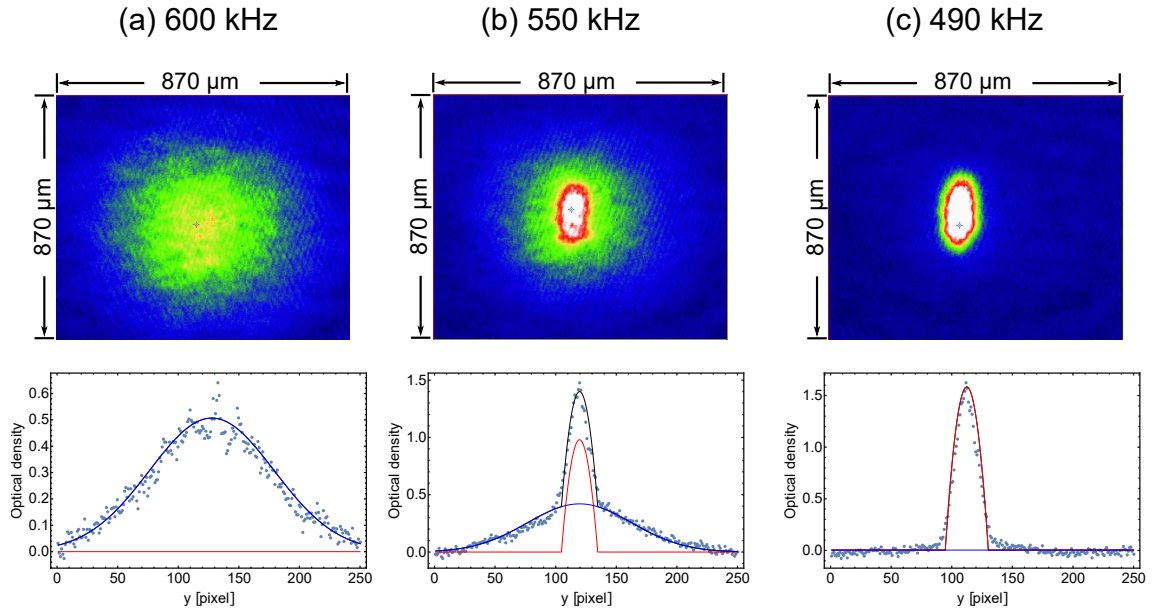


Figure 4.13: A bimodal density profile appears in the Z-wire trap as the RF end-frequency sweeps across the threshold of the BEC transition. The upper panel show the absorption images of the cloud and the bottom panel show the fits of the cloud density distribution across the peak in the y -direction. (a) Slightly above the transition, the density profile is still a Gaussian. (b) When the temperature drops below the critical temperature, a sharp parabolic peak of the condensate emerges on top of the Gaussian profile. (c) Almost a pure condensate appears as we further cool the cloud.

Other evidence of a BEC is the bimodal distribution. The density distributions of a thermal cloud and a pure BEC in a harmonic trap are clearly different. The thermal cloud has a Gaussian distribution, while the ground state of a condensate is shown to have a parabolic Thomas-Fermi distribution (Sect. 2.6.1) characteristic of the harmonic trap. The bimodal density distribution considers the partially condensed cloud as two non-interacting parts: a thermal component plus a condensate

component:

$$n(r) = (1 - f_c)n_{th}(r) + f_cn_{TF}(r) \quad (4.8)$$

where f_c is the condensate fraction. Figure 4.13 shows the emergence of a BEC as the end RF frequency is reduced. At high temperature, the density profile is an isotropic Gaussian distribution. A bimodal distribution appears as the temperature drops below the critical temperature $T_c \approx 520$ nK. After further cooling the cloud, we can produce an almost pure BEC.

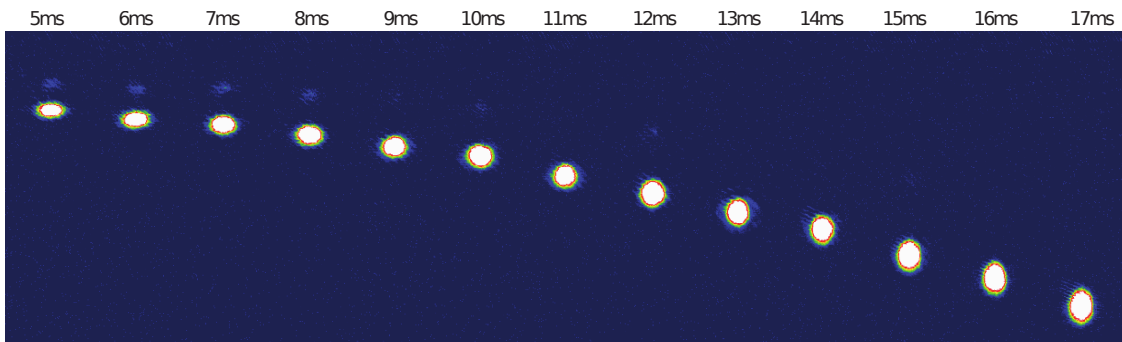


Figure 4.14: Anisotropic expansion of a condensate after the indicated times of flight. The small “shadow” clouds above the BEC are attributed to small thermal clouds spilling over the magnetic trap during the evaporation.

The easiest way to observe a signature of a BEC is the anisotropic expansion after releasing the cloud from the trap due to the anisotropic confinement. Once released, the condensate undergoes a radial accelerated expansion as the atom-atom interaction energy is converted to kinetic energy. This is because $\omega_{rad}/\omega_{ax} \approx 23 \gg 1$ and $\omega_{rad}t > 1$ when the expansion time t is longer than 1 ms. The asymptotic expansion parameters upon release from the trap can be approximated by [164]

$$R(t)_{rad}/R(0)_{rad} = 1 + \omega_{rad}t \quad (4.9)$$

$$R(t)_{ax}/R(0)_{ax} = 1 + \frac{\pi\omega_{ax}^2}{2\omega_{rad}}t. \quad (4.10)$$

The radial width $R(t)_{rad}$ of the cloud expands rapidly while the expansion of the axial width $R(t)_{ax}$ is negligible after release from the trap. The anisotropic expansion is shown in Fig. 4.14. The absorption image integrates the atom distribution over

one of the transverse directions, and in fact the shape of the cloud after expansion is a pancake shape instead of a cigar shape.

4.5.6 RF spectroscopy

In addition to a time of flight measurement, RF spectroscopy is a powerful *in-situ* technique to characterise an atomic cloud in a magnetic trap. The trapped atoms are probed by applying a RF pulse for a certain duration. Atoms satisfying the resonance condition $hf = \mu_B m_F g_F B(x, y, z)$ are outcoupled from the trap, where f is the frequency of the RF pulse. The remaining atoms are measured by absorption imaging. A self-consistent Hartree-Fock mean-field model was used to fit the attained RF spectra (Appendix 1 in [155]). Figure 4.15 shows a RF spectrum of a Z-wire BEC obtained by applying a 3 ms RF pulse of amplitude 0.5 V. A very narrow inverted-near parabolic peak appears when the end-RF frequency is close to the trap bottom, which indicates an almost pure BEC. The temperature of the condensate can be extracted from the fit; in this case it is about 300 nK. Each black dot represents a measured atom number at one frequency of the RF pulse in one experiment cycle. By repeating experiment cycles, we can scan across the RF resonance peak.

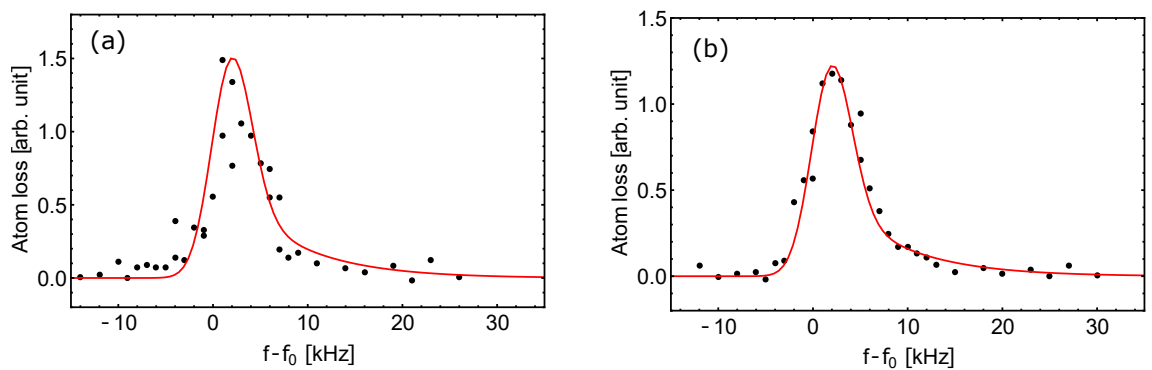


Figure 4.15: RF spectrum of a BEC in the Z-wire magnetic trap. A RF pulse of amplitude 0.5 V is applied for 3 ms (a) without a 50 Hz AC line trigger (b) with a 50 Hz AC line trigger. Trap bottom $f_0 = 657$ kHz.

The RF spectrum is quite sensitive to any magnetic noise. During each experi-

ment cycle when we are applying a RF pulse, the phase of the 50 Hz AC line at that moment fluctuates. This fluctuation alters the trap bottom, broadening the measured spectrum. With the help of the 50 Hz AC line synchronisation (Sect. 4.4.2), the influence of the magnetic noise can be suppressed and the measured RF spectrum shows a more stable result and a more defined shape, Fig. 4.15 (b).

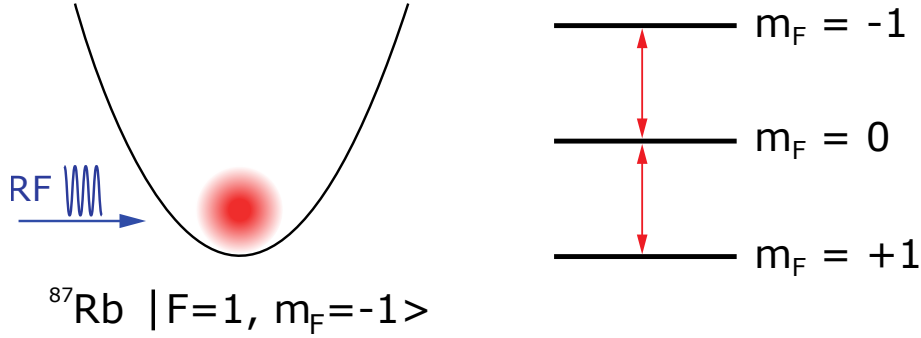


Figure 4.16: Schematic diagram of RF radiation-induced coupling between three Zeeman sublevels of the $F = 1$ state.

Since RF spectroscopy is the major method we use to probe the atomic cloud in a magnetic lattice, it is necessary to characterise the coupling of atoms introduced by the RF radiation. The coupling strength can be described by $\Omega_0 = \frac{\mu_B g_F B}{2\hbar}$. As the RF magnetic field is perpendicular to the quantisation axis, all of the RF power is equally distributed to drive σ^+ and σ^- transitions. We follow the theoretical treatment described in [165]. Atoms condensed in the $|F = 1, m_F = -1\rangle$ state are coupled by RF radiation leading to Rabi-type oscillations in a three-level system, as shown in Figure 4.16. The relative populations N_i/N of all the Zeeman sublevels in the $F = 1$ state, $i = -1, 0, +1$, are given by:

$$\begin{aligned} N_{-1}/N &= |\psi_{-1}|^2 = (1 - |c_2|^2)^2 \\ N_0/N &= |\psi_0|^2 = 2|c_2|^2 (1 - |c_2|^2)^2 \\ N_{+1}/N &= |\psi_{+1}|^2 = |c_2|^4, \end{aligned} \quad (4.11)$$

where c_2 is:

$$|c_2|^2 = \frac{\Omega_0^2}{\Omega_0^2 + \Delta^2} \sin^2 \left(\frac{\sqrt{\Omega_0^2 + \Delta^2}}{2} t \right). \quad (4.12)$$

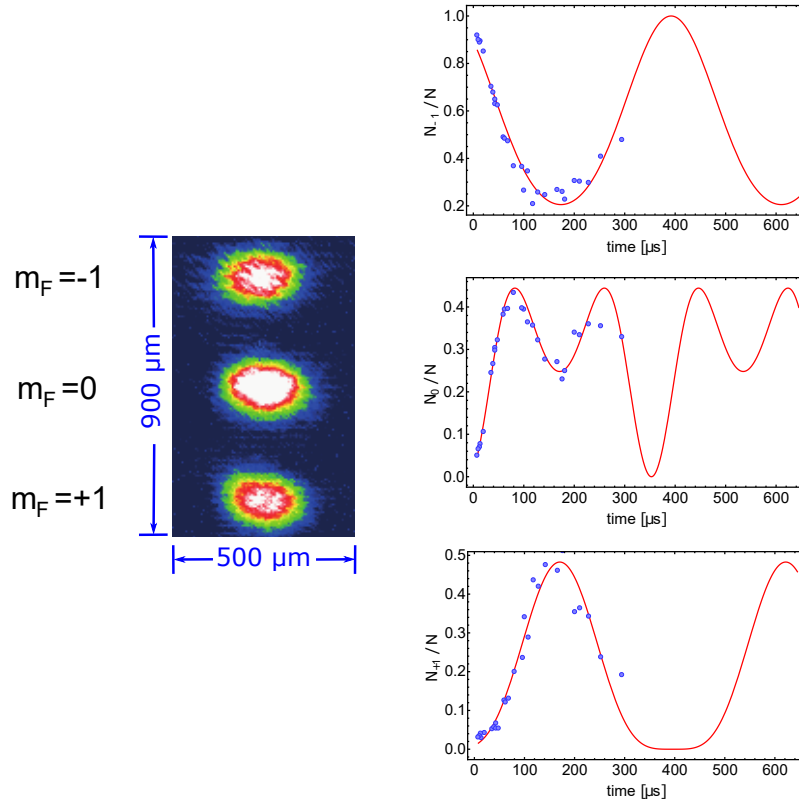


Figure 4.17: Images of the BEC in states $|F = 1, m_F = -1, 0, +1\rangle$ and the population oscillation in the three states. The blue dots are the experimental data and the red curve is the fit.

In the experiment, we perform these Rabi oscillation measurements on a condensate in the $|F = 1, m_F = -1\rangle$ state in the Z-wire magnetic trap. The trap bottom is 657 kHz which can be measured precisely from RF spectra. A RF pulse of frequency 653 kHz and amplitude $V_{pp} = 2 \text{ V}$ is applied for a duration t . The condensate is held in the trap for $t_{hold} = 0.2 \text{ ms}$. The population of the three Zeeman levels is driven by varying the pulse duration. Atoms in the $m_F = -1$ state remain trapped in the same position since the magnetic field gradient holds atoms against gravity. At the same time, atoms in the $m_F = 0$ state fall out of the trap with acceleration g since they are not sensitive to the magnetic field to a first order approximation. In contrast to the $m_F = -1$ state, atoms in the $m_F = +1$ are accelerated downwards by the magnetic field gradient plus gravity with an acceleration of $2g$. Therefore, the components $m_F = -1, 0$ and $+1$ acquire initial velocities of $0, gt_{hold}$ and $2gt_{hold}$,

respectively, and are spatially separated after a free expansion time. We image all the components simultaneously in free fall after transferring them to the $F = 2$ state with a short repumper pulse. Our measurement is shown in Fig. 4.17.

Fitting the measured data with Eq.(4.11) yields a coupling strength $\Omega_0/2\pi = 2.6$ kHz and a detuning $\Delta/2\pi = 0.96$ kHz. This relatively weak coupling indicates the earlier RF spectra measurements are not limited by RF radiation power broadening.

4.6 Summary

This chapter started with a presentation of the experimental set-up. This mainly contains three parts: the vacuum system, the laser system and the computer control system. A versatile control system was developed to produce well defined sequences for our daily BEC experiment. Then the experiment procedures from the initial MOT loading to the final evaporative cooling to achieve a BEC are summarised. Absorption imaging as the main diagnostic method is also discussed. From an analysis of the absorption images, the trap frequencies of the Z-wire magnetic trap and lifetime of the atoms trapped in the Z-wire trap are studied. Finally, the emergence of a BEC is characterised by a bimodal distribution fit, anisotropic expansion and RF spectra.

CHAPTER 5

Loading atoms into the $0.7\ \mu\text{m}$ -period triangular magnetic lattice

In this chapter I present experiments towards loading the $0.7\ \mu\text{m}$ -period triangular magnetic lattice. As the lattice period is scaled down to the sub-micron regime, the magnetic lattice traps are located at distances of only hundreds of nanometres from the magnetic film. The atom-surface interactions are first studied by bringing the Z-wire trapped atoms very close to the chip surface. Measurements of the Z-wire trap lifetimes and the remaining atom fraction at distances down to about a few micrometres are described. Then the interaction with the short-range magnetic lattice potential located a few hundreds nanometres from the chip surface is studied. Finally, preliminary results for loading atoms into the $0.7\ \mu\text{m}$ -period triangular lattice are presented. The measured short lifetimes of the atoms trapped in the magnetic lattice are consistent with a model based on surface-induced thermal evaporation.

The preliminary experiments for loading the $0.7\ \mu\text{m}$ -period magnetic lattice were carried out jointly with PhD student Tien Tran and the experimental data presented in Figures 5.15 and 5.16 were taken by him.

5.1 Z-wire trapped atoms-surface interactions

The sub-micron period magnetic lattices are designed for possible quantum tunnelling in these systems. Since the strength of the surface magnetic field decays exponentially from the film surface, the distance of the created lattice traps from the film surface is usually limited within the lattice period. For a 0.7 μm -period magnetic lattice, this means that the distance from the magnetic film surface to the trapped atoms is hundreds of nanometres. On the one hand, the atom-surface interaction can be important at such a short distance. On the other hand, the trapped atoms can be considered as an extremely sensitive probe to measure these elusive interactions which are difficult to measure in other situations.

5.1.1 Z-wire trap distance calibration

A strategy for loading a 0.7 μm -period magnetic lattice located about hundreds of nanometres from the chip surface is required to smoothly merge the Z-wire trap with the magnetic lattice traps. Therefore, it is important to study the surface effects on the Z-wire trapped atoms before they are loading into the magnetic lattices. First of all, an accurate calibration of the distance between the chip surface and the centre of the Z-wire trap is needed.

A simple experiment is performed to measure this distance by imaging a cloud *in situ*, i.e., without time of flight [160]. When the atom cloud is brought close to the chip surface, the imaging beam is tilted by a small angle ($\theta \sim 2^\circ$) such that it reflects from the surface so that two beam paths traverse the cloud. One beam first passes through the atom cloud and then reflects from the surface, while the second beam first reflects from the surface and then passes through the atom cloud. This creates both a direct image and a mirror image of the cloud simultaneously in the absorption image, see Fig. 5.1 (a). The distance between the cloud centres is $2d\cos\theta \approx 2d$, where d is the distance of the trap centre to the surface of the gold reflecting layer. At very small distances the two images merge into one due

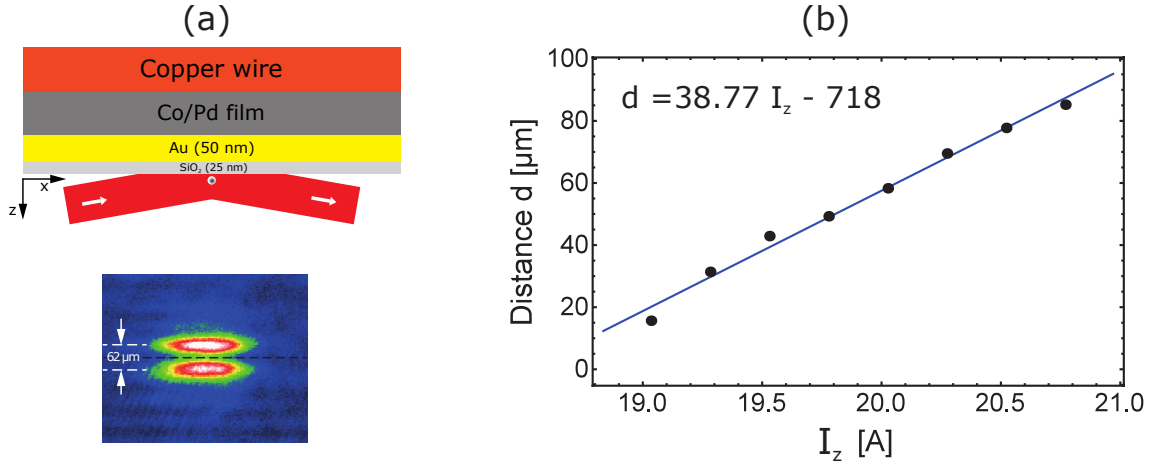


Figure 5.1: Distance calibration of the Z-wire trap near the chip surface. (a) Top panel: atom chip structure and the imaging geometry. Bottom panel: a typical *in situ* reflective absorption image of the cloud near the surface. Both direct and mirror images are visible. (b) Measurements of the distance d from the trap centre to the gold reflecting layer on the chip surface versus Z-wire current I_z for $B_x = 51.8$ G. Solid line is a linear fit: $d = (38.8 \pm 1.6)I_z - (718 \pm 33) \mu\text{m}$, where the uncertainties are 1σ statistical uncertainties.

to the finite size of the cloud and the finite resolution of the imaging system. To determine these small distances we use an extrapolation based on the best fit to the experimental measurements.

The experimental results are plotted in Fig. 5.1 (b). The vertical positions of the cloud centres in CCD pixels are measured from a Gaussian fit to the cloud in the trap and then converted into micrometres from the measured effective pixel size. The measured data fit well to a linear relationship, where the intercept $d(I_z = 0) = -718 \mu\text{m}$ corresponds approximately to the estimated distance of the gold mirror from the current-carrying copper wires. The effect of the finite size wire structure (width 1 mm) is small at this distance. Based on the distance calibration, further measurements can be performed at trap centre distances down to a few micrometers from the chip surface.

5.1.2 Trap lifetime versus Z-wire trap distance

To investigate surface-induced losses, we measure the trap lifetime as a function of the distance d of the Z-wire trap centre to the chip surface. In each measurement, the atom cloud in the initial Z-wire trap ($I_z = 37.6$ A, $B_x = 51.8$ G) is prepared ~ 670 μm from the surface. To bring the atoms closer to the surface, the Z-wire current is then smoothly ramped down in the next 150 ms. During this stage the bias field B_x is kept constant. The final position of the Z-wire trap is determined from the final current I_z according to the calibration. The atom cloud is held in the final position for different holding times, and the remaining atoms are imaged by absorption. At large distances where the direct image and the mirror image can be resolved, the atom number is read directly from the measurement of the direct image. At small distances where the two images are merged, the atom number is estimated as half of the total measured atom number.

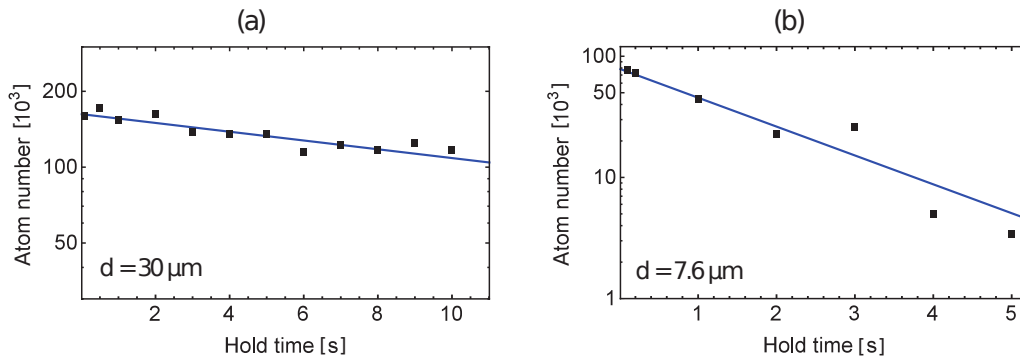


Figure 5.2: Trap loss at different atom-surface distances: (a) $d = 30 \mu\text{m}$, (b) $d = 7.6 \mu\text{m}$. Data points (black squares) are plotted on a log scale. The measured lifetimes are 25 ± 4 s at $d = 30 \mu\text{m}$ and 1.82 ± 0.26 s at $d = 7.6 \mu\text{m}$.

The cloud is evaporatively cooled to a temperature above T_c , $T \sim 1.5 \mu\text{K}$, and the trap bottom B_{IP} is adjusted to about 0.7 MHz (1 G). Figure 5.2 shows two trap loss measurements for the Z-wire trap at $d = 30 \mu\text{m}$ and $d = 7.6 \mu\text{m}$, respectively. For $d = 30 \mu\text{m}$ the Z-wire trap is far away from the surface. An exponential decay of the atom number with a rate $\gamma_0 = (25 \pm 4 \text{ s})^{-1}$ is observed. This trap loss is attributed mainly to collisions with background atoms. This is confirmed by the

observation of a distance-independent loss rate for $d > 10 \mu\text{m}$ in Fig. 5.3. Therefore, the background (one-body) loss rate should be close to $\gamma_{bg} = (25 \pm 4 \text{ s})^{-1}$. When the trap is brought closer to the surface at $d = 7.6 \mu\text{m}$, we observe a much faster loss rate $\gamma_0 = (1.82 \pm 0.26 \text{ s})^{-1}$. The increased loss rate cannot be explained by an increase in γ_{bg} , because during all the measurements no clear background pressure change in the vacuum chamber was observed.

We account for the faster loss by adding surface-induced losses. First, we consider the effect of Johnson noise. The fluctuating magnetic field caused by the thermal current noise (at room temperature $T \sim 300 \text{ K}$) in a conductor may couple to the magnetic moment of the trapped atoms to drive a spin-flip transition. Our hybrid atom chip has a $t_{Au} = 50 \text{ nm}$ thick reflecting gold layer on top of the magnetic film and a $127 \mu\text{m}$ thick copper current-carrying wire structure underneath. Since the copper wire (the Z-wire) is far away ($> 700 \mu\text{m}$) from the Z-trap, the effect on the spin-flip loss is small and can be neglected [166]. For a gold conductor and a trap bottom (1 G) corresponding to a Larmor frequency of $\omega_L/2\pi \sim 0.7 \text{ MHz}$, we obtain a skin depth $\delta \sim 94 \mu\text{m}$ ($\delta = \sqrt{2/(\sigma\mu_0\omega_L)}$, Sect. 2.7.1). Our measurements are within the regime $\delta \gg \max\{d, t_{Au}\}$, and therefore the spin-flip rate can be calculated from Eq.(2.40). At a distance $d = 7.6 \mu\text{m}$, this value is $\gamma_s = 1/\tau_s = (150 \text{ s})^{-1}$. In order to estimate the measured trap lifetime, both the background collision-limited lifetime τ_{bg} and the spin-flip-limited lifetime τ_s should be taken into account: $\tau = (1/\tau_{bg} + 1/\tau_s)^{-1}$.

In Figure 5.3 we show the measured trap lifetime versus distance d of the trap centre from the chip surface on a log scale. The measurements show that when the trap distance $d > 10 \mu\text{m}$, the measured lifetime is almost constant, $\tau \approx 25 \text{ s}$, with no significant lifetime reduction observed. In the small distance regime, $d < 10 \mu\text{m}$, the lifetime decrease is rapid with distance. The estimation based on spin-flips and background collisions (solid red curve) cannot explain this fast decay. For comparison, we also plot the fundamental limit due to Johnson noise only (dashed red curve). In principle, the Johnson noise can be effectively reduced by using a thinner and narrower layer of conductor or a reflective conductor with higher

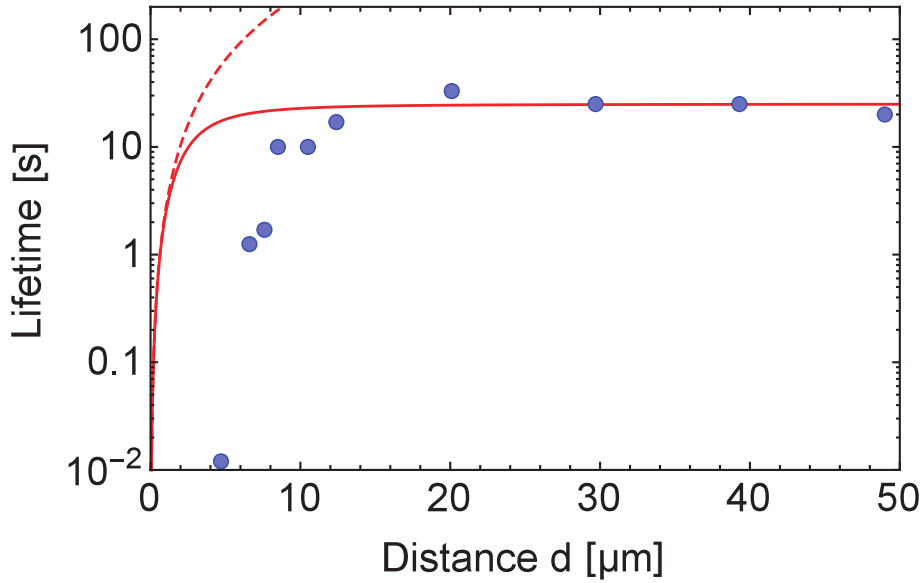


Figure 5.3: Measured lifetimes (blue points) on a log scale versus distance d of the centre of the Z-wire trapped cloud from the chip surface. The solid red curve (dashed red curve) is the calculated lifetime due to spin-flip loss from Johnson noise plus background collisions (due to spin-flip loss only).

resistivity such as palladium. However, this is not the main limitation in our present experiment performed near the chip surface (a few micrometer distances). The trap lifetimes at small d are significantly shorter than what is expected from spin-flip transitions [166].

Secondly, we consider the loss caused by 3-body recombination. The estimation of the 3-body recombination lifetime is determined by the cloud density. In these measurements, the highest possible cloud density is about $6.65 \times 10^{12} \text{ cm}^3$ based on $\sim 4 \times 10^5$ atoms at temperature $T = 1.5 \mu\text{K}$ trapped in a Z-wire trap with trapping frequency $\omega_r/2\pi = 300 \text{ Hz}$ and $\omega_{ax}/2\pi = 20 \text{ Hz}$. The calculated lifetime is $\tau_{3b} \approx 500 \text{ s}$. Therefore, the additional trap loss is most likely caused by surface-induced evaporation. Because of the attractive Casimir-Polder interaction, when the trap approaches the surface of the chip, the trap depth decreases accordingly. This leads to an additional trap loss.

5.1.3 Atom fraction versus Z-wire trap distance

To test the above explanation, we measure the remaining atom fraction χ versus distance d . Starting with N_i atoms in a Z-wire trap at distance d_i far away from the surface, we move the trap to a distance $d < d_i$ by decreasing the Z-wire current I_z . The cloud is held there for a certain time t_0 , then quickly moved back to its original location, where the remaining number of atoms N_f is measured.

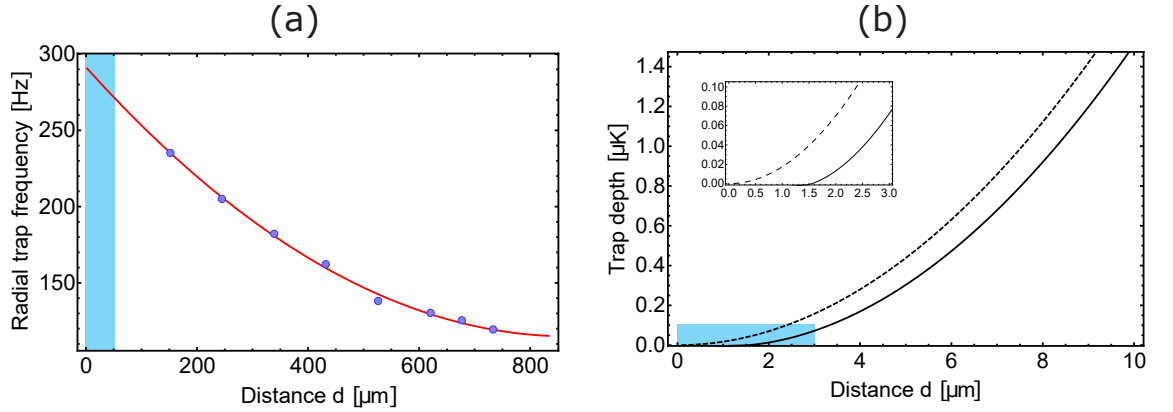


Figure 5.4: (a) Z-wire radial trap frequency as a function of trap-surface distance d . The blue points are dipole-oscillation measurements at different positions. The red curve is the best fit. The blue area (at distance smaller than $50 \mu\text{m}$) highlights the region of interest. (b) Theoretical calculations of the trap depth for the Z-wire trap using the fitted trap frequency $\omega_r/2\pi = 291.43 - 0.4055d + 0.00023d^2$ Hz. The dashed (solid) curve shows the calculation without (with) the Casimir-Polder interaction V_t ($V_t(z) + V_{CP}$), where $V_t = \frac{1}{2}M\omega_r^2d^2$. The inset shows a zoom of the blue area.

As discussed before, because the attractive Casimir-Polder potential V_{CP} lowers the trap depth to V_b , the trap finally disappears at a finite distance from the chip surface. When the Z-wire trap is close to the surface, it can be approximated by a simple harmonic trap $V_t(z)$. We simply model the atom loss from the combined trapping potential $V_t(z) + V_{CP}$ as a sudden truncation of the tail of the Boltzmann energy distribution of the trapped cloud due to the finite trap depth V_b . The remaining fraction of atoms is given by $\chi = 1 - \exp(-\eta)$, where $\eta = V_b/(k_B T)$ is the truncation parameter. It is difficult to measure the Z-trap frequency by the dipole-oscillation

method at small distances from the surface. In the experiment we measure a sequence of trap frequencies as the Z-wire trap approaches the surface and extrapolate the value to our region of interest. The measurements are presented in Fig. 5.4 (a). We choose the fitted Z-wire trap frequency $\omega_r/2\pi = 291.43 - 0.4055d + 0.00023d^2$ Hz when the trap-surface distance is within $50 \mu\text{m}$. In Fig. 5.4 (b), we show calculations of the trap depth with and without the Casimir-Polder interaction for a trap frequency using $C_4 = 8.2 \times 10^{-56} \text{ Jm}^4$ for a silica surface, Sect. 2.7.2. When including the Casimir-Polder interaction, the trap depth reduces to $\sim 1.5 \mu\text{K}$ at distance $d = 10 \mu\text{m}$, and further reduces to $\sim 250 \text{ nK}$ at $d = 5 \mu\text{m}$. Finally, the trap depth disappears at about $1.5 \mu\text{m}$ from the chip surface. In our previous lifetime measurements, the initial temperature of the cloud was about $1.5 \mu\text{K}$. According to this calculation, the barrier height becomes comparable with the cloud temperature at around $d = 10 \mu\text{m}$. Therefore, additional atom loss is expected to occur within this distance.

For the atom fraction measurements, we start with a Z-wire trapped cloud at an initial position $d_i = 100 \mu\text{m}$ from the chip surface. The cloud temperature and the atom number is controlled by the RF knife position during evaporative cooling. Then this cloud is brought closer to the chip surface at various distances d by ramping down the current I_z and holding there for $t_0 = 10 \text{ ms}$. Then the cloud is moved back to its original position and imaged. Figure 5.5 shows the measured atom fraction χ versus distance d for a condensate ($T \approx 200 \text{ nK}$) well below the critical temperature ($T_c \approx 520 \text{ nK}$), and for thermal clouds at about 600 nK , $1 \mu\text{K}$ and $2 \mu\text{K}$. The temperature of the cloud is measured by time of flight in which the thermal wing of the cloud is fitted with a Gaussian distribution; so the uncertainty increases when the temperature is close to and below T_c .

The measurements show that the thermal cloud exhibits loss at a much larger distance than the condensate. For a thermal cloud at $T \sim 2 \mu\text{K}$, the loss starts at $d \sim 20 \mu\text{m}$ and for a condensate the loss appears at $d \sim 5 \mu\text{m}$. The solid curves are theoretical fits based on $\chi = 1 - e^{-\eta}$. The only fitting parameter is the cloud temperature T . Our fitted values are 195 nK , 480 nK , $0.95 \mu\text{K}$ and $1.7 \mu\text{K}$ for the

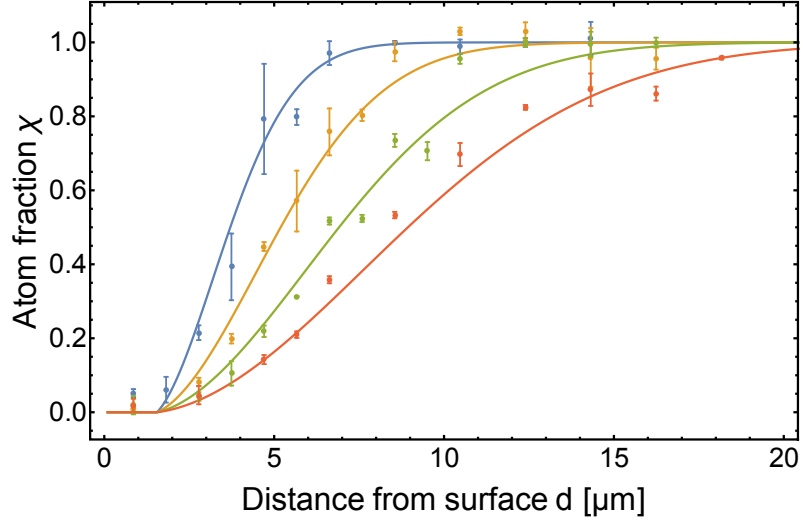


Figure 5.5: Remaining atom fraction χ in the Z-wire trap versus distance d of the cloud centre from the chip surface for a BEC at $T \approx 200$ nK (blue points) and for a thermal cloud at about 600 nK (gold points), 1 μ K (green points) and 2 μ K (red points), for $B_x = 51.8$ G. Solid curves are theoretical fits using the simple truncation model with $T = 195$ nK (blue), 480 nK (gold), 0.95 μ K (green) and 1.7 μ K (red).

blue, gold, green and red curves, respectively. These values are comparable to the temperatures measured by time of flight. No atom loss is only expected when $V_b \rightarrow \infty$ ($\eta \rightarrow \infty$) from the model $\chi = 1 - e^{-\eta}$. When η reduces to 3 only 5% of atoms are lost from the trap. This means for $T = 1.7$ μ K (red), 0.95 μ K (green), 480 nK (gold) and 195 nK (blue) cloud the losses kick in at V_b reduces to about 5.1 μ K, 2.9 μ K, 1.4 μ K and 590 nK which corresponding to distance $d \approx 18$ μ m, 13 μ m, 10 μ m and 6 μ m.

The above simple truncation model can be extended to include the effect of 1D surface evaporation in which the more energetic atoms in the trap region near the chip surface preferentially escape the trap during the $t_0 = 10$ ms holding time, since for the thermal cloud $T = 2$ μ K (atom number $N \approx 4.5 \times 10^6$), the elastic collision time $\tau_{el} \approx 1.6$ ms which is shorter than the holding time. For the colder and denser cloud the elastic collision time will be reduced further. Using a classical 1D surface evaporation model [55], the remaining atom fraction becomes $\chi = \chi_0 e^{-\Gamma_{ev} t_0}$, where $\chi_0 = 1 - \exp(-\eta)$ and $\Gamma_{ev} = f(\eta) e^{-\eta} / \tau_{el}$ is the loss rate due to 1D surface

evaporation, $f(\eta) \approx 2^{-5/2}(1 - \eta^{-1} + \frac{3}{2}\eta^{-2})$ for $\eta \geq 4$ [167]. In Fig. 5.6 we compare fits for the 1D surface evaporation model (solid purple curve) and the simple truncation model (solid blue curve) for the condensate at about 200 nK. To obtain a good fit, the temperature of the cloud $T = 120$ nK and the elastic collision time $\tau_{el} = 0.7$ ms are required. Therefore, surface-induced 1D evaporation indeed can cool the cloud close to the surface; this has been demonstrated as an alternative to RF evaporative cooling to obtain a BEC [166]. The discrepancy at small atom fraction ($\chi < 0.4$) is probably due to the simple 1D evaporation model which breaks down for $\eta \leq 1$ and assumes a constant cloud temperature with decreasing distance. In the experiment, we also observed that the atom fraction curve shifts towards the chip surface when the holding time t_0 and hence the amount of surface evaporation is reduced. This is consistent with the model.

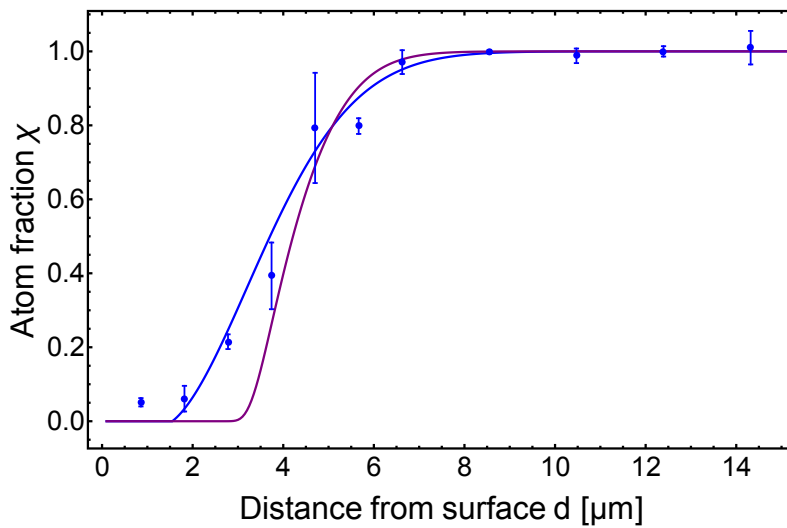


Figure 5.6: Remaining atom fraction χ versus distance d from the chip surface for a BEC at $T \approx 200$ nK, for $B_x = 51.8$ G. Blue curve: simple truncation model using $T = 195$ nK. Purple curve: 1D surface evaporation model using $T = 120$ nK and $\tau_{el} = 0.7$ ms.

Due to the attractive Casimir-Polder interaction, the trap depth disappears at about $d = 1.5 \mu\text{m}$. Our measurements are consistent with this prediction. To compensate this effect and to maintain a trap at a distance of a few hundred nanometers, the trap frequency needs to be high. In the next section, we show that our magnetic lattice trapping is strong enough to compensate the Casimir-Polder interaction in

this regime.

5.2 Loading a sub-micron period magnetic lattice: simulation

There are four lattice structures patterned on the Co/Pd multilayer magnetic film: 0.7 μm -period square and triangular magnetic lattices, and 0.7 μm -period and 5 μm -period 1D magnetic lattices. The magnetic film is 10.34 nm thick with a magnetisation $M_z = 470 \text{ kA}\cdot\text{m}^{-1}$ ($4\pi M_z = 5.9 \text{ kG}$). In this section, it is important to address whether the produced magnetic lattice traps are tight enough to compensate the Casimir-Polder interaction at distances of hundreds nanometres from the chip surface.

5.2.1 0.7 μm -period 2D magnetic lattice

The optimised 0.7 μm -period square and triangular magnetic lattice potentials can be created with bias fields $B_x = 7.86 \text{ G}$, $B_y = -3.76 \text{ G}$ and $B_x = 0.50 \text{ G}$, $B_y = 4.52 \text{ G}$, respectively. The optimised lattice traps are located at $z_{min} = a/2 = 350 \text{ nm}$ from the magnetic film, where $a = 0.7 \mu\text{m}$ is the lattice period. Including the 75 nm thick coating layer (50 nm gold and 25 nm silica) on the magnetic film, the distance between the optimised 2D magnetic lattice traps and the chip surface is only 275 nm. In this region, as discussed in the previous section, the Casimir-Polder interaction is the dominant atom-surface interaction. It may alter the shape of the lattice traps and cause additional atom loss. We have simulated this situation and the contour plots of the trap potentials are presented in Fig. 5.7. The optimised magnetic lattices are still available even including the Casimir-Polder interaction. Furthermore, the Casimir-Polder effect for these optimised 0.7 μm -period magnetic lattices can be neglected due to the large lattice trap frequencies (as high as hundreds kilohertz).

The calculated trap parameters for the optimised magnetic lattice are listed in Table 5.1. For the square lattice, each individual lattice trap is approximately

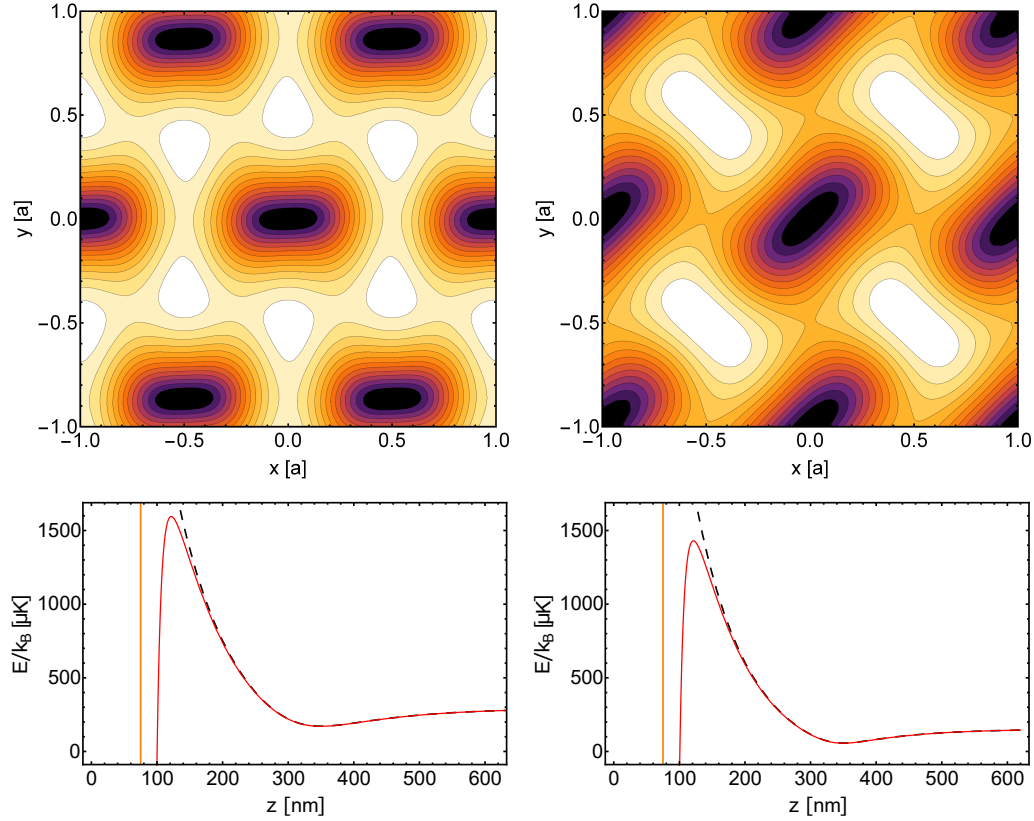


Figure 5.7: The upper panels show contour plots of the optimised 0.7 μm -period square (left) and triangular (right) magnetic lattice potentials with bias fields $\{B_x = 7.86$ G, $B_y = -3.76$ G $\}$ and $\{B_x = 0.50$ G, $B_y = 4.52$ G $\}$, respectively, at $z_{\min} = a/2 = 350$ nm. The lower panels show calculated trapping potentials for ^{87}Rb $|F = 1, m_F = -1\rangle$ atoms trapped in the optimised 0.7 μm -period square (left) and triangular (right) magnetic lattice. Black dashed lines are the magnetic lattice potentials and the red solid lines include the Casimir-Polder interaction with $C_4 = 8.2 \times 10^{-56}$ Jm 4 for a silica surface. The vertical gold lines indicate the position of the silica surface ($z = 75$ nm). Magnetic film parameters: magnetization $4\pi M_z = 5.9$ kG, film thickness $t_m = 10.34$ nm.

cylindrically symmetric with the long axis in the $\{1,1,0\}$ direction and the trap bottom $B_{IP} = 5.11$ G. The barrier heights are equal in the x - and y -directions, 6.56 G above the trap bottom. This corresponds to a barrier height of 220 μK for ^{87}Rb atoms in the $|F = 1, m_F = -1\rangle$ state. The barrier height in the z -direction is 3.61 G (121 μK). The geometric mean trap frequency is $\bar{\omega}/2\pi = 173$ kHz. For the triangular lattice, the symmetrical axis (Ioffe axis) of each lattice trap is oriented

approximately along the x -direction and the trap bottom $B_{IP} = 1.69$ G. The barrier heights are 5.97 G (200 μ K) above the trap bottom and equal in all three lattice directions in the xy -plane. In the z -direction the barrier height is 2.85 G (96 μ K). The geometric mean trap frequency is $\bar{\omega}/2\pi = 195$ kHz.

As discussed in Sect. 4.5.4, since the magnetic trap is conservative the optimised loading process is adiabatic, which means the phase space density Φ is preserved. When transferring atoms from the Z-wire trap to the magnetic lattice traps, a significant increase in trapping frequency results in appreciable heating of the atom cloud. The temperature of the lattice cloud due to the adiabatic compression can be estimated by $T_{lattice} = \frac{\bar{\omega}_{lattice}}{\bar{\omega}_{Ztrap}} T_{Ztrap}$, where $\bar{\omega} = (\omega_x \omega_y \omega_z)^{1/3}$ is the geometrical mean trapping frequency. For both lattices, the geometric mean trap frequency is $\sim 10^3$ times larger than the geometric mean trap frequency of the Z-wire trap ($\bar{\omega}_{Ztrap}/2\pi \approx 144$ Hz). Therefore, a large heating of the cloud due to adiabatic compression is expected during the loading process. In addition, the atom cloud may experience a large three-body recombination rate because of the high trap frequencies and hence large atom densities. All of these contributions can limit the lifetime of the magnetic lattice traps. More detailed discussions are presented in Sect. 5.4.

Table 5.1: Calculated trapping parameters for the optimised 2D magnetic lattices

	Square Lattice	Triangular Lattice
Period	0.7 μ m	0.7 μ m
Trap height z_{min}	0.35 μ m	0.35 μ m
Bias field $\{B_x, B_y, B_z\}$	{7.86 G, -3.76 G, 0}	{0.50 G, 4.52 G, 0}
Barrier height in lattice directions	6.56 G (220 μ K)	5.97 G (200 μ K)
Barrier height in z -direction	3.61 G (121 μ K)	2.85 G (96 μ K)
Trap bottom	5.11 G	1.69 G
Trap frequency	$\omega_z/2\pi = 260$ kHz $\omega_{\perp}/2\pi = 254$ kHz $\omega_{\parallel}/2\pi = 79$ kHz $\bar{\omega}/2\pi = 173$ kHz	$\omega_z/2\pi = 314$ kHz $\omega_y/2\pi = 307$ kHz $\omega_x/2\pi = 77$ kHz $\bar{\omega}/2\pi = 195$ kHz

5.2.2 0.7 μm -period 1D magnetic lattice

The loading procedure for a 1D 0.7 μm -period magnetic lattice is similar to that which we demonstrated previously for the 1D 10 μm -period magnetic lattice [155]. The simulations are shown in Fig. 5.8. The Z-wire trap which is initially far away ($\sim 670 \mu\text{m}$) from the chip surface is brought closer to the lattice traps by ramping down the Z-wire current I_z . The Z-wire trap smoothly merges with the magnetic lattice traps at $I_z = 18.2 \text{ A}$, $B_x = 52 \text{ G}$. The lattice traps are located $\sim 480 \text{ nm}$ from the chip surface ($d = z_{\text{min}} - (t_{\text{Au}} + t_{\text{SiO}_2}) = z_{\text{min}} - 75 \text{ nm}$), Fig. 5.8 (d). According to the calculations, the Casimir-Polder interaction does not change the shape of the lattice traps at this trapping distance.

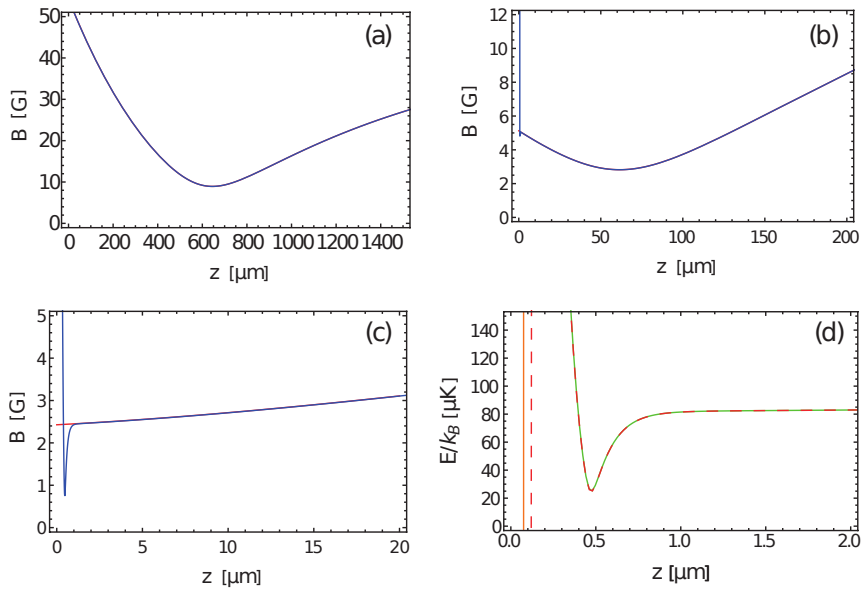


Figure 5.8: Radia simulations for loading a 0.7 μm -period 1D magnetic lattice from a Z-wire trap. Z-wire currents are $I_z =$ (a) 37.6 A, (b) 20 A, (c) 18.2 A, and a bias field $B_x = 52 \text{ G}$. The red curves show the trapping magnetic field of the Z-wire trap. The blue curves show the combined trapping magnetic field of the Z-wire and the magnetic lattice. (d) Zoom of plot (c) in temperature units while taking the Casimir-Polder interaction into account. The green solid line plots the magnetic lattice trapping potential for ^{87}Rb $|F = 1, m_F = -1\rangle$ state atoms. The red dashed line includes the Casimir-Polder interaction (off scale) with coefficient $C_4 = 8.2 \times 10^{-56} \text{ Jm}^4$ for a silica surface. The gold line indicates the position of the chip surface.

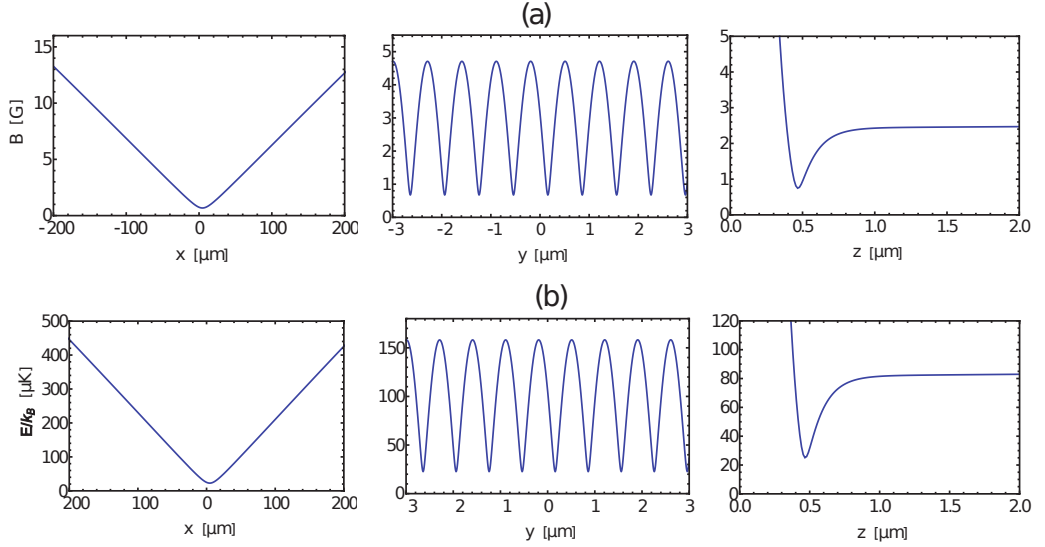


Figure 5.9: Calculated trap potential of the created 1D $0.7 \mu\text{m}$ -period magnetic lattice for $I_z = 18.2 \text{ A}$, $B_x = 52 \text{ G}$. (a) Magnetic field of the lattice along the x -, y -, z - directions. (b) Corresponding trapping potential for ^{87}Rb $|F = 1, m_F = -1\rangle$ state atoms in temperature units.

The lattice trap created with the parameters $I_z = 18.2 \text{ A}$ and $B_x = 52 \text{ G}$ is shown in Fig. 5.9. The calculated radial trap frequency is $\omega_r/2\pi = 212 \text{ kHz}$ and the axial trap frequency $\omega_{ax}/2\pi = 675 \text{ Hz}$. The geometric mean trap frequency $\bar{\omega}/2\pi = 31 \text{ kHz}$, so the adiabatic compression in transferring the atom cloud from the Z-wire trap to the 1D magnetic lattice is smaller than in the 2D case because of the weak confinement along the axial direction.

5.3 Projection of ultracold atoms towards the 2D lattice potential

Before loading the $0.7 \mu\text{m}$ -period magnetic lattice, it is important to check that the ultracold atoms can interact with the short-range magnetic lattice potential. This is to ensure that the magnetic film is still strongly magnetised after the vacuum baking and that the atom cloud is actually reaching the magnetic lattice potential, a few hundreds nanometres from the chip surface, without being lost. Then, by

fine tuning the experiment parameters, we will attempt to load the 0.7 μm -period triangular magnetic lattice and look for a signal of the trapped atom cloud.

Figure 5.10 shows the calculated magnetic potential pattern produced by the magnetic film structure itself without any bias fields. The 2D magnetic film structures still produce a certain periodic potential pattern (but without magnetic lattice traps since there are no trap minima in the z -direction, which need bias fields to provide the required field cancellation) and the produced potential pattern is quite robust at various distances from the surface. Interestingly, the square lattice structure creates a square potential pattern with a period of $\sqrt{2}a$ while the triangular lattice structure creates a potential pattern which looks like an array of 1D chains. The magnetic potential pattern for the triangular structure has a larger barrier in the y -direction than in the x -direction and the pattern period is about $a/2 = 350$ nm in the x -direction and about $a = 700$ nm in the y -direction. The magnetic field magnitude decays exponentially in the vertical z -direction from the surface.

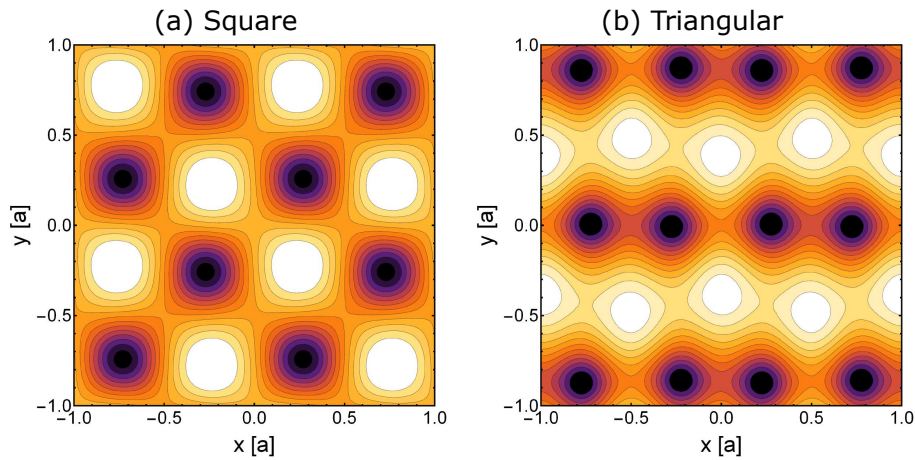


Figure 5.10: 2D magnetic lattice potential patterns created by (a) a square lattice structure and (b) a triangular lattice structure, without bias fields and in the plane $z = a/2$. Lattice period $a = 0.7 \mu\text{m}$.

When an atom moves in such a magnetic potential field, the force experienced by the atom is given by $F = -\nabla U(x, y, z) = -m_F g_F \mu_B \nabla |B(x, y, z)|$. Therefore, atoms feel a strong repulsive force when approaching the surface and finally can be reflected back. Singh et al. [108, 109] have previously demonstrated the atom cloud reflection

from the 1D $10\ \mu\text{m}$ -period magnetic grating structure. A 1D corrugated magnetic potential is formed in the presence of a B_y bias field. Since the corrugation only appears in one direction (y -direction), both the experiment and calculation show that the lateral expansion of the cloud only occurs in this direction, resulting in an arc-shaped reflected atom cloud. For the more complicated potential pattern formed by the 2D magnetic lattice structures, corrugations in both x - and y -directions are expected to introduce force components parallel to the magnetic film surface which lead to a lateral expansion of the cloud in both directions when ultracold atoms are reflected from the magnetic potential. In our experiment configuration, one of the directions overlaps with the imaging beam path, so we expect the reflected cloud to have a half-moon shape.

5.3.1 Reflection from a $0.7\ \mu\text{m}$ -period triangular magnetic potential

In this experiment, the ultracold cloud is projected vertically towards the magnetic film structure and the reflection signal from the corrugated magnetic potential is recorded. An ultracold atom cloud at about 200 nK, below the critical temperature, is first prepared in a Z-wire trap $\sim 670\ \mu\text{m}$ below the surface. Then the cloud is positioned at different distances d_0 close to the $0.7\ \mu\text{m}$ -period triangular magnetic lattice structure by ramping down the Z-wire current I_z . To launch the cloud vertically, the Z-wire trap is switched off suddenly by turning off the Z-wire current I_z and the bias field B_x . During this period I_z rapidly decreases to zero (in $\sim 1\ \text{ms}$) while B_x , which is produced by external coils, decreases slowly (in $\sim 10\ \text{ms}$) compared to the Z-wire current. This delay gives a momentum kick (launching velocity $\sim 70\ \mu\text{m}/\text{ms}$) to the atom cloud, thus launching the cloud. A series of measurements is made by launching the cloud at different positions and monitoring the reflection dynamics after different waiting times. The measurements are presented in Fig. 5.11. When the launching position is too far from the surface, $d_0 = 145\ \mu\text{m}$, no reflection is observed. The atom cloud falls down under gravity before it can reach the magnetic

potential. More importantly, no lateral expansion is observed. Since the cloud is cooled below the critical temperature, thermal expansion in the lateral direction should be very small and can be neglected. Reflections start to appear when the launching position approaches $d_0 = 128 \mu\text{m}$; both the free falling part and the reflected part are observed. As shown in Fig. 5.11 (b), the cloud splits into two parts when it turns back from the surface the lower cloud which expands in the lateral direction (parallel to the surface) is the reflected part and the upper cloud which remains almost constant in the lateral dimension is the free falling part. Finally, clear reflections are observed at $d_0 = 76$ and $67 \mu\text{m}$. The reflected clouds show a half-moon shape and the lateral dimension after reflection by the magnetic lattice potential is up to three times larger than the dimension of the incident cloud.

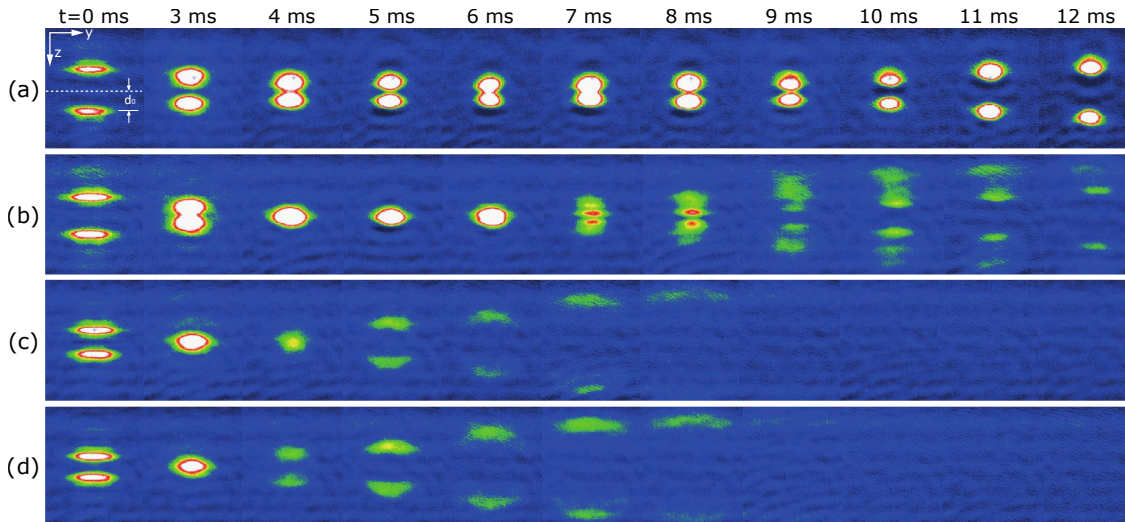


Figure 5.11: Reflection absorption images of the time evolution of an ultracold atom cloud projected towards the magnetic lattice potential with no bias fields. Launching position $d_0 =$ (a) $145 \mu\text{m}$, (b) $128 \mu\text{m}$, (c) $76 \mu\text{m}$, (d) $67 \mu\text{m}$ from the chip surface. Both the direct and the mirror images are visible due to the reflection absorption imaging geometry. The white dashed line in (a) indicates the position of the reflecting surface.

An accurate simulation of the reflection dynamics requires detailed knowledge of factors such as the lattice potential, the launching velocity and stray magnetic fields. Here, we apply a simple analysis to capture the main features of the reflection dynamics. The width of the cloud in the lateral direction (σ_Y) and the cloud position

in the vertical direction (d) are plotted versus the projection time t in Fig. 5.12. Without reflection, the lateral width remains almost constant at $\sim 50 \mu\text{m}$ and the trajectory of the cloud in the vertical direction can be fitted with a single quadratic function. For the case of reflection, the lateral width increases approximately linearly with time after reflection, with a slope corresponding to lateral velocities of $30 \mu\text{m/ms}$ for $d_0 = 67 \mu\text{m}$ and $21 \mu\text{m/ms}$ for $d_0 = 76 \mu\text{m}$. In the vertical direction, two quadratic functions are required to fit the cloud trajectory. This implies that the incident velocity towards the lattice potential is not equal to the exit velocity after reflection. From the fitting we find that for $d_0 = 67 \mu\text{m}$ the incident velocity is $60 \mu\text{m/ms}$ and the exit velocity is $45 \mu\text{m/ms}$, while for $d_0 = 76 \mu\text{m}$, the incident velocity is $52 \mu\text{m/ms}$ and the exit velocity is $45 \mu\text{m/ms}$. Generally, the initial launching velocity increases when the cloud approaches the surface. The reflection of the cloud starts to occur at a certain launching velocity and becomes stronger over a certain range of launching velocities and finally disappears for launching velocities much larger than $70 \mu\text{m/ms}$.

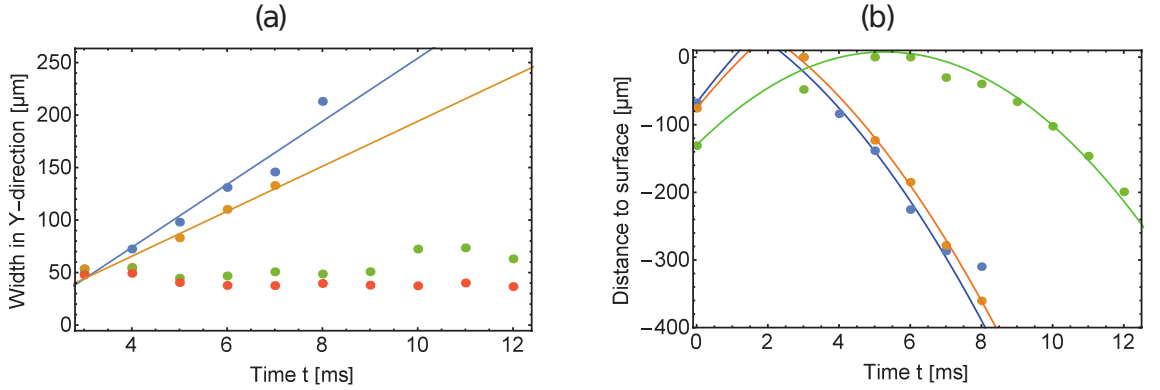


Figure 5.12: Time evolution of (a) the lateral widths along y and (b) the vertical positions of the ultracold atom cloud projected towards the magnetic lattice potential. Launching positions $d_0 = 67 \mu\text{m}$ (blue), $76 \mu\text{m}$ (gold), $128 \mu\text{m}$ (green) and $145 \mu\text{m}$ (red). Fitted curves (σ and d in μm , t in ms , gravitational acceleration $g = 9.8 \mu\text{m/ms}^2$) are (a) lateral width $\sigma_Y = -46.15 + 30t$ (blue); $\sigma_Y = -20.08 + 21.4t$ (gold) and (b) vertical position: $d = -67.5 + 70t - 0.5gt^2$ before reflection and $d = -82.5 + 60(t + 8.1) - 0.5g(t + 8.1)^2$ after reflection (blue); $d = -75.7 + 65t - 0.5gt^2$ before reflection and $d = -82.5 + 60(t + 7.8) - 0.5g(t + 7.8)^2$ after reflection (gold); $d = -130 + 52t - 0.5gt^2$ (green).

No reflection is observed when the atom cloud is launched towards a region of the magnetic film without the lattice structure. The cloud disappears almost immediately when it touches the chip surface. From the above results, we conclude that the reflection is caused by the magnetic lattice potential and the ultracold atom cloud can interact with the short-range magnetic lattice potential. Further study of the reflection dynamics from a sub-micron-period magnetic lattice is needed. For example, we were not able to observe a diffraction signal from the 2D triangular magnetic lattice as Günther et al. have done for the case of a 1D current-carrying wire magnetic lattice [105, 106].

5.4 Loading a 0.7 μm -period triangular magnetic lattice: preliminary results

After demonstrating the interaction between the ultracold atom cloud and the magnetic lattice potential, we are now in a position to investigate loading of atoms into the 0.7 μm -period triangular magnetic lattice. The optimised triangular magnetic lattice potential is created with bias magnetic fields $B_x = 0.50$ G and $B_y = 4.52$ G. In our experiment configuration, the loading procedure starts from a Z-wire trap which requires a large bias field in the x -direction ($B_x \sim 50$ G). In these preliminary measurements, the Z-wire trapped ultracold cloud is transferred to the magnetic lattice traps by ramping down the Z-wire current to zero and the bias field B_x to various final values.

The lattice potential formed by the triangular lattice structure with a bias field $\{B_x, B_y = 0, B_z = 0\}$ is studied first. The created triangular lattice potential pattern is quite robust for a range of various values of B_x . Figure 5.13 (b) shows an example of a 2D contour plot for the 0.7 μm -period triangular lattice structure with $B_x = 51.8$ G. For this magnetic lattice, the traps are more elongated and tighter than for the optimised triangular lattice, Fig. 5.13 (c). For a magnetic film structure magnetised in the z -direction, the magnetisation can be modelled as a

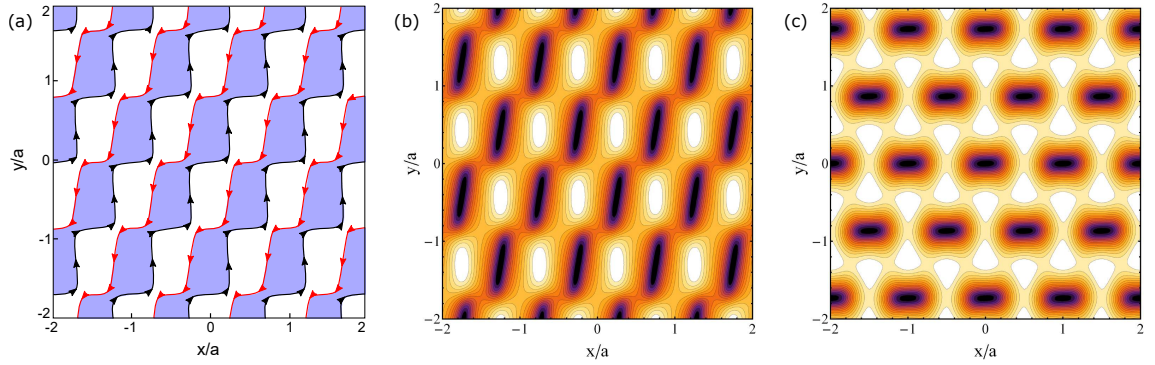


Figure 5.13: (a) The magnetic film pattern designed to create a triangular magnetic lattice optimised for a trap distance of $z = z_{min} = a/2$ from the surface of the magnetic film, where a is the lattice period. Blue regions represent the magnetic film and arrows represent virtual currents circulating around the edges of the film structure. (b) Contour plot of a triangular magnetic lattice potential with bias fields $\{B_x = 51.8 \text{ G}, B_y = 0, B_z = 0\}$; $a = 0.7 \mu\text{m}$; and $z_{min} = 132 \text{ nm}$. Dark regions are trap minima. (c) Contour plot of the optimised triangular magnetic lattice potential with bias fields $\{B_x = 0.50 \text{ G}, B_y = 4.52, B_z = 0\}$; $a = 0.7 \mu\text{m}$; and $z_{min} = a/2 = 350 \text{ nm}$. Magnetic film parameters: magnetisation $4\pi M_z = 5.9 \text{ kG}$, film thickness $t_m = 10.34 \text{ nm}$.

virtual current circulating around the edges of the patterned structure, as indicated by the arrows in Fig. 5.13 (a). A bias field B_x applied along the $+x$ -direction can cancel the magnetic field produced by the virtual current flowing along the vertical red edge to create a periodic array of elongated magnetic traps aligned along the long vertical red edges, Fig. 5.13 (b). On the other hand, a bias field B_y applied along the $+y$ -direction can cancel the magnetic field produced by the virtual current flowing along the horizontal black edge to create a periodic array of magnetic traps aligned along the short horizontal black edges, Fig. 5.13 (b). In general, a larger B_x results in a lattice trapping plane closer to the magnetic film and hence creates tighter traps with larger trap frequencies and barrier heights.

The formed magnetic lattice traps are located 132 nm from the magnetic film surface for the $B_x = 51.8 \text{ G}$ case. The distance of the lattice trap position to the chip surface $d = z_{min} - (t_{Au} + t_{SiO_2})$ becomes extremely small ($\sim 60 \text{ nm}$) when taking the 75 nm thick coating layer (gold and silica) into account. Therefore, it is important to

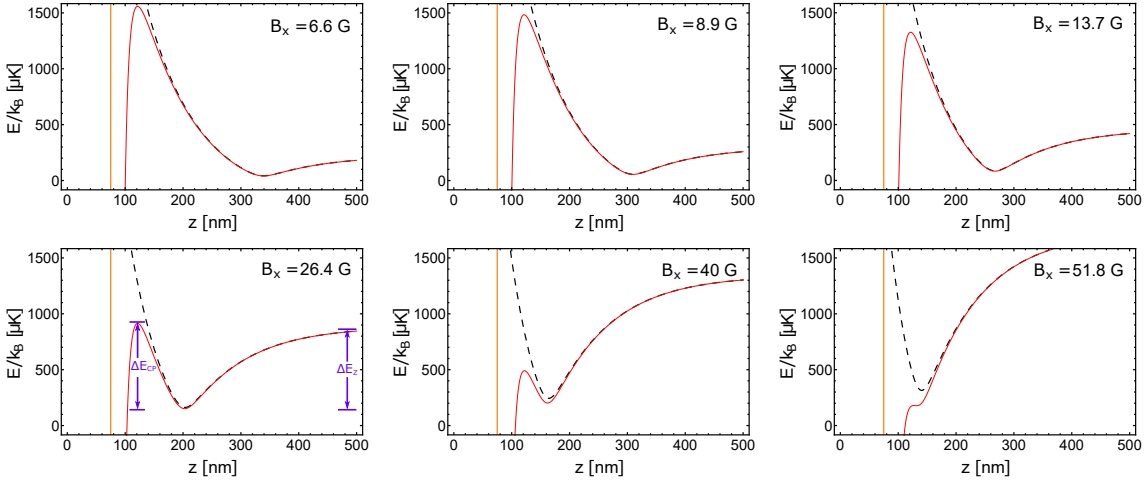


Figure 5.14: Calculated trapping potentials for ^{87}Rb $|F = 1, m_F = -1\rangle$ atoms trapped in a 0.7 μm -period triangular magnetic lattice for various values of the bias field B_x . The black dashed lines are the magnetic lattice potentials and the red solid lines include the Casimir-Polder interaction with coefficient $C_4 = 8.2 \times 10^{-56} \text{ Jm}^4$ for a silica surface. The vertical gold lines indicate the position of the silica surface ($z = 75 \text{ nm}$) used in the calculations.

study the effect of the Casimir-Polder interaction on the lattice trap potential in the z -direction for various B_x . The calculations are presented in Figure 5.14, where the Casimir-Polder coefficient is taken to be $C_4 = 8.2 \times 10^{-56} \text{ Jm}^4$ for a dielectric surface of silica film (Sect. 2.7.2). According to these calculations, the trapping potential for $B_x = 51.8 \text{ G}$ is very shallow, with the calculated trap depth $\Delta E_{CP}/k_B \sim 1.5 \mu\text{K}$. For $B_x \leq 26.4 \text{ G}$ the trap centre is located at distances $d > 130 \text{ nm}$ from the chip surface and the effect of the Casimir-Polder interaction is relatively small, so that the effective depth of the lattice traps is determined by $\Delta E_{eff} \equiv \Delta E_z$. For $B_x \geq 40 \text{ G}$, the trap distance $d < 100 \text{ nm}$ and the deformation of the lattice trap potential caused by the Casimir-Polder interaction becomes significant, so that $\Delta E_{eff} \equiv \Delta E_{CP}$. The calculated trapping parameters for different B_x are listed in Table 5.2. The calculated trap frequencies for these very tight magnetic lattice traps can be larger than 1 MHz. In order to form a meaningful trap with these extreme frequencies, the corresponding Larmor frequencies at the trap bottom B_{IP} are also required to be very high to avoid losses induced by Landau-Zener spin-flip transitions. In Table 5.2, the calculated Larmor frequency is much larger than the lattice trapping frequency

for the various bias fields B_x . Therefore, the permanent magnetic film structure can create magnetic traps with trap frequency in megahertz regime.

Table 5.2: Calculated parameters for ^{87}Rb $|F = 1, m_F = -1\rangle$ atoms trapped in the 0.7 μm -period triangular magnetic lattice including Casimir-Polder interaction, using the parameters $4\pi M_z = 5.9 \text{ kG}$, $t_m = 10.34 \text{ nm}$ and $C_4 = 8.2 \times 10^{-56} \text{ Jm}^4$. z_{min} and $d = z_{min} - 75 \text{ nm}$ are the distances of the trap minima from the magnetic film surface and the chip surface, respectively; B_{IP} is the trap bottom; ω_L is the Larmor frequency at the trap bottom; ω_{\perp} , ω_{\parallel} are the trap frequencies perpendicular to and parallel to the elongated traps; $\bar{\omega}$ is the geometric mean trap frequency; $\Delta E_{x,y}$, ΔE_z are the barrier height of the magnetic potential in the x - y plane and z -direction, respectively; and ΔE_{CP} is the barrier height due to the effect of the Casimir-Polder interaction.

Bias field B_x (G)	z_{min} (CP) (nm)	d (nm)	B_{IP} (G)	$\omega_L/2\pi$ (kHz)	$\omega_{\perp,\parallel}/2\pi$ (kHz)	$\bar{\omega}/2\pi$ (kHz)	$\Delta E_{x,y}/k_B$ (μK)	$\Delta E_z/k_B$ (μK)	$\Delta E_{CP}/k_B$ (μK)
6.6	339	264	1.2	840	530, 81	283	264, 170	181	1518
8.9	310	235	1.6	1120	616, 93	328	359, 232	244	1429
13.7	267	192	2.5	1750	769, 114	407	559, 362	377	1243
26.4	203	128	4.5	3149	1093, 153	568	1106, 730	736	763
40.0	162	87	6.0	4199	1370, 180	696	1689, 1151	1142	289
51.8	132	57	5.3	3709	887, 111	444	2297, 1588	1563	1.5

The loading stage starts with a cloud of $\sim 5 \times 10^5$ ^{87}Rb $|F = 1, m_F = -1\rangle$ atoms at $\sim 1 \mu\text{K}$ prepared in the Z-wire trap located $\sim 670 \mu\text{m}$ from the surface with $I_z = 37.6 \text{ A}$, $B_x = 51.8 \text{ G}$. The cloud is first brought to about $100 \mu\text{m}$ from the chip surface by linearly ramping down the current I_z and B_x in 100 ms. In the next step, B_x is kept constant and I_z is further ramped down, which brings the atoms closer to the surface until the Z-wire trap merges smoothly with the magnetic lattice traps located hundreds of nanometres from the chip surface. The ramping speed for I_z is optimised so that it is sufficiently slow to prevent the Z-wire trapped atoms acquiring enough momentum to penetrate the magnetic lattice potential and hit the surface and to project them onto different magnetic states but not so slow that at distances very close to the chip surface the atoms are lost by surface interactions and sloshing. Loading of the magnetic lattice is performed using a range of bias

fields $B_x = 8.9, 13.7, 26.4, 40.0$ and 51.8 G. For $B_x = 51.8$ G, there is no change in B_x and the procedure involves simply ramping down I_z . For smaller B_x , it is necessary to reduce both B_x and I_z in the first 100 ms.

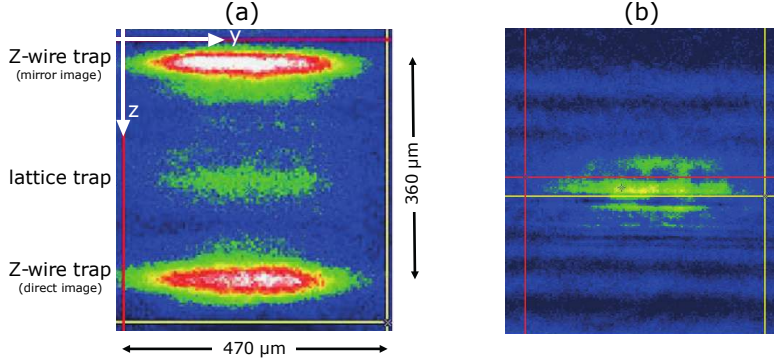


Figure 5.15: Reflection absorption images of ^{87}Rb $|F = 1, m_F = -1\rangle$ atoms (a) trapped in the $0.7 \mu\text{m}$ -period triangular magnetic lattice mid-way between the direct and mirror images of the Z-wire trapped cloud, for $B_x = 51.8$ G; (b) trapped in the $0.7 \mu\text{m}$ -period triangular magnetic lattice only, for $B_x = 13.7$ G.

A search for atoms loaded in the magnetic lattice is made by rapidly ramping up I_z again to bring the Z-wire trapped cloud further from the surface and taking an *in situ* image. A typical reflection absorption image is shown in Fig. 5.15 (a) for $B_x = 51.8$ G. The clouds at the bottom and top of the figure are the direct and mirror images of the atoms remaining in the Z-wire trap, while the smaller cloud in the middle is attributed to atoms trapped in the magnetic lattice very close to the chip surface. The direct and mirror images of the lattice trapped cloud cannot be resolved owing to their very small ($\sim 0.2 \mu\text{m}$) separation and atoms in individual lattice sites (separated by $0.7 \mu\text{m}$) are not resolved because of the limited resolution of the imaging system. Similar images of the small atom cloud trapped very close to the chip surface are observed for the other values of the bias field B_x .

The small atom cloud trapped in the middle remains when the Z-wire current I_z is completely turned off (as shown in Fig. 5.15 (b) for $B_x = 13.7$ G). When I_z is quickly reduced to zero the Z-wire trapped atoms are projected vertically to hit the chip surface and are removed. The remaining atoms are only trapped in the magnetic lattice traps. We estimate from the absorption images that $\sim 2 \times 10^4$

atoms are trapped in the magnetic lattice, initially in an area of $170 \mu\text{m} \times 11 \mu\text{m}$ containing about 3000 lattice sites ($0.7 \times 0.7 \mu\text{m}^2$ per lattice site), which corresponds to $\bar{N}_{site} \approx 6$ atoms per site. The total number of trapped atoms represents a loading efficiency of about 4%.

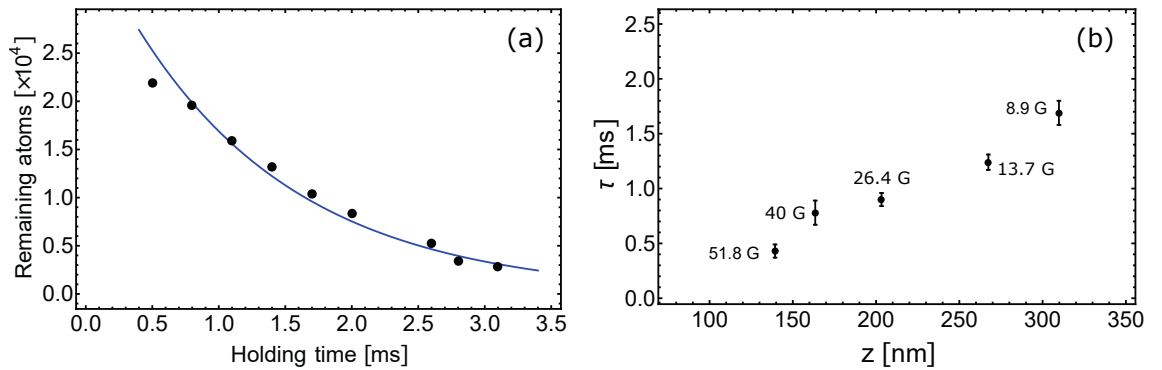


Figure 5.16: (a) Decay curve for atoms trapped in the 0.7 μm -period triangular magnetic lattice for $B_x = 13.7 \text{ G}$. The blue solid line is a single exponential fit to the data corresponding to $\tau = 1.24 \pm 0.07 \text{ ms}$. Time zero is chosen arbitrarily. (b) Measured lifetimes (black points) of atoms trapped in the magnetic lattice versus distance z of the lattice trap centre from the magnetic film surface. The B_x values (in G) are shown and the error bars are 1σ statistical uncertainties.

The lifetime of the atoms trapped in the magnetic lattice is measured by recording the number of remaining atoms versus different holding times for a range of bias fields B_x , and hence for a range of distances $z = z_{min}$ from the magnetic film surface. Figure 5.16 (a) shows a typical decay curve for $B_x = 13.7 \text{ G}$. Within our detection sensitivity, the decay curves are well fitted with a single exponential, with lifetimes varying from $0.43 \pm 0.06 \text{ ms}$ for $B_x = 51.8 \text{ G}$ to $1.69 \pm 0.11 \text{ ms}$ for $B_x = 8.9 \text{ G}$ (Table 5.4). These lifetimes are much longer than the corresponding lattice trap periods ($1\text{-}3 \mu\text{s}$), and they are found to increase approximately linearly with distance $d = z - (t_{Au} + t_{SiO_2})$ from the chip surface over the range of investigation (Fig. 5.16 (b)).

To interpret the short measured lifetimes and their approximately linear increase with distance d , we consider the following possible atom loss mechanisms:

- (1) *Adiabatic compression*. According to our previous analysis (Sect. 5.2.1), when

the ultracold atoms are transferred from the Z-wire trap to the very tight magnetic lattice traps, they are heated by adiabatic compression. The geometric mean trap frequency of the Z-wire trap is measured to be $\bar{\omega}_{Ztrap}/2\pi = 113 \text{ Hz}$ ($B_x = 51.8 \text{ G}$), 96 Hz ($B_x = 26.4 \text{ G}$) and 87 Hz ($B_x = 13.7 \text{ G}$). Because of the much larger geometric mean trap frequency of the magnetic lattice traps, Table 5.2, the compression will introduce a significant heating of the cloud, from an initial temperature $T \approx 1 \mu\text{K}$ to $\sim 3 \text{ mK}$ ($B_x = 13.7 \text{ G}$) and $\sim 4 \text{ mK}$ ($B_x = 26.4 \text{ G}$). Atoms with energies higher than the effective trap depth, $\Delta E_{eff} = \min\{\Delta E_z, \Delta E_{CP}\}$, rapidly escape the traps, resulting in a sudden truncation of the high energy tail of the Boltzmann distribution.

(2) *Surface-induced thermal evaporation.* After the sudden truncation, the remaining more energetic atoms that populate the edge of the lattice traps with energies comparable to ΔE_{eff} can rapidly overcome the trap barrier in the z -direction and become lost from the traps or spill over into neighbouring lattice traps. The escaped atoms carry away energy greater than the average energy per atom from the trap, and the remaining cloud reaches equilibrium at a lower temperature $T \approx \Delta E_{eff}/(\eta k_B)$, where η is the truncation parameter. The surface evaporation loss rate is large at the beginning of the evaporation and then gradually decreases as the evaporation proceeds.

The lifetime for surface-induced thermal evaporation is given by $\tau_{ev} = \tau_{el}/[f(\eta)e^{-\eta}]$ [55], where $\tau_{el} = [n_0\sigma_{el}\bar{v}_{rel}]^{-1}$ is the elastic collision time, and $n_0 = \frac{\bar{N}_{site}}{(2\pi)^{3/2}} \left(\frac{M}{k_B T}\right)^{3/2} \bar{\omega}^3$ is the peak atom density in the magnetic lattice traps. According to this model, τ_{ev} scales as $\Delta E_{eff}/[\bar{\omega}^3 \bar{N}_{site} \eta f(\eta) e^{-\eta}]$, where the truncation parameter η is assumed to remain constant. For decreasing $B_x \leq 26.4 \text{ G}$ (where $\Delta E_{eff} \equiv \Delta E_z$), the trap minima move away from the chip surface and $\bar{\omega}^{-3}$ increases at a faster rate than ΔE_z decreases, so that τ_{ev} exhibits an almost linear increase with increasing distance d from the chip surface. On the other hand, for increasing $B_x > 26.4 \text{ G}$ (where $\Delta E_{eff} \equiv \Delta E_{CP}$), the trap minima move very close to the chip surface and ΔE_{CP} and $\bar{\omega}^{-3}$ both decrease together with decreasing d , resulting in a sharp decrease in τ_{ev} (Table 5.2).

A reasonable fit, as shown in Fig. 5.17 (a), requires $\bar{N}_{site} \approx 2$ and $\eta \approx 4.4$. The value $\bar{N}_{site} = 2$ is smaller than the estimated initial value $\bar{N}_{site} \approx 6$ which could be due to atoms initially spilling over into neighbouring lattice sites or the initial atom number being about three times smaller than the measured value ($\sim 2 \times 10^4$). The fitted curve (red solid line) represents the measurements well for distances to the magnetic film surface z larger than 200 nm. However, the fitted curve deviates from the measurements when the lattice traps approach the surface ($z < 200$ nm). This deviation occurs at a position where the effect of the Casimir-Polder interaction starts to dominate. The calculated lifetime is very sensitive to the distance d from the chip surface at these very small distances due to the Casimir-Polder interaction.

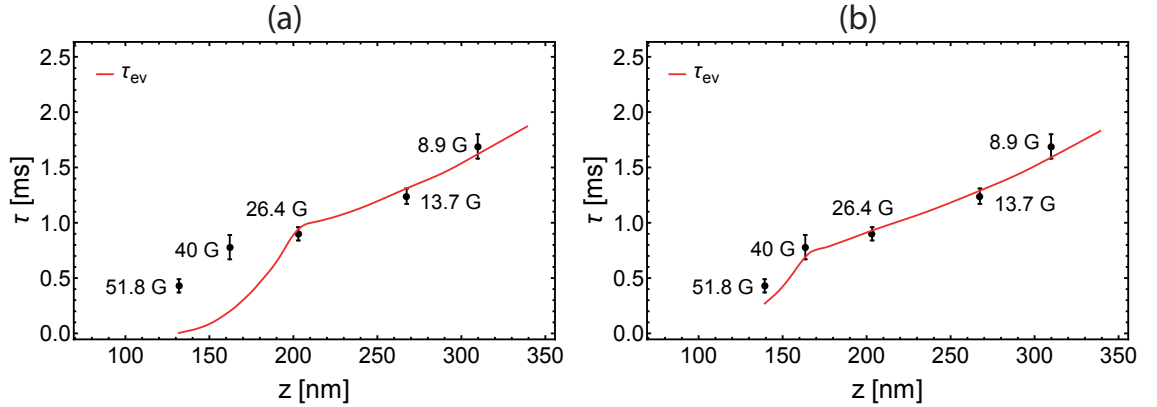


Figure 5.17: The measured lattice lifetimes are fitted with the model of surface-induced thermal evaporation. The red curve shows the calculated evaporation lifetime τ_{ev} for (a) $\bar{N}_{site} = 2$, $\eta = 4.4$ and the fixed parameters given in Table 5.2. (b) $\bar{N}_{site} = 2$, $\eta = 4.4$, offset $\delta d = 25$ nm and the fixed parameters given in Table 5.3.

To obtain a better fit at very small distance d requires either the calculated $C_4 = 8.2 \times 10^{-56} \text{Jm}^4$ to be smaller by an order of magnitude or the calculated distances of the trapped atoms from the chip surface $d = z_{min} - (t_{Au} + t_{SiO_2})$ to be larger by an offset $\delta d \approx 25$ nm. The above C_4 value is expected to be accurate to within $\sim 40\%$ based on the level of agreement between the calculated C_4 value and the measured value for a dielectric sapphire surface film [168]. An offset value of $\delta d = 25$ nm is within the estimated uncertainty (${}_{-30}^{+40}$ nm) in $d = z_{min} - (t_{Au} + t_{SiO_2})$ for $B_x = 40$ G and 51.8 G, which has a contribution from a systematic error of

about +10 nm due to the effect of the 25 nm-deep etching of the magnetic film and estimated uncertainties in $t_{\text{Au}} + t_{\text{SiO}_2}$ (± 5 nm), z_{min} (± 25 nm) and the effect of the estimated uncertainty in C_4 (± 2 nm). Introducing an offset $\delta d = 25$ nm for the distance $d = z_{\text{min}} - (t_{\text{Au}} + t_{\text{SiO}_2})$ of the lattice traps from the chip surface gives $\Delta E_{\text{CP}}/k_B = 655 \mu\text{K}$ for $B_x = 51.8$ G, as shown in Figure 5.18.

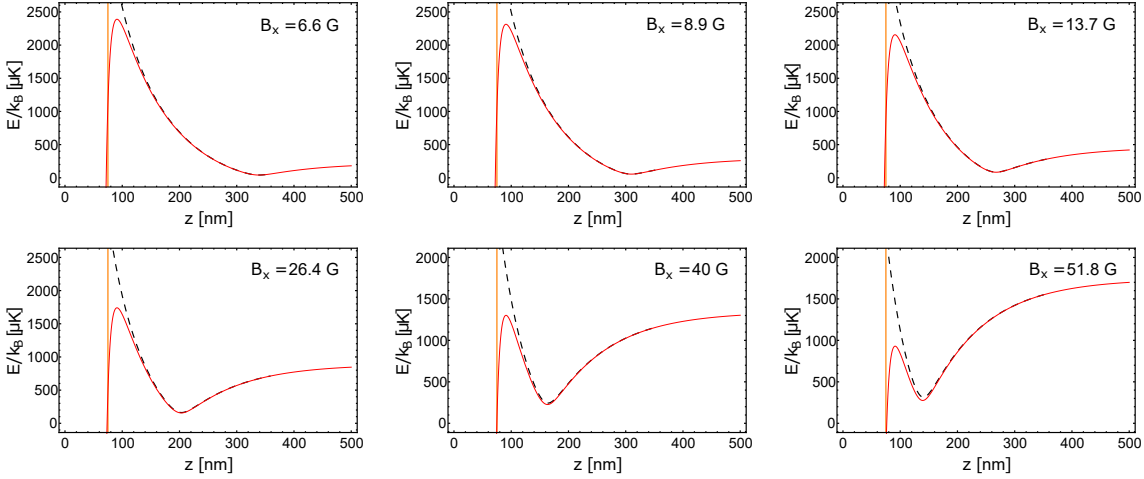


Figure 5.18: Calculated trapping potentials for ^{87}Rb $|F = 1, m_F = -1\rangle$ atoms trapped in a 0.7 μm -period triangular magnetic lattice for various values of the bias field B_x by introducing an offset $\delta d = 25$ nm.

Table 5.3: Calculated parameters for ^{87}Rb $|F = 1, m_F = -1\rangle$ atoms trapped in the 0.7 μm -period triangular magnetic lattice, for $4\pi M_z = 5.9$ kG, $t_m = 10.34$ nm, $C_4 = 8.2 \times 10^{-56}$ Jm⁴ and offset parameter $\delta d = 25$ nm. The distance of the trap minima from the chip surface is $d = z_{\text{min}} - (t_{\text{Au}} + t_{\text{SiO}_2}) + \delta d = z_{\text{min}} - 50$ nm.

Bias field B_x (G)	z_{min} (CP) (nm)	d (nm)	B_{IP} (G)	$\omega_L/2\pi$ (kHz)	$\omega_{\perp,\parallel}/2\pi$ (kHz)	$\bar{\omega}/2\pi$ (kHz)	$\Delta E_{x,y}/k_B$ (μK)	$\Delta E_z/k_B$ (μK)	$\Delta E_{\text{CP}}/k_B$ (μK)
6.6	339	289	1.2	840	532, 82	285	264, 170	181	2348
8.9	310	260	1.6	1120	618, 94	330	359, 232	244	2258
13.7	267	217	2.5	1750	772, 115	409	559, 362	376	2072
26.4	203	153	4.7	3289	1097, 153	569	1104, 729	731	1584
40.0	163	113	6.7	4689	1405, 185	715	1703, 1155	1118	1075
51.8	139	89	8.2	5738	1657, 207	828	2233, 1554	1465	655

The calculated trap parameters for different bias fields B_x with $\delta d = 25$ nm are listed in Table 5.3. Based on these calculations and with fitted parameters $\bar{N}_{\text{site}} = 2$,

$\eta = 4.4$, the calculated lifetime τ_{ev} (solid red curve) in Fig. 5.17 (b) is well fitted to the measurements. The model clearly shows the turning point ($d \approx 110$ nm from the chip surface) where the Casimir-Polder interaction becomes dominant. The atoms can be trapped as close as ~ 90 nm from the chip surface due to the extremely high trap frequency produced by the magnetic lattice.

(3) *3-body recombination.* A second possible loss process is 3-body recombination in the very tight magnetic lattice traps. This rapid loss process is expected to occur at the very beginning of the loading process before recording the atom number remaining in the lattice traps. The lifetime for (non-exponential) decay by 3-body recombination can be estimated from $\tau_{3b} = 1/(K_3 n_0^2)$, where $K_3 = 4.3(1.8) \times 10^{-29}$ cm⁶/s for non-condensed ^{87}Rb $|F = 1, m_F = -1\rangle$ atoms [113]. Thus, τ_{3b} scales as $\Delta E_{eff}^3 / [\bar{\omega}^6 \bar{N}_{site}^2 \eta^3]$. For decreasing $B_x < 40$ G (for $\delta d = 25$ nm) (or $B_x < 26.4$ G for $\delta d = 0$ nm), the trap minima move away from the chip surface and ΔE_{eff}^3 decreases at about the same rate as $\bar{\omega}^{-6}$ increases (Table 5.3 for $\delta d = 25$ nm and Table 5.2 for $\delta d = 0$ nm), so that τ_{3b} remains almost constant for distances $z > 170$ nm (for $\delta d = 25$ nm) (or $z > 210$ nm for $\delta d = 0$ nm). For increasing $B_x \geq 40$ G (for $\delta d = 25$ nm) ($B_x \geq 26.4$ G for $\delta d = 0$ nm), the trap minima move very close to the chip surface and ΔE_{eff}^3 and $\bar{\omega}^{-6}$ both decrease strongly together with decreasing z , resulting in a rapid decrease in τ_{3b} .

In Figure 5.19, we show this changing behaviour for $\bar{N}_{site} = 2$, $\eta = 4.4$. The flat shape for “lifetime” for 3-body recombination τ_{3b} versus distance is different to the observed linearly dependence of lifetime versus distance (Fig. 5.16 (b)), and therefore it is unlikely that 3-body loss is contributing to the measured lifetime. But in reality, the 3-body loss should only be suppressed for $\bar{N}_{site} = 2$ since the hopping allows some 3-body recombination for $N < 3$. An average of two atoms per lattice site over the occupied lattice is consistent with the end-product of rapid 3-body recombination prior to the final equilibration stage, leaving 0, 1 or 2 atoms on any given site. The lifetime of the lattice trap mainly depends on the relatively long exponential decay curve (Fig. 5.16 (a)) due to the surface-induced thermal evaporation loss when $\bar{N}_{site} \approx 2$ is reached.

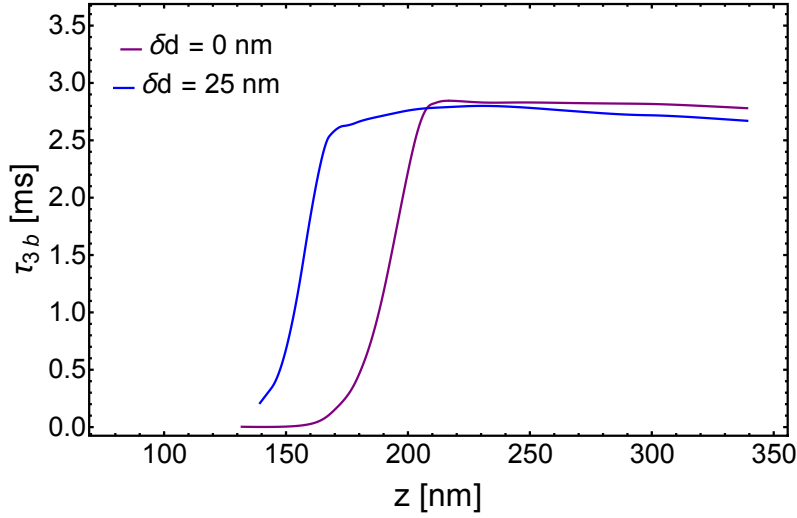


Figure 5.19: Calculated 3-body recombination lifetime τ_{3b} for $\bar{N}_{site} = 2$, $\eta = 4.4$, $\delta d = 0$ nm (purple curve) and $\bar{N}_{site} = 2$, $\eta = 4.4$, $\delta d = 25$ nm (blue curve).

Table 5.4: Measured magnetic lattice trap lifetimes τ_{exp} for a range of bias fields B_x and the calculated lifetimes for different loss processes. τ_s and τ_{ev} are the spin-flip lifetime and the lifetime for surface-induced thermal evaporation, respectively.

B_x (G)	τ_{exp} (ms)	τ_s (ms)	$\bar{N}_{site} = 2, \eta = 4.4$	
			τ_{ev} (ms) ($\delta d = 0$ nm)	τ_{ev} (ms) ($\delta d = 25$ nm)
6.6		254	1.87	1.83
8.9	1.69 ± 0.11	210	1.62	1.59
13.7	1.24 ± 0.07	150	1.31	1.29
26.4	0.90 ± 0.06	80	0.94	0.93
40	0.78 ± 0.11	50	0.20	0.69
51.8	0.43 ± 0.06	30	0.004	0.27

(4) *Spin flips due to Johnson noise.* Another possible loss process can result from spin-flips caused by Johnson magnetic noise. For $t_{Au} = 50$ nm thick gold layer on top of the magnetic film, we obtain spin-flip lifetimes that are much longer than the measured lattice trap lifetimes, for example, $\tau_s = 50$ ms and 250 ms for $d = 110$ nm and 290 nm, respectively, see Table 5.4.

The above discussion suggests that the short lifetimes (0.4 - 1.7 ms) of the atoms trapped in the $0.7\ \mu\text{m}$ -period triangular magnetic lattice at distances $d = 90 - 260\ \text{nm}$ from the chip surface are limited mainly by losses due to surface-induced thermal evaporation following transfer of atoms from the Z-wire trap to the very tight magnetic lattice traps, rather than by fundamental loss processes such as 3-body recombination or spin-flips due to Johnson magnetic noise.

5.5 Summary

The chapter described experiments on a $0.7\ \mu\text{m}$ -period triangular magnetic lattice which is a possible candidate for conducting quantum tunnelling experiments in a magnetic lattice. Since the lattice traps for a sub-micron-period magnetic lattice are normally located only a few hundred nanometres from the magnetic film surface, the atom-surface interactions were studied prior to loading atoms into the magnetic lattice traps. In the experiment, we found that the atom loss introduced by the Casimir-Polder interaction appears at about $5\ \mu\text{m}$ from surface for a condensate in a Z-wire trap. The interaction of ultracold atoms with the $0.7\ \mu\text{m}$ -period magnetic potential was then studied by the atom cloud reflection dynamics. The observation of half-moon-shaped reflected clouds is consistent with the existence of a weak sinusoidal magnetic potential pattern in the lattice plane. Finally, preliminary results for loading ^{87}Rb atoms into the $0.7\ \mu\text{m}$ -period triangular magnetic lattice were presented. The measured trap lifetimes are in the range 0.4 - 1.7 ms for bias fields $B_x = 52 - 9\ \text{G}$. To interpret these short lifetimes, possible atom loss mechanisms were discussed. Our model suggests that surface-induced thermal evaporation is the major limitation, rather than 3-body losses or spin-flips due to Johnson magnetic noise. It should be feasible to overcome surface-induced thermal evaporation losses by improving the transfer of atoms from the Z-wire trap to the very tight magnetic lattice traps, for example, by loading the atoms from a magnetic trap with higher trap frequency.

CHAPTER 6

Summary and future directions

6.1 Summary

In this thesis, I have reported the design, fabrication and testing of sub-micron period 2D magnetic lattice structures on a Co/Pd multi-atomic layer magnetic film for ultracold atom experiments. This patterned film is integrated onto a current-carrying wire atom chip to form a hybrid chip device. The original result of the thesis is the trapping of ultracold ^{87}Rb atoms in a $0.7\ \mu\text{m}$ -period triangular magnetic lattice at estimated distances down to about 100 nm from the atom chip surface and at trap frequencies as high as 800 kHz. This result represents new territory for trapping ultracold atoms.

In chapter 2 theoretical background relevant to the experiments described in this thesis was briefly introduced. This included the basic theory of magnetic trapping, runaway evaporation and the properties of Bose-Einstein condensation, and the atom-surface interactions including both Johnson noise and the attractive Casimir-Polder interaction.

Chapter 3 described the fabrication of the sub-micron period 2D magnetic lattice structures and the construction of the hybrid magnetic lattice atom chip. High quality magnetic lattice structures with a period down to $0.7\ \mu\text{m}$ were patterned on

a multi-atomic layer Co/Pd magnetic film with an optimised procedure of electron-beam lithography and reactive ion etching. It includes $0.7\ \mu\text{m}$ -period square and triangular lattices and $0.7\ \mu\text{m}$ - and $5\ \mu\text{m}$ -period 1D lattices. In addition, a current-carrying wire structure which contains four U-wires and four Z-wires was fabricated based on a direct bonded copper (DBC) substrate for the preparation of the initial ultracold cloud.

In the chapter 4 the experimental setup and the experimental procedure for routinely producing a BEC or ultracold atom cloud in a Z-wire trap were described. The Z-wire trap is usually located $\sim 670\ \mu\text{m}$ below the chip surface, where the magnetic field from the magnetic lattice structure is negligible. Time of flight measurements and RF spectroscopy were used to characterise the properties of the condensate and the ultracold thermal cloud.

In chapter 5 the interactions between the Z-wire trapped atoms and the new hybrid magnetic lattice chip surface was first studied at short distances ($\sim 1 - 20\ \mu\text{m}$) before loading the magnetic lattice traps. For distances $d > 10\ \mu\text{m}$, the measured trap lifetime is constant ($\sim 25\ \text{s}$) and independent of the distance but reduces rapidly and becomes distance-dependent when $d < 10\ \mu\text{m}$ due to the attractive Casimir-Polder interaction. This has been confirmed by measurements of the remaining atom fraction versus distance d . Next, the interaction between the ultracold atoms and the short-range magnetic potential located about $100\ \text{nm}$ from the chip surface is checked by observing the reflection dynamics. The observation of half-moon-shaped reflected clouds confirms that the magnetic potential pattern created by the triangular magnetic structure is consistent with the expected sinusoidal corrugations in the xy -plane. In the final section, the results for loading the $0.7\ \mu\text{m}$ -period triangular magnetic lattice were presented. The measured short lifetimes ($0.4\text{-}1.7\ \text{ms}$) of the lattice traps at various distances ($90\text{-}260\ \text{nm}$) from the chip surface is fitted well by a surface-induced thermal evaporation model. Our analysis suggests that the trap lifetimes are currently limited mainly by losses due to surface-induced thermal evaporation following transfer of the atoms from the Z-wire trap to the very tight magnetic lattice traps, rather than by fundamental

processes such as surface interactions, 3-body recombination or spin flips caused by Johnson magnetic noise.

6.2 Future directions

The current lifetimes (~ 1 ms) of the trapped atoms need to be increased at least one order of magnitude to enable quantum tunnelling which is typically about 10 ms (Sect. 2.6.2) for a $0.7 \mu\text{m}$ -period magnetic lattice. The surface-induced thermal evaporation is the main limiting factor based on our calculations. For the same atom number per lattice site, for example $\overline{N}_{site} = 2$, the estimated evaporation lifetime τ_{ev} is determined by the temperature of the cloud which is not a fundamental limit. It should be feasible to overcome the losses by loading the atoms from a magnetic trap with higher trap frequency. Trap frequencies as high as 5 kHz [55] or even tens of kilohertz [169] have previously been achieved for a current-carrying conductor microtrap on an atom chip. This can significantly reduce the heating due to adiabatic compression. For example, if we choose $\omega_r/2\pi = 20$ kHz, $\omega_{ax}/2\pi = 20$ Hz and an optimised $0.7 \mu\text{m}$ -period triangular magnetic lattice, the resulting heating reduces from a 1000 times to 100 times. Another improvement is that the Casimir-Polder interaction can be compensated at about 400 nm (Sect. 2.7.2) with such a high trap frequency. We can expect the atom loss due to the Casimir-Polder interaction to be small during the loading process. For a condensate initially prepared at temperature $T \approx 100$ nK, the temperature can increase to $\sim 10 \mu\text{K}$ after loading lattice traps. The truncation parameter is $\eta \approx 10$ in this case since $\Delta E_z \approx 96 \mu\text{K}$ (Sect. 5.2.1). Our model suggests that the surface-induced thermal evaporation lifetime can increase to $\tau_{ev} \approx 300$ ms, which is very promising for quantum tunnelling. In order to drive the system through the quantum transition from the superfluid regime to the Mott-insulator regime, the barrier height needs to be precisely ramped over about 20 mG. This requires that the bias fields and stray DC and AC magnetic fields need to be precisely controlled to within about 1 mG. As demonstrated in chapter 3, the quality of the fabricated magnetic lattice structure is very high and the imperfections

in the periodicity are about 1%. The kind of effects this can introduce to quantum tunnelling requires further studies. In conclusion, quantum tunnelling should be possible in a $0.7\ \mu\text{m}$ -period magnetic lattice without fundamental limitations although it will be experimentally very challenging.

Recently, a proposal to simulate lattice spin models based on long-range interacting Rydberg atoms trapped in a magnetic lattice with large period ($\sim 3\ \mu\text{m}$) has been reported [170]. The capability to produce a large-period magnetic lattice structure is one advantage compared to the widely used optical lattices. In addition, the large periods reduce adiabatic compression heating and increase the evaporation lifetime τ_{ev} and suppress 3-body losses accordingly. A ten-times thicker magnetic film would be suitable for this experiment because it can produce enough trap barrier height for a $3\ \mu\text{m}$ -period magnetic lattice. A main concern here is that the inhomogeneous electric fields produced by the adsorbed atoms on the chip surface can perturb the nearby Rydberg atoms [171]. This perturbation should be very small when atoms are prepared in nS Rydberg states due to their small differential electric polarisability [170]. The Amsterdam group has demonstrated loading ^{87}Rb $|F = 2, m_F = +2\rangle$ atoms into a $10\ \mu\text{m}$ -period 2D magnetic lattice with a lifetime of about 1 s [118]. Longer lattice trap lifetimes are expected for ^{87}Rb $|F = 1, m_F = -1\rangle$ atoms which have a smaller 3-body recombination rate [113, 114]. This is another promising research direction for the future.

Bibliography

- [1] S. Bose. *Z. Phys.*, 26:178, 1924. (Cited on page 2.)
- [2] A. Einstein. *Sitzungsber. Preuss. Akad. Wiss.*, 2:61, 1924. (Cited on page 2.)
- [3] A. Einstein. *Sitzungsber. Preuss. Akad. Wiss.*, 3:18, 1925. (Cited on page 2.)
- [4] L. N. Cooper. Bound electron pairs in a degenerate fermi gas. *Phys. Rev.*, 104:1189, 1956. (Cited on page 2.)
- [5] J. Bardeen, L. N. Cooper, and J. R. Schrieffer. Microscopic theory of superconductivity. *Phys. Rev.*, 106:162, 1957. (Cited on page 2.)
- [6] J. Bardeen, L. N. Cooper, and J. R. Schrieffer. Theory of superconductivity. *Phys. Rev.*, 108:1175, 1957. (Cited on page 2.)
- [7] S. Chu. The manipulation of neutral particles. *Rev. Mod. Phys.*, 70:685, 1998. (Cited on page 2.)
- [8] C. N. Cohen-Tannoudji. Manipulating atoms with photons. *Rev. Mod. Phys.*, 70:707, 1998. (Cited on page 2.)
- [9] W. D. Phillips. Laser cooling and trapping of neutral atoms. *Rev. Mod. Phys.*, 70:721, 1998. (Cited on page 2.)
- [10] M. H. Anderson, J. R. Ensher, M. R. Matthews, C. E. Wieman, and E. A. Cornell. Observation of Bose-Einstein condensation in a dilute atomic vapor. *Science*, 269:198–201, 1995. (Cited on page 2.)

-
- [11] K. B. Davis, M. -O. Mewes, M. R. Andrews, N. J. van Druten, D. S. Durfee, D. M. Kurn, and W. Ketterle. Bose-Einstein condensation in a gas of sodium atoms. *Phys. Rev. Lett.*, 75:3969, 1995. (Cited on page 2.)
- [12] C. C. Bradley, C. A. Sackett, J. J. Tollett, and R. G. Hulet. Evidence of Bose-Einstein condensation in an atomic gas with attractive interactions. *Phys. Rev. Lett.*, 75:1687, 1995. (Cited on page 2.)
- [13] I. Bloch. Ultracold quantum gases in optical lattices. *Nature Physics*, 1:23, 2005. (Cited on pages 3 and 24.)
- [14] I. Bloch, J. Dalibard, and W. Zwerger. Many-body physics with ultracold gases. *Rev. Mod. Phys.*, 80:885, 2008. (Cited on pages 3, 24, and 25.)
- [15] M. Greiner, O. Mandel, T. Esslinger, T. W. Hänsch, and I. Bloch. Quantum phase transition from a superfluid to a Mott insulator in a gas of ultracold atoms. *Nature*, 415:39, 2002. (Cited on pages 3 and 25.)
- [16] M. P. A. Fisher, P. B. Weichman, G. Grinstein, and D. S. Fisher. Boson localization and the superfluid-insulator transition. *Phys. Rev. B*, 40:546, 1989. (Cited on pages 3 and 24.)
- [17] T. Stöferle, H. Moritz, C. Schori, M. Köhl, and T. Esslinger. Transition from a strongly interacting 1D superfluid to a Mott insulator. *Phys. Rev. Lett.*, 92:130403, 2006. (Cited on page 3.)
- [18] I. B. Spielman, W. D. Phillips, and J. V. Porto. Mott-insulator transition in a two-dimensional atomic bose gas. *Phys. Rev. Lett.*, 98:080404, 2007. (Cited on pages 3, 24, and 25.)
- [19] W. S. Bakr, J. I. Gillen, A. Peng, S. Fölling, and M. Greiner. A quantum gas microscope for detecting single atoms in a Hubbard-regime optical lattice. *Nature*, 462:74, 2009. (Cited on page 3.)

- [20] J. F. Sherson, C. Weitenberg, M. Endres, M. Cheneau, I. Bloch, and S. Kuhr. Single-atom-resolved fluorescence imaging of an atomic Mott insulator. *Nature*, 467:68, 2010. (Cited on page 3.)
- [21] R. Jördens, N. Strohmaier, K. Günter, H. Moritz, and T. Esslinger. A Mott Insulator of Fermionic Atoms in an Optical Lattice. *Nature*, 455:204, 2008. (Cited on page 3.)
- [22] U. Schneider, L. Hackermüller, S. Will, Th. Best, I. Bloch, T. A. Costi, R. W. Helmes, D. Rasch, and A. Rosch. Metallic and Insulating Phases of Repulsively Interacting Fermions in a 3D Optical Lattice. *Science*, 322:1520, 2008. (Cited on page 3.)
- [23] B. DeMarco and D. S. Jin. Onset of Fermi degeneracy in a trapped atomic gas. *Science*, 285:1703, 1999. (Cited on page 3.)
- [24] A. G. Truscott, K. E. Strecker, W. I. McAlexander, G. B. Partridge, and R. G. Hulet. Observation of Fermi pressure in a gas of trapped atoms. *Science*, 291:2570, 2001. (Cited on page 3.)
- [25] C. Chin, R. Grimm, P. Julienne, and E. Tiesinga. Feshbach resonances in ultracold gases. *Rev. Mod. Phys.*, 82:1225, 2010. (Cited on pages 3 and 24.)
- [26] C. A. R. Sá de Melo, M. Randeria, and J. R. Engelbrecht. Crossover from BCS to Bose superconductivity: Transition temperature and time-dependent Ginzburg-Landau theory. *Phys. Rev. Lett.*, 71:3202, 1993. (Cited on page 4.)
- [27] Y.-J. Lin, R. L. Compton, K. Jiménez-García, J. V. Porto, and I. B. Spielman. Synthetic magnetic fields for ultracold neutral atoms. *Nature*, 462:628, 2009. (Cited on page 4.)
- [28] J. Dalibard, F. Gerbier, G. Juzeliūnas, and P. Öhberg. Colloquium: Artificial gauge potentials for neutral atoms. *Rev. Mod. Phys.*, 83:1523, 2011. (Cited on page 4.)

-
- [29] J. Reichel. Microchip traps and Bose-Einstein condensation. *Appl. Phys. B*, 75:469, 2002. (Cited on pages 4, 13, 14, 16, and 64.)
- [30] R. Folman, P. Krüger, J. Schmiedmayer, J. Denschlag, and C. Henkel. Microscopic atom optics: From wires to an atom chip. *Advances in Atomic, Molecular, and Optical Physics*, 48:263–356, 2002. (Cited on pages 4, 13, and 14.)
- [31] J. Fortágh and C. Zimmermann. Magnetic microtraps for ultracold atoms. *Rev. Mod. Phys.*, 79:235, 2007. (Cited on page 4.)
- [32] M. Keil, O. Amit, S. Zhou, D. Groswasser, Y. Japha, and R. Folman. Fifteen years of cold matter on the atom chip: promise, realizations, and prospects. *Journal of Modern Optics*, 63:1840, 2016. (Cited on page 4.)
- [33] R. Folman, P. Krüger, D. Cassettari, B. Hessmo, T. Maier, and J. Schmiedmayer. Controlling cold atoms using nanofabricated surfaces: Atom chips. *Phys. Rev. Lett.*, 84:4749, 2000. (Cited on pages 4 and 5.)
- [34] R. Folman, J. Schmiedmayer and T. Calarco. Quantum Information Processing with Neutral Atoms on an Atom Chip. *J. Mod. Opt.*, 49:1375, 2002. (Cited on page 4.)
- [35] J. D. Weinstein and K. G. Libbrecht. Microscopic magnetic traps for neutral atoms. *Phys. Rev. A*, 52:4004, 1995. (Cited on page 4.)
- [36] J. Denschlag, D. Cassettari, and J. Schmiedmayer. Guiding neutral atoms with a wire. *Phys. Rev. Lett.*, 82:2014, 1999. (Cited on page 4.)
- [37] D. Müller, D. Z. Anderson, R. J. Grow, P. D. D. Schwindt, and E. A. Cornell. Guiding neutral atoms around curves with lithographically patterned current-carrying wires. *Phys. Rev. Lett.*, 83:5194, 1999. (Cited on page 4.)
- [38] N. H. Dekker, C. S. Lee, V. Lorent, J. H. Thywissen, S. P. Smith, M. Drndić, R. M. Westervelt, and M. Prentiss. Guiding neutral atoms on a chip. *Phys. Rev. Lett.*, 84:1124, 2000. (Cited on page 4.)

-
- [39] D. Cassetari, B. Hessmo, R. Folman, T. Maier, and J. Schmiedmayer. Beam splitter for guided atoms. *Phys. Rev. Lett.*, 85:5483, 2000. (Cited on page 4.)
- [40] J. Reichel, W. Hänsel, and T. W. Hänsch. Atomic micromanipulation with magnetic surface traps. *Phys. Rev. Lett.*, 83:3398, 1999. (Cited on pages 5 and 16.)
- [41] H. Ott, J. Fortagh, G. Schlotterbeck, A. Grossmann, and C. Zimmermann. Bose-Einstein condensation in a surface microtrap. *Phys. Rev. Lett.*, 87:230401, 2001. (Cited on page 5.)
- [42] T. L. Gustavson, A. P. Chikkatur, A. E. Leanhardt, A. Görlitz, S. Gupta, D. E. Pritchard, and W. Ketterle. Transport of Bose-Einstein condensates with optical tweezers. *Phys. Rev. Lett.*, 88:020401, 2001. (Cited on page 5.)
- [43] W. Hänsel, P. Hommelhoff, T. W. Hänsch, and J. Reichel. Bose-Einstein condensation on a microelectronic chip. *Nature*, 413:498–501, 2001. (Cited on page 5.)
- [44] S. Aubin, S. Myrskog, M. H. T. Extavour, L. J. LeBlanc, D. McKay, A. Stummer, and J. H. Thywissen. Rapid sympathetic cooling to Fermi degeneracy on a chip. *Nature Physics*, 2:384, 2006. (Cited on page 5.)
- [45] A. Tauschinsky, R. M. T. Thijssen, S. Whitlock, H. B. van Linden van den Heuvell, and R. J. C. Spreeuw. Spatially resolved excitation of Rydberg atoms and surface effects on an atom chip. *Phys. Rev. A*, 81:063411, 2010. (Cited on page 5.)
- [46] C. H.-Avigliano, R. C. Teixeira, T. L. Nguyen, T. C.-Molrecht, G. Nogues, I. Dotsenko, S. Gleyzes, J. M. Raimond, S. Haroche, and M. Brune. Long coherence times for Rydberg qubits on a superconducting atom chip. *Phys. Rev. A*, 90:040502(R), 2014. (Cited on page 5.)

-
- [47] S. A. Meek, H. L. Bethlem, H. Conrad, and G. Meijer. Trapping molecules on a chip in traveling potential wells. *Phys. Rev. Lett.*, 100:153003, 2008. (Cited on page 5.)
- [48] Samuel A. Meek, Horst Conrad, and Gerard Meijer. Trapping molecules on a chip. *Science*, 324:1699, 2009. (Cited on page 5.)
- [49] J. Esteve, J.-B. Trebbia, T. Schumm, A. Aspect, C. I. Westbrook, and I. Bouchoule. Observations of density fluctuations in an elongated Bose gas: Ideal gas and quasicondensate regimes. *Phys. Rev. Lett.*, 96:130403, 2006. (Cited on page 5.)
- [50] S. Hofferberth, I. Lesanovsky, B. Fischer, T. Schumm, and J. Schmiedmayer. Non-equilibrium coherence dynamics in one-dimensional bose gases. *Nature*, 449:324, 2007. (Cited on page 5.)
- [51] A. H. van Amerongen, J. J. P. van Es, P. Wicke, K. V. Kheruntsyan, and N. J. van Druten. Yang-yang thermodynamics on an atom chip. *Phys. Rev. Lett.*, 100:090402, 2008. (Cited on page 5.)
- [52] B. Yuen, I. J. M. Barr, J. P. Cotter, E. Butler and E. A. Hinds. Enhanced oscillation lifetime of a Bose-Einstein condensate in the 3D/1D crossover. *New J. Phys.*, 17:093041, 2015. (Cited on page 5.)
- [53] M. Takahashi. Thermodynamics of One-Dimensional Solvable Models. *Cambridge University Press*, 1999. (Cited on page 5.)
- [54] E. H. Lieb and W. Liniger. Exact analysis of an interacting Bose gas. I. the general solution and the ground state. *Phys. Rev.*, 130:1605, 1963. (Cited on page 5.)
- [55] Y. Lin, I. Teper, C. Chin, and V. Vuletić. Impact of the Casimir-Polder potential and Johnson noise on Bose-Einstein condensate stability near surfaces. *Phys. Rev. Lett.*, 92:050404, 2004. (Cited on pages 5, 28, 87, 104, and 113.)

-
- [56] D. M. Harber, J. M. Obrecht, J. M. McGuirk, and E. A. Cornell. Measurement of the Casimir-Polder force through center-of-mass oscillations of a Bose-Einstein condensate. *Phys. Rev. A.*, 72:033610, 2005. (Cited on page 5.)
- [57] J. M. Obrecht, R. J. Wild, M. Antezza, L. P. Pitaevskii, S. Stringari, and E. A. Cornell. Measurement of the temperature dependence of the Casimir-Polder force. *Phys. Rev. Lett.*, 98:063201, 2007. (Cited on page 5.)
- [58] M. P. A. Jones, C. J. Vale, D. Sahagun, B. V. Hall, and E. A. Hinds. Spin coupling between cold atoms and the thermal fluctuations of a metal surface. *Phys. Rev. Lett.*, 91:080401, 2003. (Cited on page 5.)
- [59] S. Aigner, L. D. Pietra, Y. Japha, O. E.-Wohlman, T. David, R. Salem, R. Folman, and J. Schmiedmayer. Long-range order in electronic transport through disordered metal films. *Science*, 319:1226, 2008. (Cited on page 5.)
- [60] S. Wildermuth, S. Hofferberth, I. Lesanovsky, E. Haller, L. M. Andersson, S. Groth, I. Bar-Joseph, P. Krüger, and J. Schmiedmayer. Bose-Einstein condensates: Microscopic magnetic-field imaging. *Nature*, 435:440, 2005. (Cited on page 5.)
- [61] S. Wildermuth, S. Hofferberth, I. Lesanovsky, S. Groth, P. Krüger, J. Schmiedmayer, and I. Bar-Joseph. Bose-Einstein condensates: Microscopic magnetic-field imaging. *Appl. Phys. Lett.*, 88:264103, 2006. (Cited on page 5.)
- [62] P. Böhi, M. F. Riedel, T. W. Hänsch, and P. Treutlein. Imaging of microwave fields using ultracold atoms. *Appl. Phys. Lett.*, 97:051101, 2010. (Cited on page 5.)
- [63] C. F. Ockeloen, R. Schmied, M. F. Riedel, and P. Treutlein. Quantum metrology with a scanning probe atom interferometer. *Phys. Rev. Lett.*, 111:143001, 2013. (Cited on page 5.)
- [64] Y. Wang, D. Z. Anderson, V. M. Bright, E. A. Cornell, Q. Diot, T. Kishimoto, M. Prentiss, R. A. Saravanan, S. R. Segal, and S. Wu. Atom Michelson

- interferometer on a chip using a Bose-Einstein condensate. *Phys. Rev. Lett.*, 94:090405, 2005. (Cited on page 5.)
- [65] E. A. Hinds, C. J. Vale, and M. G. Boshier. Two-wire waveguide and interferometer for cold atoms. *Phys. Rev. Lett.*, 86:1462, 2001. (Cited on page 6.)
- [66] Y. Shin, C. Sanner, G.-B. Jo, T. A. Pasquini, M. Saba, W. Ketterle, D. E. Pritchard, M. Vengalattore, and M. Prentiss. Interference of Bose-Einstein condensates split with an atom chip. *Phys. Rev. A.*, 72:021604(R), 2005. (Cited on page 6.)
- [67] T. Schumm, S. Hofferberth, L. M. Andersson, S. Wildermuth, S. Groth, I. Bar-Joseph, J. Schmiedmayer, and P. Krüger. Matter-wave interferometry in a double well on an atom chip. *Nature Physics*, 1:57, 2005. (Cited on page 6.)
- [68] T. Berrada, S. van Frank, R. Bücker, T. Schumm, J.-F. Schaff, and J. Schmiedmayer. Integrated Mach-Zehnder interferometer for Bose-Einstein condensates. *Nature Communications*, 4:2077, 2013. (Cited on page 6.)
- [69] T. Berrada, S. van Frank, R. Bücker, T. Schumm, J.-F. Schaff, J. Schmiedmayer, B. Juliá-Díaz, and A. Polls. Matter-wave recombiners for trapped Bose-Einstein condensates. *Phys. Rev. A*, 93:063620, 2016. (Cited on page 6.)
- [70] T. Calarco, E. A. Hinds, D. Jaksch, J. Schmiedmayer, J. I. Cirac, and P. Zoller. Quantum gates with neutral atoms: Controlling collisional interactions in time-dependent traps. *Phys. Rev. A*, 61:022304, 2000. (Cited on page 6.)
- [71] P. Treutlein, T. W. Hänsch, J. Reichel, A. Negretti, M. A. Cirone, and T. Calarco. Microwave potentials and optimal control for robust quantum gates on an atom chip. *Phys. Rev. A*, 74:022312, 2006. (Cited on page 6.)
- [72] P. Treutlein, P. Hommelhoff, T. Steinmetz, T. W. Hänsch, and J. Reichel. Coherence in microchip traps. *Phys. Rev. Lett.*, 92:203005, 2005. (Cited on page 6.)

- [73] C. Deutsch, F. Ramirez-Martinez, C. Lacroûte, F. Reinhard, T. Schneider, J. N. Fuchs, F. Piéchon, F. Laloë, J. Reichel, and P. Rosenbusch. Spin self-rephasing and very long coherence times in a trapped atomic ensemble. *Phys. Rev. Lett.*, 105:020401, 2010. (Cited on page 6.)
- [74] P. Böhi, M. F. Riedel, J. Hoffrogge, J. Reichel, T. W. Hänsch, and P. Treutlein. Coherent manipulation of Bose-Einstein condensates with state-dependent microwave potentials on an atom chip. *Nature Physics*, 5:592, 2009. (Cited on page 6.)
- [75] M. F. Riedel, P. Böhi, Y. Li, T. W. Hänsch, A. Sinatra, and P. Treutlein. Atom-chip-based generation of entanglement for quantum metrology. *Nature*, 464:1170, 2010. (Cited on page 6.)
- [76] R. Szmuk, V. Dugrain, W. Maineult, J. Reichel, and P. Rosenbusch. Stability of a trapped-atom clock on a chip. *Phys. Rev. A*, 92:012106, 2015. (Cited on page 6.)
- [77] Y. Colombe, T. Steinmetz, G. Dubois, F. Linke, D. Hunger, and J. Reichel. Strong atom-field coupling for Bose-Einstein condensates in an optical cavity on a chip. *Nature*, 450:272, 2007. (Cited on page 6.)
- [78] R. Gehr, J. Volz, G. Dubois, T. Steinmetz, Y. Colombe, B. L. Lev, R. Long, J. Estève, and J. Reichel. Cavity-based single atom preparation and high-fidelity hyperfine state readout. *Phys. Rev. Lett.*, 104:203602, 2010. (Cited on page 6.)
- [79] J. Volz, R. Gehr, G. Dubois, J. Estève, and J. Reichel. Measurement of the internal state of a single atom without energy exchange. *Nature*, 475:210, 2011. (Cited on page 6.)
- [80] M. Trinker, S. Groth, S. Haslinger, S. Manz, T. Betz, S. Schneider, I. Bar-Joseph, T. Schumm, and J. Schmiedmayer. Multilayer atom chips for versatile atom micromanipulation. *Appl. Phys. Lett.*, 92:254102, 2008. (Cited on page 6.)

- [81] T. Nirrengarten, A. Qarry, C. Roux, A. Emmert, G. Nogues, M. Brune, J.-M. Raimond, and S. Haroche. Realization of a superconducting atom chip. *Phys. Rev. Lett.*, 97:200405, 2006. (Cited on page 6.)
- [82] T. Mukai, C. Hufnagel, A. Kasper, T. Meno, A. Tsukada, K. Semba, and F. Shimizu. Persistent supercurrent atom chip. *Phys. Rev. Lett.*, 98:260407, 2007. (Cited on page 6.)
- [83] M. Kohonen, M. Succo, P. G. Petrov, R. A. Nyman, M. Trupke, and E. A. Hinds. An array of integrated atom-photon junctions. *Nature Photonics*, 5:35, 2011. (Cited on page 6.)
- [84] G. I. Opat, S. J. Wark, and A. Cimmino. Electric and magnetic mirrors and gratings for slowly moving neutral atoms and molecules. *Appl. Phys. B*, 54:396, 1992. (Cited on page 7.)
- [85] T. M. Roach, H. Abele, M. G. Boshier, H. L. Grossman, K. P. Zetie, and E. A. Hinds. Realization of a magnetic mirror for cold atoms. *Phys. Rev. Lett.*, 75:629, 1995. (Cited on page 7.)
- [86] A. I. Sidorov, R. J. McLean, W. J. Rowlands, D. C. Lau, J. E. Murphy, M. Walkiewicz, G. I. Opat, and P. Hannaford. Specular reflection of cold caesium atoms from a magnetostatic mirror. *Quantum Semiclass. Opt.*, 8:713, 1996. (Cited on page 7.)
- [87] C. V. Saba, P. A. Barton, M. G. Boshier, I. G. Hughes, P. Rosenbusch, B. E. Sauer, and E. A. Hinds. Reconstruction of a cold atom cloud by magnetic focusing. *Phys. Rev. Lett.*, 82:468, 1999. (Cited on page 7.)
- [88] D. C. Lau, R. J. McLean, A. I. Sidorov, D. S. Gough, J. Koperski, W. J. Rowlands, B. A. Sexton, G. I. Opat, and P. Hannaford. Magnetic mirrors with micron-scale periodicities for slowly moving neutral atoms. *J. Optics B: Quantum Semiclass. Opt.*, 1:371–7, 1999. (Cited on page 7.)

- [89] A. I. Sidorov, R. J. McLean, F. Scharnberg, D. S. Gough, T. J. Davis, B. A. Sexton, G. I. Opat, and P. Hannaford. Permanent magnet microstructures for atom optics. *Acta Physica Polonica B*, 33:2137–2155, 2002. (Cited on page 7.)
- [90] I. Barba, R. Gerritsma, Y. T. Xing, J. B. Goedkoop, and R. J. C. Spreeuw. Creating Ioffe-Pritchard micro-traps from permanent magnetic film with in-plane magnetization. *Eur. Phys. J. D*, 35:75, 2005. (Cited on page 7.)
- [91] C. D. J. Sinclair, J. A. Retter, E. A. Curtis, B. V. Hall, I. Llorente Garcia, S. Eriksson, B. E. Sauer, and E. A. Hinds. Cold atoms in videotape micro-traps. *Eur. Phys. J. D*, 35:105, 2005. (Cited on page 7.)
- [92] C. D. J. Sinclair, E. A. Curtis, I. Llorente Garcia, J. A. Retter, B. V. Hall, S. Eriksson, B. E. Sauer, and E. A. Hinds. Bose-Einstein condensation on a permanent-magnet atom chip. *Phys. Rev. A*, 72:031603(R), 2005. (Cited on page 7.)
- [93] B. V. Hall, S. Whitlock, F. Scharnberg, P. Hannaford, and A. Sidorov. A permanent magnetic film atom chip for Bose-Einstein condensation. *J. Phys. B: At. Mol. Opt. Phys.*, 39:27, 2006. (Cited on pages 7 and 45.)
- [94] T. Fernholz, R. Gerritsma, S. Whitlock, I. Barb, and R. J. C. Spreeuw. Fully permanent magnet atom chip for Bose-Einstein condensation. *Phys. Rev. A*, 77:033409, 2008. (Cited on pages 7 and 30.)
- [95] S. Jose, P. Surendran, Y. Wang, I. Herrera, L. Krzemien, S. Whitlock, R. McLean, A. Sidorov, and P. Hannaford. Periodic array of Bose-Einstein condensates in a magnetic lattice. *Phys. Rev. A*, 89:051602(R), 2014. (Cited on pages 7, 9, and 30.)
- [96] P. Surendran, S. Jose, Y. Wang, I. Herrera, H. Hu, X. Liu, S. Whitlock, R. McLean, A. Sidorov, and P. Hannaford. Radio-frequency spectroscopy of a linear array of Bose-Einstein condensates in a magnetic lattice. *Phys. Rev. A*, 91:023605, 2015. (Cited on pages 7, 9, and 30.)

- [97] J. Yin, W. Gao, J. Hu, and Y. Wang. Magnetic surface microtraps for realizing an array of alkali atomic Bose-Einstein condensates or Bose clusters. *Opt Commun*, 206:99–113, 2002. (Cited on pages 7 and 30.)
- [98] A. Grabowski and T. Pfau. A lattice of magneto-optical and magnetic traps for cold atoms. *Eur Phys J D*, 22:347–354, 2003. (Cited on pages 7 and 30.)
- [99] M. Yun and J. Yin. Practical scheme to realize 2D array of BECs on an atom chip: novel 2D magneto-optical and magnetic lattices. *Opt Express*, 14:2539–2551, 2006. (Cited on pages 7 and 30.)
- [100] O. Romero-Isart, C. Navau, A. Sanchez, P. Zoller, and J. I. Cirac. Superconducting vortex lattices for ultracold atoms. *Phys. Rev. Lett*, 111:145304, 2013. (Cited on pages 7 and 30.)
- [101] X. Luo, L. Wu, J. Chen, R. Lu, R. Wang, and L. You. Generating an effective magnetic lattice for ultracold atoms. *New J Phys*, 17:083048, 2015. (Cited on pages 7 and 30.)
- [102] G. A. Sinuco-León and B. M. Garraway. Radio-frequency dressed lattices for ultracold alkali atoms. *New J. Phys.*, 17:053037, 2015. (Cited on page 7.)
- [103] I. L. García, B. Darquié, E. A. Curtis, C. D. J. Sinclair, and E. A. Hinds. Experiments on a videotape atom chip: Fragmentation and transport studies. *New J. Phys.*, 12:093017, 2010. (Cited on page 8.)
- [104] M. Boyd, E. W. Streed, P. Medley, G. K. Campbell, J. Mun, W. Ketterle, and D. E. Pritchard. Atom trapping with a thin magnetic film. *Phys. Rev. A*, 76:043624, 2007. (Cited on page 8.)
- [105] A. Günther, S. Kraft, M. Kemmler, D. Koelle, R. Kleiner, C. Zimmermann, and J. Fortágh. Diffraction of a Bose-Einstein condensate from a magnetic lattice on a microchip. *Phys. Rev. Lett.*, 95:170405, 2005. (Cited on pages 8, 30, and 98.)

- [106] A. Günther, S. Kraft, C. Zimmermann, and J. Fortágh. Atom interferometer based on phase coherent splitting of Bose-Einstein condensates with an integrated magnetic grating. *Phys. Rev. Lett.*, 98:140403, 2007. (Cited on pages 8 and 98.)
- [107] M. Singh, M. Volk, A. Akulshin, A. Sidorov, R. McLean, and P. Hannaford. One dimensional lattice of permanent magnetic microtraps for ultracold atoms on an atom chip. *J. Phys. B: At. Mol. Opt. Phys.*, 41:065301, 2008. (Cited on page 8.)
- [108] M. Singh, R. McLean, A. Sidorov, and P. Hannaford. Dynamics of reflection of ultracold atoms from a periodic one-dimensional magnetic lattice potential. *Phys. Rev. A*, 79:053407, 2009. (Cited on pages 8 and 94.)
- [109] M. Singh and P. Hannaford. Effect of projection velocity and temperature on the reflection of ultracold atoms from a periodic one-dimensional corrugated magnetic potential. *Phys. Rev. A*, 82:013416, 2010. (Cited on pages 8 and 94.)
- [110] R. Gerritsma, S. Whitlock, T. Fernholz, H. Schlatter, J. A. Luigjes, J.-U. Thiele, J. B. Goedkoop, and R. J. C. Spreeuw. Lattice of microtraps for ultracold atoms based on patterned magnetic films. *Phys. Rev. A*, 76:033408, 2007. (Cited on page 8.)
- [111] S. Whitlock, R. Gerritsma, T. Fernholz, and R. J. C. Spreeuw. Two-dimensional array of microtraps with atomic shift register on a chip. *New J Phys*, 11:023021, 2009. (Cited on page 8.)
- [112] S. Whitlock, C. F. Ockeloen, and R. J. C. Spreeuw. Sub-poissonian atom-number fluctuations by three-body loss in mesoscopic ensembles. *Phys. Rev. Lett.*, 104:120402, 2010. (Cited on page 8.)
- [113] E. A. Burt, R. W. Ghrist, C. J. Myatt, M. J. Holland, E. A. Cornell, and C. E. Wieman. Coherence, correlations, and collisions: What one learns about

- Bose-Einstein condensates from their decay. *Phys. Rev. Lett.*, 79:337, 1997. (Cited on pages 8, 65, 107, and 114.)
- [114] J. Söding, D. Guéry-Odelin, P. Desbiolles, F. Chevy, H. Inamori, and J. Dalibard. Three-body decay of a rubidium Bose-Einstein condensate. *Appl. Phys. B*, 69:257, 1999. (Cited on pages 8, 65, and 114.)
- [115] S. Ghanbari, T. D. Kieu, A. Sidorov, and P. Hannaford. Permanent magnetic lattices for ultracold atoms and quantum degenerate gases. *J Phys B*, 39:847–890, 2006. (Cited on pages 9 and 41.)
- [116] S. Ghanbari, T. D. Kieu, and P. Hannaford. A class of permanent magnetic lattices for ultracold atoms. *J Phys B*, 40:1283–1294, 2007. (Cited on page 9.)
- [117] R. Schmied, D. Leibfried, R. J. C. Spreeuw, and S. Whitlock. Optimized magnetic lattices for ultracold atomic ensembles. *New J Phys*, 12:103029, 2010. (Cited on pages 9, 30, 31, 32, and 45.)
- [118] V. Y. F. Leung, D. R. M. Pijn, H. Schlatter, L. Torralbo-Campo, A. L. La Rooij, G. B. Mulder, J. Naber, M. L. Soudijn, A. Tauschinsky, C. Abarbanel, B. Hadad, E. Golan, R. Folman, and R. J. C. Spreeuw. Magnetic-film atom chip with $10 \mu\text{m}$ period lattices of microtraps for quantum information science with Rydberg atoms. *Rev. Sci. Instrum.*, 85:053102, 2014. (Cited on pages 9 and 114.)
- [119] I. Herrera, Y. Wang, P. Michaux, D. Nissen, P. Surendran, S. Juodkazis, S. Whitlock, R. J. McLean, A. Sidorov, M. Albrecht, and P. Hannaford. Sub-micron period lattice structures of magnetic microtraps for ultracold atoms on an atom chip. *J Phys D*, 48:115002, 2015. (Cited on pages 9, 36, 38, 42, and 44.)
- [120] W. Ketterle, D. S. Durfee, and D. M. Stamper-Kurn. Making, probing and understanding Bose-Einstein condensates. *Proceedings of the International School of Physics "Enrico Fermi", Course CXL, edited by M. Inguscio, S.*

- Stringari, and C. E. Wieman*, pages 67–176, 1999. (Cited on pages 11, 58, and 59.)
- [121] J. D. Jackson . Classical Electrodynamics. *Wiley*, 1998. (Cited on page 12.)
- [122] W. Ketterle, D. E. Pritchard. Trapping and focusing ground state atoms with static fields. *Appl. Phys. B*, 54:403, 1992. (Cited on page 12.)
- [123] E. Majorana. Atomi orientati in campo magnetico variabile. *Nuovo Cimento*, 9:43, 1932. (Cited on page 12.)
- [124] E. L. Raab, M. Prentiss, A. Cable, S. Chu, and D. E. Pritchard. Trapping of neutral sodium atoms with radiation pressure. *Phys. Rev. Lett.*, 59:2631, 1987. (Cited on page 16.)
- [125] Wolfgang Ketterle and N.J. Van Druten. Evaporative cooling of trapped atoms. *Advances in Atomic, Molecular, and Optical Physics*, 37:181236, 1996. (Cited on pages 18, 19, 20, and 21.)
- [126] O. J. Luiten, M. W. Reynolds, and J. T. M. Walraven. Kinetic theory of the evaporative cooling of a trapped gas. *Phys. Rev. A*, 53:381, 1996. (Cited on page 18.)
- [127] F. Dalfovo, S. Giorgini, L. P. Pitaevskii, and S. Stringari. Theory of Bose-Einstein condensation in trapped gases. *Rev. Mod. Phys.*, 71:463, 1999. (Cited on page 20.)
- [128] C. J. Pethick and H. Smith. Bose Einstein Condensation in Dilute Gases. *Cambridge University Press*, 2002. (Cited on page 22.)
- [129] S. Ghanbari, P. B. Blakie, P. Hannaford, and T. D. Kieu. Superfluid to Mott insulator quantum phase transition in a 2D permanent magnetic lattice. *Eur. Phys. J. B*, 70:305310, 2009. (Cited on pages 24 and 30.)

-
- [130] F. S. Cataliotti, S. Burger, C. Fort, P. Maddaloni, F. Minardi, A. Trombettoni, A. Smerzi, and M. Inguscio. Josephson junction arrays with Bose-Einstein condensates. *Science*, 293:843, 2001. (Cited on page 24.)
- [131] D. Jaksch, C. Bruder, J. I. Cirac, C. W. Gardiner, and P. Zoller. Cold bosonic atoms in optical lattices. *Phys. Rev. Lett.*, 81:3108, 1998. (Cited on page 24.)
- [132] G. G. Batrouni, V. Rousseau, R. T. Scalettar, M. Rigol, A. Muramatsu, P. J. H. Denteneer, and M. Troyer. Mott domains of bosons confined on optical lattices. *Phys. Rev. Lett.*, 89:117203, 2002. (Cited on page 25.)
- [133] S. Trotzky, P. Cheinet, S. Fölling, M. Feld, U. Schnorrberger, A. M. Rey, A. Polkovnikov, E. A. Demler, M. D. Lukin, and I. Bloch. Time-resolved observation and control of superexchange interactions with ultracold atoms in optical lattices. *Science*, 319:295, 2008. (Cited on page 26.)
- [134] P. Treutlein. Coherent manipulation of ultracold atoms on atom chips. *PhD thesis*, Ludwig-Maximilians Universität München, 2008. (Cited on pages 26 and 27.)
- [135] C. Henkel. Magnetostatic field noise near metallic surfaces. *Eur. Phys. J. D*, 35:59, 2005. (Cited on pages 26 and 28.)
- [136] C. Henkel, P. Krüger, R. Folman, and J. Schmiedmayer. Fundamental limits for coherent manipulation on atom chips. *Appl. Phys. B*, 76:173, 2003. (Cited on page 27.)
- [137] C. Henkel, S. Pötting, and M. Wilkens. Loss and heating of particles in small and noisy traps. *Appl. Phys. B*, 69:379, 1999. (Cited on page 27.)
- [138] C. Henkel and S. Pötting. Coherent transport of matter waves. *Appl. Phys. B*, 72:73, 2001. (Cited on page 27.)
- [139] T. A. Pasquini, Y. Shin, C. Sanner, M. Saba, A. Schirotzek, D. E. Pritchard, and W. Ketterle. Quantum reflection from a solid surface at normal incidence. *Phys. Rev. Lett.*, 93:223201, 2004. (Cited on page 28.)

- [140] Z. Yan, A. Dalgarno, and J. F. Babb. Long-range interactions of lithium atoms. *Phys. Rev. A.*, 55:2882, 1997. (Cited on page 28.)
- [141] Y. Wang, P. Surendran, S. Jose, T. Tran, I. Herrera, S. Whitlock, R. McLean, A. Sidorov, and P. Hannaford. Magnetic lattices for ultracold atoms and degenerate quantum gases. *Science Bulletin*, 61:1097–1106, 2016. (Cited on page 30.)
- [142] J. Yu, Z. Xu, R. Lü, and L. You. Dynamical generation of topological magnetic lattices for ultracold atoms. *Phys. Rev. Lett.*, 116:143003, 2016. (Cited on page 30.)
- [143] S. Whitlock, B. V. Hall, T. Roach, R. Anderson, M. Volk, P. Hannaford, and A. I. Sidorov. Effect of magnetization inhomogeneity on magnetic microtraps for atoms. *Phys. Rev. A*, 75:043602, 2007. (Cited on page 30.)
- [144] S. Whitlock. Bose-Einstein condensates on a magnetic film atom chip. *Swinburne PhD thesis*, 2007. (Cited on page 34.)
- [145] P. F. Carcia, A. D. Meinhaldt, and A. Suna. Perpendicular magnetic anisotropy in Pd/Co thin film layered structures. *Appl. Phys. Lett.*, 47:178, 1985. (Cited on page 34.)
- [146] W. B. Zeper, F. J. A. M. Greidanus, and P. F. Carcia. Evaporated Co/Pt layered structures for magneto-optical recording. *IEEE Transactions on Magnetics*, 25:3764, 1989. (Cited on page 34.)
- [147] D. G. Stinson and S.-C. Shin. Magnetization and anisotropy of Co/Pd multilayer thin films. *J. Appl. Phys.*, 67:4459, 1990. (Cited on page 34.)
- [148] A. G. Roy, D. E. Laughlin, T. J. Klemmer, K. Howard, S. Khizroev, and D. Litvinov. Seed-layer effect on the microstructure and magnetic properties of Co/Pd multilayers. *J. Appl. Phys.*, 89:7531, 2001. (Cited on page 34.)

- [149] I. G. Hughes, P. A. Barton, T. M. Roach, and E. A. Hinds. Atom optics with magnetic surfaces: Ii. microscopic analysis of the 'floppy disk' mirror. *J. Phys. B: At. Mol. Opt. Phys.*, 30:2119, 1997. (Cited on page 42.)
- [150] Ron Folman, Philipp Treutlein and Jörg Schmiedmayer. Atom chip fabrication. *Atom Chips, edited by Jakob Reichel and Vladan Vuletić, Wiley*, pages 61–110, 2011. (Cited on page 46.)
- [151] Ruquan Wang. Approaching Lithium BEC with a mini trap. *Yale University PhD Thesis*, 2006. (Cited on page 47.)
- [152] M. B. Squires, J. A. Stickney, E. J. Carlson, P. M. Baker, W. R. Buchwald, S. Wentzell, and S. M. Miller. Atom chips on direct bonded copper substrates. *Rev. Sci. Instrum.*, 82:023101, 2011. (Cited on page 47.)
- [153] M. Singh. A magnetic lattice and macroscopic entanglement of a BEC on an atom chip. *Swinburne PhD thesis*, 2008. (Cited on pages 51 and 62.)
- [154] S. Jose. Trapping of ultracold atoms in a magnetic lattice. *Swinburne PhD thesis*, 2013. (Cited on page 51.)
- [155] P. Surendran. Bose-Einstein condensation in a magnetic lattice. *Swinburne PhD thesis*, 2015. (Cited on pages 51, 61, 75, and 92.)
- [156] C. Wieman and T. W. Hänsch. Doppler-free laser polarization spectroscopy. *Phys. Rev. Lett.*, 36:1170, 1976. (Cited on page 55.)
- [157] C. P. Pearman, C. S. Adams, S. G. Cox, P. F. Griffin, D. A. Smith, and I. G. Hughes. Polarization spectroscopy of a closed atomic transition: applications to laser frequency locking. *J. Phys. B: At. Mol. Phys.*, 35:5141, 2002. (Cited on page 55.)
- [158] J. Dalibard and C. Cohen-Tannoudji. Laser cooling below the Doppler limit by polarization gradients: simple theoretical models. *J. Opt. Soc. Am. B*, 6:2023, 1989. (Cited on page 55.)

- [159] W. Demtröder. Laser spectroscopy. *Springer-Verlag*, 1993. (Cited on page 56.)
- [160] D. A. Smith, S. Aigner, S. Hofferberth, M. Gring, M. Andersson, S. Wildermuth, P. Krüger, S. Schneider, T. Schumm, and J. Schmiedmayer. Absorption imaging of ultracold atoms on atom chips. *Opt. Express*, 19(9):8471–8485, 2011. (Cited on pages 61 and 80.)
- [161] <http://atomcool.rice.edu/>. (Cited on page 63.)
- [162] D. S. Jin, J. R. Ensher, M. R. Matthews, C. E. Wieman, and E. A. Cornell. Collective excitations of a Bose-Einstein condensate in a dilute gas. *Phys. Rev. Lett.*, 77:420, 1996. (Cited on page 69.)
- [163] S. Stringari. Collective excitations of a trapped Bose-Condensed gas. *Phys. Rev. Lett.*, 77:2360, 1996. (Cited on page 71.)
- [164] Y. Castin and R. Dum. Bose-Einstein condensates in time dependent traps. *Phys. Rev. Lett.*, 77:5315, 1996. (Cited on page 74.)
- [165] Russell Anderson. Nonequilibrium dynamics and relative phase evolution of two-component Bose-Einstein condensates. *Swinburne PhD thesis*, 2010. (Cited on page 76.)
- [166] D. M. Harber, J. M. McGuirk, J. M. Obrecht, and E. A. Cornell. Thermally induced losses in ultra-cold atoms magnetically trapped near room-temperature surfaces. *J. Low Temp. Phys.*, 133:229, 2003. (Cited on pages 83, 84, and 88.)
- [167] E. L. Surkov, J. T. M. Walraven, and G. V. Shlyapnikov. Collisionless motion and evaporative cooling of atoms in magnetic traps. *Phys. Rev. A*, 53:3403, 1996. (Cited on page 88.)
- [168] C. Stehle, H. Bender, C. Zimmermann, D. Kern, M. Fleischer and S. Slama. Plasmonically tailored micropotentials for ultracold atoms. *Nature Photon.*, 5:494, 2011. (Cited on page 105.)

- [169] T. Jacqmin, B. Fang, T. Berrada, T. Roscilde, and I. Bouchoule. Momentum distribution of one-dimensional Bose gases at the quasicondensation crossover: Theoretical and experimental investigation. *Phys. Rev. A.*, 86:043626, 2012. (Cited on page 113.)
- [170] S. Whitlock, A. W. Glaetzle, and P. Hannaford. Simulating quantum spin models using rydberg-excited atomic ensembles in magnetic microtrap arrays. *J. Phys. B: At. Mol. Opt. Phys.*, 50:074001, 2017. (Cited on page 114.)
- [171] M. Saffman, T. G. Walker, and K. Mølmer. Quantum information with Rydberg atoms. *Rev. Mod. Phys.*, 82:2313 , 2010. (Cited on page 114.)

Publications

1. *Trapping ultracold atoms at 100 nm from a surface in a 0.7 μm -period magnetic lattice*

Y. Wang, T. Tran, P. Surendran, I. Herrera, A. Balcytis, D. Nissen, M. Albrecht, A. Sidorov and P. Hannaford
arXiv:1705.09419 (2017)

2. *Magnetic lattices for ultracold atoms and degenerate quantum gases*

Y. Wang, P. Surendran, S. Jose, T. Tran, I. Herrera, S. Whitlock, R. McLean, A. Sidorov, and P. Hannaford
Science Bulletin **61**, 1097-1106 (2016)

3. *Sub-micron period lattice structures of magnetic microtraps for ultracold atoms on an atom chip*

I. Herrera, Y. Wang, P. Michaux, P. Surendran, S. Juodkazis, S. Whitlock, R. McLean, A. Sidorov, M. Albrecht, and P. Hannaford
J. Phys. D: Appl. Phys. **48**, 115002 (2015)

4. *Radio-frequency spectroscopy of a linear array of Bose-Einstein condensates in a magnetic lattice*

P. Surendran, S. Jose, Y. Wang, I. Herrera, S. Whitlock, R. McLean, A. Sidorov and P. Hannaford
Phys. Rev. A **91**, 023605 (2015)

5. *Periodic array of Bose-Einstein condensates in a magnetic Lattice*

S. Jose, P. Surendran, Y. Wang, I. Herrera, M. Singh, L. Krzemien, S. Whitlock,
A. Sidorov, R. McLean, and P. Hannaford
Physical Review A **89**, 051602(R), (2014)